DEFENCE S&T TECHNICAL BULLETIN
BULETIN TEKNIKAL S&T PERTAHANAN

VOL. 4 JIL. | NUM. 2 BIL. | YEAR 2011 TAHUN | ISSN 1985-6571

CONTENTS

STRIDE™

SCIENCE & TECHNOLOGY RESEARCH INSTITUTE FOR DEFENCE
INSTITUT PENYELIDIKAN SAINS & TEKNOLOGI PERTAHANAN

AIMS AND SCOPE

The Defence S&T Technical Bulletin is the official technical bulletin of the Science & Technology Research Institute for Defence (STRIDE). It contains articles on research findings in various fields of defence science & technology. The primary purpose of this bulletin is to act as a channel for the publication of defence-based research work undertaken by researchers both within and outside the country.

WRITING FOR THE DEFENCE S&T TECHNICAL BULLETIN

Contributions to the journal should be based on original research in areas related to defence science & technology. All contributions should be in English.

PUBLICATION

The editors' decision with regard to publication of any item is final. A paper is accepted on the understanding that it is an original piece of work which has not been accepted for publication elsewhere. Contributors will receive two complimentary copies of the issue in which their work appears.

PRESENTATION OF MANUSCRIPTS

The format of the manuscript is as follows:

a) Page size B5 (JIS)
b) MS Word format
c) Single space
d) Justified
e) In Times New Roman ,11-point font
f) Should not exceed 20 pages, including references
g) Texts in charts and tables should be in 10-point font.

Please e-mail the manuscript to:

1) Dr. Zalini bt Yunus (zalini.yunus@stride.gov.my)
2) Dr. Mahdi bin Che Isa (mahdi.cheisa@stride.gov.my)
3) Dinesh Sathyamoorthy (dinesh.sathyamoorthy@stride.gov.my)

The next edition of the bulletin is expected to be published in April 2012. The due date for submissions is 29 February 2012. **It is strongly iterated that authors are solely responsible for taking the necessary steps to ensure that the submitted manuscripts do not contain confidential or sensitive material.**

The template of the manuscript is as follows:

TITLE OF MANUSCRIPT

Name(s) of author(s)

Affiliation(s)

E-mail:

ABSTRACT

Contents of abstract.

Keywords: *Keyword 1; keyword 2; keyword 3; keyword 4; keyword 5.*

1. TOPIC 1

Paragraph 1.

Paragraph 2.

1.1 Sub Topic 1

Paragraph 1.

Paragraph 2.

2. TOPIC 2

Paragraph 1.

Paragraph 2.

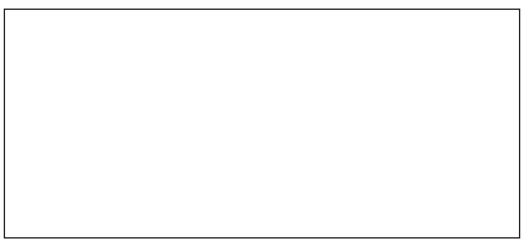

Figure 1: Title of figure.

Table 1: Title of table.

Content	**Content**	**Content**
Content	Content	Content
Content	Content	Content
Content	Content	Content

Equation 1 (1)
Equation 2 (2)

REFERENCES

Long lists of notes of bibliographical references are generally not required. The method of citing references in the text is 'name date' style, e.g. 'Hanis (1993) claimed that...', or '…including the lack of interoperability (Bohara *et al.*, 2003)'. End references should be in alphabetical order. The following reference style is to be adhered to:

Books

Serra, J. (1982). *Image Analysis and Mathematical Morphology*. Academic Press, London.

Book Chapters

Goodchild, M.F. & Quattrochi, D.A. (1997). Scale, multiscaling, remote sensing and GIS. *In* Quattrochi, D.A. and Goodchild, M.F. (Eds.), *Scale in Remote Sensing and GIS*. Lewis Publishers, Boca Raton, Florida, pp. 1-11.

Journals / Serials

Jang, B.K. & Chin, R.T. (1990). Analysis of thinning algorithms using mathematical morphology. *IEEE T. Pattern Anal.*, **12**: 541-550.

Online Sources

GTOPO30 (1996). *GTOPO30: Global 30 Arc Second Elevation Data Set*. Available online at: http://edcwww.cr.usgs.gov/landdaac/gtopo30/gtopo30.html (Last access date: 1 June 2009)

Unpublished Materials (e.g. theses, reports and documents)

Wood, J. (1996). *The Geomorphological Characterization of Digital Elevation Models*. PhD Thesis, Department of Geography, University of Leicester, Leicester.

THERMOGRAPHIC MASS BLIND FEVER SCREENING: A REVIEW OF THE EFFECTIVENESS OF CORRELATION TESTS AND OPERATIONS

Dinesh Sathyamoorthy[1*] & Ahmad Razi Mohamed Yunus[2]

[1]Instrumentation & Electronics Technology Division (BTIE)
[2]Protection & Biophysical Technology Division (BTPB)
Science & Technology Research Institute for Defence (STRIDE), Ministry of Defence, Malaysia

[*]E-mail: dinesh.sathyamoorthy@stride.gov.my

ABSTRACT

Recent efforts to control the spread of epidemic infectious diseases, such as the 2003 severe acute respiratory syndrome (SARS) outbreak, the 2006 avian influenza outbreak and 2009 influenza A(H1N1) pandemic, have prompted health officials to develop rapid screening processes to detect febrile patients. The ideal device for fever screening should be speedy, non-invasive and be able to accurately detect febrile patients with minimal inconvenience and disruption of human traffic. To this end, thermography has been proposed as a non-contact and non-invasive method for detecting fever. This paper is aimed at conducting a critical review of the effectiveness of thermographic mass blind fever screening in terms of correlation tests and operations. The overall effectiveness of thermographic fever screening is subject to various environmental and subject factors, and performance characteristics of the thermographic device employed. Furthermore, reported thermographic fever screening operations have produced high false discovery rates, resulting in high proportions of patients being mistakenly classified as febrile and subsequently being referred for medical examination. Nevertheless, thermography has significant potential to be a quick non-contact and non-invasive method for mass blind fever screening which helps reduce the workload of medical officers. It is important that thermographic fever screening operations be carefully planned and conducted in order to yield the best possible results.

Keywords: *Thermographic mass blind fever screening; core body and skin temperatures; correlation; receiver operating characteristics (ROC); false discovery rate.*

1. INTRODUCTION

Recent efforts to control the spread of epidemic infectious diseases, such as the 2003 severe acute respiratory syndrome (SARS) outbreak, the 2006 avian influenza outbreak and 2009 influenza A(H1N1) pandemic, have prompted health officials to develop rapid screening processes to detect febrile patients. Such screening may take place at hospital entries, mainly in emergency departments, or at airports and immigration check points to detect travellers with increased core body temperatures. These fever screening stations employ personnel to take oral, aural or axillary temperatures to pick out those with fever and send them for further clinical evaluations, and hence, curb the spread of the disease (Kaydos-Daniels *et al.*, 2004; St. John *et al.*, 2005; Goh *et al.*, 2006; Chiappini *et al.*, 2009; Jefferson *et al.*, 2009; Mukherjee *et al.*, 2010). Oral, aural and axillary temperature measurements are accurate, but are rather invasive, time-consuming and labour-intensive. The ideal device for fever screening should be speedy, non-invasive and be able to accurately detect febrile patients with minimal inconvenience and disruption of human traffic. To this end, thermography has been proposed as a non-contact and non-invasive method for detecting fever (Seffrin, 2003; Jiang *et al.*, 2006; Wong & Wong, 2006; Ng & Acharya, 2009; Bitar *et al.*, 2009; Ng, 2010).

There has been increasing interest in the medical applications of thermography for diagnosis, in particular in areas of rheumatology, dermatology, orthopaedics and circulatory abnormalities (Jiang *et al.*, 2006; Ivatinitsky *et al.*, 2006; Diakides & Bronzion, 2007; Hildebrandt *et al.*, 2010). However, the extension of thermographic diagnostic tools to mass blind fever screening has not yet been thoroughly assessed. Many of the present thermographic systems in use at airports and immigration checkpoints have not been scientifically validated. As a result, they may create a false sense of security by underestimating the number of febrile (and possibly infected) individuals (Seffrin , 2003; Wong & Wong, 2006; Hausfater *et al.*, 2008; Ng & Acharya, 2009; Mercer & Ring, 2009; Bitar *et al.*, 2009; Nguyen *et al.*, 2010). Nevertheless, fever screening operators largely rely on use of thermography due to the need to screen massive numbers of travellers at borders and airports. In addition, thermographic mass screening of suspected febrile visitors at the entrances of hospitals has become standard procedure (Chiang *et al.*, 2008; Ng & Acharya, 2009; Bitar *et al.*, 2009; Ng, 2010)

This paper is aimed at conducting a critical review of the effectiveness of thermographic mass blind fever screening in terms of correlation tests and operations. The review is conducted based on the abundance of literature on the related topics, in particular since the 2003 SARS outbreak, and the first author's experience as a member of the Science & Technology Research Institute for Defence (STRIDE) team which conducted thermographic fever screening for suspected influenza A(H1N1) patients in the Kuala Lumpur International Airport (KLIA) from 30 April to 13 May 2009 (Abdul Ghaffar *et al.*, 2009a,b; STRIDE, 2009).

2. CORRELATION TESTS

Thermography is only a physiological test rather than an anatomical test such as computed tomography, X-ray and mammography. The thermographic device (either an infrared thermometer or a thermal camera) and operator can be positioned at a distance from the subject to be screened (Figure 1). The thermographic device detects infrared radiation emitted from human skin surfaces and converts it into electrical signals, which are then used to display a temperature reading of an area of interest (via infrared thermometer) and / or temperature profile / colour graphically (via thermal camera). The thermogram shows thermal patterns on the subject's skin surface, including hot and cold spots. Hence, it is possible to use thermography for the detection of febrile patients in a crowd due to its capability of detecting individuals with elevated temperature. The subject is deemed to have an elevated temperature if the facial temperature is above the threshold setting, which is determined based on the correlation between core body temperature measured via oral / aural / axillary thermometer and skin temperature measured via the employed thermographic device (Seffrin, 2003; Jiang *et al.*, 2006; Wong & Wong, 2006; Ng & Acharya, 2009; Bitar *et al.*, 2009; Ng, 2010).

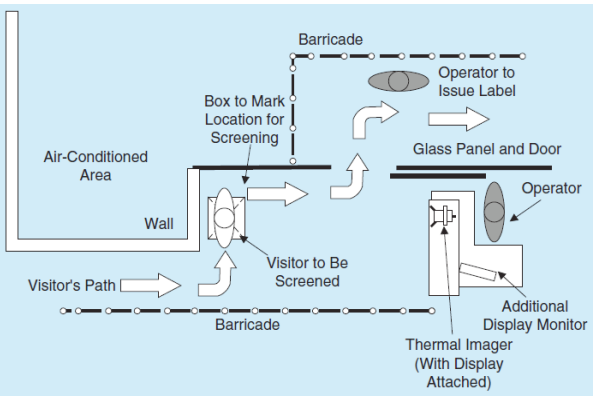

Figure 1: Example of a thermographic mass blind fever screening operation setup. (Ng & Acharya, 2009)

Ng *et al.* (2004, 2006), Hausfater *et al.* (2008), Ring *et al.* (2008) and Ng (2010) reported that the best skin temperature reading is from the maximum temperature in the eye region, followed by the maximum temperature in the forehead region. However, the eye region may not be appropriate for mass screening because of difficulty in measuring temperature accurately through eyeglasses, which are worn by many people (Hausfater *et al.*, 2008; Bitar *et al.*, 2009). Left ear temperature is often used to represent core body temperature as it resembles brain temperature (Ng *et al.*, 2006).

The outcome of thermographic mass blind fever screening can be positive *P* (febrile) (Figure 2) or negative *N* (healthy) (Figure 3), while the actual health status of the subject may be different. In this setting, the following possibilities occur:

i) **True positive *TP*:** Febrile subjects correctly identified as febrile
ii) **False positive *FP*:** Healthy subjects wrongly identified as febrile
iii) **True negative *TN*:** Healthy subjects correctly identified as healthy
iv) **False negative *FN*:** Febrile subjects wrongly identified as healthy

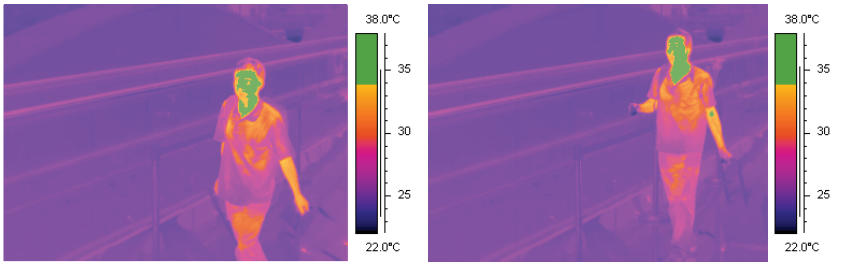

(a) **(b)**

Figure 2: Thermograms of positive subjects (STRIDE, 2009).

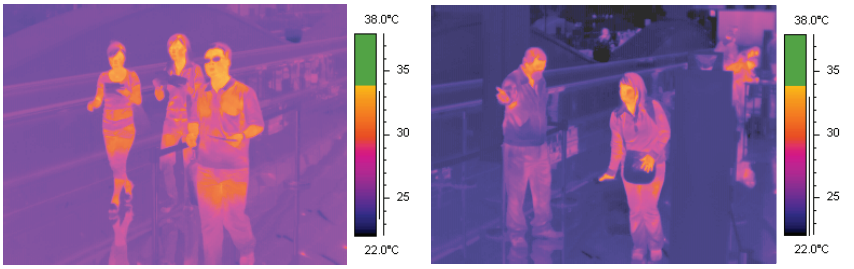

(a) **(b)**

Figure 3: Thermograms of negative subjects (STRIDE, 2009)

Analysis of the collected data is usually conducted using regression analysis and receiver operating characteristics (ROC), which is a measure of sensitivity and specify. Regression analysis is used to determine the correlation between core body and skin temperatures, via the coefficient of determination R^2 of the linear regression (Weisberg, 2005; Devore, 2010). Sensitivity S_N (Equation 1) measures the proportion of actual positive subjects that are correctly identified, while specificity S_P (Equation 2) measures the proportion of negative subjects that are correctly identified. For any test, there is usually a trade-off between both measures. The optimal threshold is defined as the value that yields the highest combined sensitivity and specificity (Fawcett, 2004, 2006). For fever screening operations, it is generally preferable to have a relatively high rate of false positives (low sensitivity) in order to increase the chances of avoiding false negatives (high specificity) (STRIDE, 2009).

$$S_N = \frac{TP}{TP + FN} \tag{1}$$

$$S_P = \frac{TN}{TN + FP} \tag{2}$$

The trade-off between sensitivity and specificity can be graphically represented using a ROC curve, which is a plot of sensitivity vs (100 - specificity) as the discrimination threshold is varied. It is a graphical means of assessing the ability of a test to discriminate between healthy and febrile subjects. It is often used by clinical researchers in assessing how accurate a particular test is in identifying fever cases. The best possible prediction would yield a point in the upper left corner of the ROC space (coordinate (0,100)), representing 100% sensitivity (no false positives) and 100% specificity (no false negatives). The diagonal line from the bottom left to the top right corners of the ROC space (the line of no-discrimination) divides the ROC space into areas of good or bad classification. Points above the diagonal line indicate good classification results, while points below the line indicate wrong results. The area under the ROC curve *AUC* provides a measure of the average performance of the test (Fawcett, 2004, 2006).

A large number of subjects is required to obtain a proper correlation between core body and skin temperatures. Basis *et al.* (2005), who used 203 subjects, noted that their sample size was too small for their findings to be conclusive. Due to time limitation, STRIDE (2009) only used 27 subjects, consisting of STRIDE officers and staff. This small number of subjects resulted in low values of R^2 (0.005) and *AUC* (0.61) (Figure 4). Furthermore, as all the subjects were healthy (no febrile subjects could be found in short notice), it was hard to determine the behaviour of the correlation at core body temperatures higher than 38 °C, which is the core body temperature threshold for fever (WHO, 2009; CPRC, 2009). In comparison, various studies have used significantly larger number of subjects, consisting of both healthy and febrile subjects, and obtained higher values of R^2 and *AUC* (Table 1).

It is important to understand that skin temperature does not solely depend on core body temperature and may be affected by other subject factors, including age, gender and use of antipyretic drugs, and environmental factors, including subject-sensor distance, ambient temperature and humidity, and surrounding ventilation system (Seffrin, 2003; Wong & Wong, 2006; Ng & Acharya, 2009; Bitar *et al.*, 2009; Nguyen *et al.*, 2010; Weinert, 2010). The emissivity of clean, dry human skin is close to the emissivity of a blackbody (0.98), but can vary between 0.94 and 0.99 depending on face contour, makeup, sweat and skin complexion (Ng *et al.*, 2004, 2006; Ng, 2005; Ng & Archaya, 2009). Measurement error resulting from variation in oral / aural / axillary thermometer measurement and technique could also decrease the correlation between core body and skin temperatures (Jensen *et al.*, 2000; Daanen, 2006; Ring *et al.*, 2008, 2010; Nguyen, 2010). Furthermore, factors such as insufficient straightened ear canal or earwax obstructing the path of heat radiating from the tympanic membrane could cause reduction in aural temperature measurement (Hay *et al.*, 2004; Chiappini *et al.*, 2009, 2011).

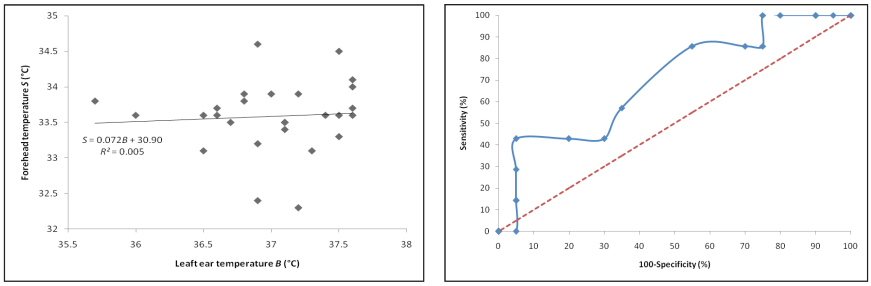

(a) **(b)**

Figure 4: Results of the test on correlation between core body and skin temperatures conducted in STRIDE (2009), using core body temperature threshold of 37.5 °C: (a) Linear regression between forehead temperatures *S* and left ear temperatures *B*, with very low value of R^2 (0.005). (b) ROC curve, with low value of *AUC* (0.61). From the curve, the best trade-off is observed at sensitivity of 42.6% and specificity of 95%, corresponding to forehead temperature of 34 °C. The other thresholds give either false positive or false negative rates that are too high.

In addition, during such correlation tests, core body and skin temperatures are measured from subjects who are usually standing still. However, in actual fever screening operations, skin temperatures would be measured from subjects who would have walked certain distances prior to arriving at the fever screening area, while carrying luggage, children etc., resulting in increased core body and skin temperatures (Bitar *et al.*, 2009; STRIDE, 2009).

Studies that have been conducted on the effectiveness of thermographic fever screening correlation tests have given mixed conclusions. Chan *et al.* (2004), Ng *et al.* (2004, 2006), Ng (2005), Chiang *et al.* (2008), Nguyen *et al.* (2010), Chiappini *et al.* (2011), Teran *et al.* (2011) and Hewlett *et al.* (2011) reported that thermography can be used as a first line tool for mass blind fever screening, and that skin temperatures measured via thermography have good correlation with core body temperature measurements. However, Ng *et al.* (2005), Cheung *et al.* (2008), Hausfater *et al.* (2008), Paes *et al.* (2010) and Priest *et al.* (2011) reported that skin temperature measurements via thermography do not provide a reliable basis for screening patients who are febrile because the gradient between skin and core body temperatures is markedly influenced by various subject and environmental characteristics.

Nevertheless, thermography was the primary means of mass blind fever screening during the 2009 influenza A(H1N1) pandemic (Ng, 2010; Mukherjee *et al.*, 2010; Nishiura & Kamiya, 2011) as it is economic, quick and does not inflict any discomfort on the subjects. Furthermore, as it is passive in nature, it does not emit any harmful radiation or subject the person to any risk. In addition, as it is a non-contact screening procedure, it is hygienic and does not require sterilisation or disposables (Seffrin, 2003; Ng & Acharya, 2009; Bitar *et al.*, 2009; Chiapini *et al.*, 2009, 2011).

Table 1: Reported results of studies on correlation between core body and skin temperatures*.

Study	Thermographic Device	Number of Subjects			Performance Parameters			
		Healthy	Febrile	Total	Coefficient of Determination R^2	Area under the ROC curve *AUC*	Sensitivity S_N (%)	Specificity S_P(%)
Chan *et al*. (2004)	FLIR ThermaCAM PM595	127	49	176	0.70	na	83.0	88.0
Ng *et al.* (2004)	FLIR ThermaCAM S60	417	87	502	0.55	0.97	85.4	95.0
Ng *et al.* (2005)	Standard ST 8812	498	69	567	0.26	na	89.4	75.4
Ng (2005)	FLIR ThermaCAM S60	416	86	502	0.52	0.91	90.7	75.8
Basis *et al.* (2005)	na	184	19	203	na	na	42.0	98.0
Ng *et al.* (2006)	FLIR ThermalVision900	na	na	750	0.78	na	na	na
Chiang *et al.* (2008)	Telesis Spectrum 9000MB	968	64	1,032	0.44	0.81	100.0	52.4
Cheung *et al.* (2008)	na	1,302	215	1,517	0.434	na	68.0	22.4
Hausfater *et al.* (2008)	Raytex Raynger MX	1,964	62	2,026	0.27	0.87	82.0	77.0
Abdul Ghaffar *et al.* (2009a), STRIDE (2009)	FLIR ThermaCAM SC3000	27	0	27	0.005	0.61	42.6	95.0
Paes *et al.* (2010)	Thermofocus 700A2	na	na	100	0.66	na	0.64	0.96
Nguyen *et al.* (2010)	Optotherm Thermoscreen	2,809	64	2,873	0.43	0.96	91.0	90.0
Chiappini *et al.* (2011)	Thermofocus 0800	198	53	251	0.84	na	88.7	89.9
Teran *et al.* (2011)	Thermofocus 01500	267	167	434	0.95	na	97.0	97.0
Hewlett *et al.* (2011)	Optotherm Thermoscreen	523	43	566	na	na	60.0	97.0
Priest *et al.* (2011)	ThermaCAM E45	1,245	30	1,275	na	0.66	87.0	39.0

*For some of these studies, correlation tests were conducted for multiple scenarios (e.g. types of thermographic devices, temperature and relative humidity, body parts, core body temperature thresholds, physical activities, gender and age). The parameters for scenarios recommended by the respective authors are presented here.
na: Information not available.

3. OPERATIONS

The results of reported thermographic fever operations (Table 2) have produced high false discovery rates *FDR* (Equation 3). This resulted in large proportions of patients being mistakenly classified as febrile and subsequently being referred for medical examination.

$$FDR = \frac{FP}{P} \tag{3}$$

The false discovery rate for such operations could be reduced by increasing the forehead temperature threshold, but without any knowledge on the status of the negative subjects, in particular the false negative subjects, this is too risky to be done. While it is preferable to have a lower false discovery rate, it is absolutely vital that the possibilities of having false negatives be reduced as much as possible (STRIDE, 2009).

It is important to note that, despite the high false discovery rates, only a small fraction of the patients were identified as positive subjects, reducing the medical officers' workload. The alternative, conducting oral / aural / axillary temperature measurement on all possible subjects, would have been extremely hectic, time-consuming and undesirable. In this aspect, thermographic mass blind fever screening proved to be a quick non-contact and non-invasive method that did not inflict any discomfort on the subjects (Bitar *et al.*, 2009; STRIDE, 2009).

Many variables can affect the accuracy of thermographic mass blind fever screening. Ideally, the thermographic device should have temperature discrimination of not more than 0.1 °C, and be operated in a stable controlled indoor environment within 1 °C. The accuracy of the thermographic device is highly dependent on the skill and knowledge of the operator. Mishandling of the equipment can result in erroneous data. A number of factors are known to affect the temperature readings of thermographic devices, in particular variation in operating environment and screened subjects. Thermographic devices have different degrees of temperature drifts between self-correction, uniformity within field of view, error and stability of temperature threshold, distance effect and detector sizes. Hence, operators should receive adequate training for proper operation, maintenance and application of the corresponding thermographic device for its intended fever screening operation (Seffrin, 2003; Wong & Wong, 2006; ICE, 2008; ISO, 2009; Mercer & Ring, 2009; Ng & Acharya, 2009; Nguyen *et al.*, 2010; Ring *et al.*, 2010; Chiappini *et al.*, 2011). Details on thermographic device requirements for fever screening are discussed in ICE (2008), ISO (2009) and Ng & Archaya (2009).

Table 2: Reported results of thermographic mass blind fever screening operations*.

Operation	Location	Thermographic Device	Duration	Number of Subjects			False Discovery Rate *FDR* (%)
				Total	Positive	True Positive	
Health Canada (2004)	Vancouver International Airport	na	May - November 2003	3,920,407	1,365	0	100
	Pearson Airport			649,352	70	0	100
	Pearson Airport		1 September - 10 December 2003	na	733	49	93.32
Chiu *et al.* (2005)	Taipei Medical University - Wan Fang Hospital	Telesis Spectrum 9000 MB	13 April - 12 May 2003	72,327	305	3	99.01
Shu *et al.* (2005)	C.K.S. and Kaohsiung Airports	na	July 2003 - June 2004	8,000,000	22,000	3,011	86.31
McBride & Buikstra (2007), McBride *et al.* (2010)	Cairns International Airport	FLIR ThermoCAM E45	April - September 2006	181,759	963	118	87.75
Abdul Ghaffar *et al.* (2009b), STRIDE (2009)	KLIA Satellite Building, Gate C22	FLIR ThermaCAM SC3000	30 April - 13 May 2009	34, 845	3,896	350	91.01
Nishiura & Kamiya (2011)	Narita International Airport	NEC / AVIO TVS-500	28 April - 18 June 2009	441,041	805	18	97.76
			1 September 2009- 31 January 2010	9,140,435	930	293	68.49

*While most of these operations employ initial oral / aural / axillary temperature measurement to determine the number of true positive subjects, other methods are also used. For example, for the first part of the operation in Health Canada (2004) (May to November 2003), the number of true positive subjects was determined based on real-time reverse transcription polymerase chain reaction (RT-PCR) confirmatory diagnostic, while for the second part (1 September to 10 December 2003), initial aural temperature measurement was used.

na: Information not available.

False positive / negative readings could be caused by the subjects themselves. False negative readings may be seen in subjects with heavy makeup, who are on medication or have circulatory problems, or even from deliberate cooling of the face. A subject who is perspiring heavily will be presented as significantly cooler due to evaporative cooling effect. False positive results may be seen in subjects who are pregnant, menstruating, on hormone replacement therapy, have recently consumed alcohol or hot drinks, or have undergone physical exertion before the screening. Factors such as stress, use of stimulants, such as caffeine and nicotine, and inflammation caused by trauma or sunburn could also cause false positive results (Seffrin, 2003; Wong & Wong, 2006; Mercer & Ring, 2009; Ng & Acharya, 2009; Bitar *et al.*, 2009; Ng, 2010).

An important factor that should be taken into account is body temperature regulation at the early stage of a typical fever, where the body attempts to raise its temperature but vasoconstriction occurs to prevent heat loss through the skin. For this reason, some individuals at this stage of fever will not be detected via thermography (Guyton, 2000; Ng, 2005; Ng *et al.*, 2006; Mercer & Ring, 2009; Mukherjee *et al.*, 2010). In addition, patients who have underlying diseases, such as cancer, diabetes and hypertension, or who are in postoperative state may not be symptomatic at the early stage of infectious diseases (Ng, 2005).

During the fever screening operation in KLIA, two false negative cases occurred (The Star, 2009a,b; NST, 2009; MOH, 2009; STRIDE, 2009). Both patients were from flight MH 091 (from Newark, New Jersey, USA), which arrived at KLIA on 13 May 2009, 0715 hrs. It was reported that both patients had only contracted fever after they had left KLIA (The Star, 2009a,b; NST, 2009), and hence, were able to avoid detection from the thermographic fever screening. Even if aural / oral / axillary temperature measurement had been conducted on both patients at the time, they would still not have been detected.

4. CONCLUSION AND RECOMMENDATIONS

On the whole, thermography has significant potential to be a quick non-contact and non-invasive method for mass blind fever screening. However, its overall effectiveness is subject to various environmental and subject factors, and performance characteristics of the thermographic device employed.

In order to maximise the effectiveness of thermographic fever screening, rigorous tests should be conducted using large numbers of subjects (consisting of a good mix of healthy and febrile subjects). The tests should be conducted for various environmental parameters, including varying room temperatures and relative humidity, and for various subject parameters, such as standing still, after physical exertion, after consuming hot / cold drinks etc. It is only through such rigorous

tests that the methodology can be fine-tuned to have high sensitivity and specificity for the specific operating conditions and thermographic device employed. This can allow for decreased false discovery rates, without increasing the risk of having false negatives. In addition, usage of analytical tools, such as automated target recognition, parabolic regression (PR), fuzzy logic and artificial neural networks (ANN), can help improve the diagnostic capabilities of thermographic fever screening.

ACKNOWLEDGEMENT

The authors are grateful to Datuk Dr. Abdul Ghaffar Ramli, Director-General, Science & Technology Research Institute for Defence (STRIDE), Ministry of Defence, Malaysia, Mdm. Wan Salwa Wan Hassan, Director of the STRIDE Instrumentation & Electronics Division (BTIE), Mr. Mohd. Faudzi Mohammad, Head of the STRIDE Radar & Laser Branch, and the reviewers, Dr. Mahdi Che Isa and Mdm. Kathryn Tham Bee Lin, for their suggestions that have helped strengthen this manuscript.

REFERENCES

Abdul Ghaffar, R., Wan Salwa, W.H., Mohamad Muslim, T., Mohammad Shahminan, S., Dinesh, S., Jamilah, J., Hafizah, M.Y. & Maslehah, A.M. (2009a). Assessment of STRIDE's capability to conduct thermographic mass blind fever screening: Preliminary test of correlation between core body and skin temperatures. *National Security Council Meeting*, 29 April 2009, National Security Council, Prime Minister's Department, Putrajaya.

Abdul Ghaffar, R., Wan Salwa, W.H., Mohamad Muslim, T., Mohammad Shahminan, S., Dinesh, S., Jamilah, J., Hafizah, M.Y. & Maslehah, A.M. (2009b). Thermographic mass blind temperature screening for suspected influenza A(N1H1) patients in the Kuala Lumpur International Airport (KLIA) (30 April - 13 May 2009). *National Security Council Meeting*, 18 May 2009, National Security Council, Prime Minister's Department, Putrajaya.

Basis, F., Reznikovich, S. & Vilensky, A. (2005). Thermocameras for screening travellers for fever in the ED: A Pilot Study. *Israeli J. Emerg. Med.*, **5**: 36-39.

Bitar, D., Goubar, A. & Desenclos, J.C. (2009). International travels and fever screening during epidemics: A literature review on the effectiveness and potential use of non-contact infrared thermometers. *Euro Surveill.*, **14**: 1-5.

Chan, L.S., Cheung, G.T.Y., Lauder, I.J. and Kumana, C.R. (2004). Screening for fever by remote-sensing infrared thermographic camera. *J. Travel Med.*, **11**: 273–278.

Cheung B.M.Y., Chan, L.S., Lauder, I.J. & Kumana, C.R. (2008). *Detection of Human Body Temperature with Infrared Thermographic Imaging: Accuracy and Feasibility in Detection of Fever in Human Subjects*. Research Fund for the Control of Infectious Diseases (RFCID), Hong Kong.

Chiang, M.F., Lin, P.W., Lin, L.F., Chiou, H.Y., Chien, C.W., Chu, S.F. & Chiu, W.T. (2008). Mass screening of suspected febrile patients with remote-sensing infrared thermography: Alarm temperature and optimal distance. *J. Formosan Med. Assoc.*,

107: 937-944.

Chiappini, E., Principi, N., Longhi, R., Tovo, P.A., Becherucci, P., Bonsignori, F., Esposito, S., Festini, F., Galli, L., Lucchesi, B., Mugelli, A. & de Martino, M. (2009).Management of fever in children: Summary of the Italian Pediatric Society guidelines. *Clin. Ther.*, **31**: 1826–1843.

Chiappini, E., Sollai, S., Longhi, C., Morandini, L., Laghi, A., Osio, C.E., Persiani, M., Lonati, S., Picchi, R., Bonsignori, F., Mannelli, Galli & Martino, M.D. (2011). Performance of non-contact infrared thermometer for detecting febrile children in hospital and ambulatory settings. *J. Clin. Nurs.*, **20**: 1311-1318.

Chiu, W.T., Lin, P.W., Chiou, H.Y., Lee, W.S., Lee, C.N., Yang, Y.Y., Lee, H.M., Hsieh, M.S., Hu, C.J., Ho, Y.S., Deng, W.P. & Hsu, C.Y. (2005). Infrared thermography to mass-screen suspected SARS patients with fever. *Asia Pac. J. Public Health*, **17**: 26–28.

Crisis Preparedness & Response Centre (CPRC) (2009). *Case Definition of Infleunza A(H1N1) Virus*. Crisis Preparedness & Response Centre (CPRC), Ministry of Health (MOH), Malaysia.

Daanen, H.A.M. (2006). Infrared tympanic temperature and ear canal morphometry. *J. Med. Eng.Tech.*, **30**: 224-234.

Devore, J.L. (2010). *Probability & Statistics for Engineering and the Sciences*. Brooks / Cole, Boston, Massachusetts.

Diakides, N.A. & Bronzion, J.D. (2007). *Medical Infrared Imaging*. CRC Press, Florida.

Fawcett, T. (2004). *ROC Graphs: Notes and Practical Considerations for Researchers*. Technical Report, HP Laboratories, Palo Alto, USA.

Fawcett, T. (2006). An introduction to ROC analysis. *Pattern Recogn. Lett.*, **27**: 861-874.

Goh, K.T., Cutter, J., Heng, B.H., Ma, Stefan, Koh, B.K.W., Kwok, C., Toh, C.M & Chew, S.K. (2006). Epidemiology and control of SARS in Singapore. *Ann. Acad. Med.*, **35**: 301-316.

Guyton, A.C. (2000). *Textbook of Medical Physiology, 10th Ed*. Saunder, Philadelphia, Pennsylvania.

Hausfater, P., Zhao, Y., Defrenne, S., Bonnet, P. & Riou, B. (2008). Cutaneous infrared thermometry for detecting febrile patients. *Emerg. Infect. Dis.*, **54**: 448–450..

Hay, A.D., Peters, T.J., Wilson, A. & Fahey, T. (2004). The use of infrared thermometry for the detection of fever. *Br. J. Gen. Pract.*, **54**: 448–450.

Health Canada (2004). Thermal image scanners to detect fever in airline passengers, Vancouver and Toronto, 2003. *Can. Commun. Dis. Rep.*, **30**: 165-167.

Hewlett, A.L., Kalil, A.C., Strum, R.A., Zeger, W.G. and Smith, P.W. (2011). Evaluation of an infrared thermal detection system for fever recognition during the H1N1 influenza pandemic. *Infect. Cont. Hosp. Ep.*, **32**: 504-506.

Hildebrandt, C., Raschner, C. & Ammer, K. (2010). An overview of recent application of medical infrared thermography in sports medicine in Austria. *Sensor.*, **10**: 4700-4715.

International Electrotechnical Commission (IEC) (2008). *IEC 80601-2-59 (Medical Electrical Equipment- Part 2-59: Particular Requirements for the Basic Safety and Essential Performance of Screening Thermographs for Human Febrile Temperature Screenings)*. International Electrotechnical Commission (IEC), Geneva, Switzerland.

International Organization for Standardization (ISO) (2009). *ISO/TR 13154:2009 (Medical Electrical Equipment: Deployment, Implementation and Operational Guidelines*

for Indentifying Febrile Humans Using a Screening Thermograph). International Organization for Standardization (ISO), Geneva, Switzerland.

Ivatinitsky, G.R., Khizhnyak, E.P., Deev, A.A. & Khizhyak, L.N. (2006). Thermal imaging in medicine: A comparative study of infrared systems operating in wavelength ranges of 3–5 and 8–12 μm as applied to diagnosis. *Dokl. Biochem. Biophy.*, **407**: 59-63

Jefferson, T., Foxlee, R., Del Mar, C., Dooley, L., Ferroni, Hewak, Prabhala, A. Nair, S. & Rivetti, A. (2009). Physical interventions to interrupt or reduce the spread of respiratory viruses: Systematic review. *BMJ*, **339**: b3675.

Jensen, B.N., Jensen, F.S., Madsen, S.N. & Lossl, K. (2000). Accuracy of digital tympanic, oral, axillary and rectal thermometers compared with standard rectal mercury thermometers. *Eur. J. Sug.*, **166**: 848-851.

Jiang, L.J., Ng, E.Y.K., Yeo, A.C.B., Wu, S., Pan, F., Yau, W.Y., Chen, J.H., Yang, Y. (2006). A perspective on medical infrared imaging. *J. Med. Eng. Tech.*, **29**: 257-267.

Kaydos-Daniels, S.C., Olowokure, B., Chang, H.J., Barwick, R.S., Deng, J.F., Kuo S.H., Su, I.J., Chen, K.T., Maloney, S.A. & the SARS International Field Team (2004). Body temperature monitoring and SARS fever hotline. *Emerg. Infect. Dis.*, **10**: 373–376.

McBride, W.J.H. & Buikstra, E. (2007). *Investigation on the Optimal Assessment of Febrile Passengers Detected by Infrared Thermal Scanning at an International Airport. School of Medicine*. James Cook University, Cairns, Australia.

McBride, W.J.H., Buikstra, E. & FitzGerald, M. (2010). Investigation of febrile passengers detected by infrared thermal scanning at an international airport. *Aust. NZ. J. Public Health*, **34**: 5-10.

Mercer, J.B. & Ring, E.F. (2009). Fever screening and infrared thermal imaging: Concerns and guidelines. *Thermology Int.*, **19**:67-69.

Ministry of Health (MOH) (2009). *Press Statement by the Director-General of Health Malaysia on the Current Situation of Influenza A(H1N1) and the Measures Taken by the Ministry of Health Malaysia*. 17 May 2009, Ministry of Health, Malaysia.

Mukherjee, P., Lim, P.L., Chow, A., Barkham, T., Seow, E., Win, M.K., Chua, A., Leo, Y.S. & Chen, M.I.C. (2010). Epidemiology of travel-associated pandemic (H1N1) 2009 infection in 116 patients, Singapore. *Emerg. Infect. Dis.*, **16**: 21-26.

New Straits Times (NST) (2009). *Malaysia Braces for Possible Flu Outbreak*. Available online at:
http://www.nst.com.my/Current_News/NST/Sunday/Frontpage/20090517075014/Article/index_html (Last access date: 27 May 2009).

Ng, D.K., Chan, C.H., Chow, P.Y. & Kwok, K.L. (2005). Non-contact infrared thermometer temperature measurement for screening fever in children. *Ann. Trop. Paediatr.*, **54**: 93-97.

Ng, E.Y.K. (2010). Advanced integrative thermography in identification of human elevated temperature. *In* Annonos, P., Rossi, M., Pham, T.D., Falugi, C., Bussing, A. & Koukou, M. (Eds.) *Advances in Biomedical Research*, WSEAS Press, Stevens Point, Wisconsin, pp. 190-195.

Ng, E.Y.K. & Acharya, R.U. (2009): Remote-sensing infrared thermography: Reviewing the applications of indoor infrared fever-screening systems. *IEEE Eng. Med. Biol. Mag.*, **28**: 76—83.

Ng, E.Y.K., Kaw, G.J.L. & Chang, W.M. (2004). Analysis of IR thermal imager for mass blind fever screening. *Microvasc. Res.,* **68**: 104– 109.

Ng, E.Y.K., Wiryani, M. & Wong, B.S. (2006). Study of facial skin and aural temperature using IR with and w/o TRS. *IEEE Eng. Med. Biol. Mag.*, **25**: 68–74.

Nguyen, A.V., Hohen, N.J., Lipman, H., Brown, C.M, Molinari, N.A., Jackson, W.L., Kirking, H., Szymanowski, P., Wilson, T.W., Salhi, B., Roberts, R.R., Stryker, D.W. & Fishbein, D.B. (2010). Comparison of 3 infrared thermal detection systems and self-report for mass fever screening. *Emerg. Infect. Dis.*, **16**: 1710-1717.

Nishiura, H. & Kamiya, K. (2011). Fever screening during the influenza (H1N1-2009) pandemic at Narita International Airport, Japan. *BMC Infect. Dis.*, **11**:111

Paes, B. F., Vermeulen, K., Brohet, R. M., van der Ploeg, T. & de Winter, J. P. (2010) Accuracy of tympanic and infrared skin thermometers in children. *Arch. Dis. Child.*, **95**: 974-978.

Priest, P.C., Duncan, A.R., Jennings, L.C. & Baker, M.G. (2011). Thermal image scanning for influenza border screening: Results of an airport screening study. *PLoS One*, **6**: e14490.

Ring, E.F.J., Jung, A., Rutowski, Kalicki & Bajwa, U. (2008). Detecting fever in Polish children by infrared thermography. 9th International Conference on Quantitative Infrared Thermography, 25-28 July 2008, Krakow, Poland.

Ring, E.F.J., McEvoy, H., Jung, A., Zuber, J. & Machin, G. (2010). New standards for devices used for the measurement of human body temperature. *J. Med. Eng. Tech.*, **34**: 249-253.

Science & Technology Research Institute for Defence (STRIDE) (2009). *Thermographic Mass Blind Fever Screening for Suspected Influenza A(N1H1) Patients in the Kuala Lumpur International Airport (KLIA) (30 April - 13 May 2009)*. Science & Technology Research Institute for Defence (STRIDE), Ministry of Defence, Malaysia.

Seffrin, R.J. (2003). Thermal imaging for detecting potential SARS infection. *Proc. Nat. Conf. Thermal Imagers for Fever Screening: Selection, Usage and Testing*, Singapore, May 2003, pp. 857–858.

Shu, P.Y., Chien, L.J., Cheng, S.F., Su, C.L., Kuo, Y.C., Liao, T.L., Ho, M.S. & Lin, T.H. (2005). Fever screening at airports and imported dengue. *Emerg. Infect. Dis.*, **11**: 460-462.

St. John, R.K., King, A., Jong, D., Bodie-Collins, M., Squires, S.G. & Tam, T.W.S. (2005). Border screening for SARS. *Emerg. Infect. Dis.*, **11**: 6–10.

Teran, C.G., Torrez-Llanos, J., Teran-Miranda, T.E., Balderrama, C., Shah, N.S. & Villarroel, P. (2011). Clinical accuracy of a non-contact infrared skin thermometer in paediatric practice. *Child Care Health Dev.*, In press.

The Star (2009a). *21-year-old Student from US Has H1N1*. Available online at:
http://thestar.com.my/news/story.asp?file=/2009/5/16/nation/3921680 (Last access date: 27 May 2009).

The Star (2009b). *Another Student Has A (H1N1) Flu*. Available online at:
http://thestar.com.my/news/story.asp?file=/2009/5/17/ah1n1flu/3925765&sec=ah1n1flu (Last access date: 27 May 2009).

Weinert, D. (2010). Circadian temperature variation and ageing. *Ageing Res. Rev.*, **9**: 51-60.

Weisberg, S. (2005). *Applied Linear Regression*. Wiley, New Jersey.

Wong J.J. & Wong, C.Y.C. (2006). Non-contact infrared thermal images for mass fever screening: State of the art or myth? *Hong Kong Med. J.*, **12**: 242–243.

World Health Organization (WHO) (2009). *Interim WHO Guidance for the Surveillance of Human Infection with Swine Influenza A (H1N1) Virus*. World Health Organization (WHO), Geneva, Switzerland.

ELECTROCHEMICAL CHARACTERISATION OF AS-CAST Al-Zn-Sn AND Al-Zn-Mg-Sn ALLOYS FOR CORROSION CONTROL APPLICATION IN TROPICAL MARINE ENVIRONMENTS

Mahdi Che Isa[1*], Mohd Subhi Din Yati[1], Nik Hassanuddin Nik Yusoff[1], Mohd Moesli Muhammad[1], Mohd Fauzy Mohd Nor[2], Osmera Ismail[2] & Irwan Mohd Nor[1]

[1]Materials Research Group, Maritime Technology Division (BTM),
[2]Weapons Technology Division (BTP)
Science & Technology Research Institute for Defence (STRIDE), Ministry of Defence, Malaysia

[*]Email: mahdi.cheisa@stride.gov.my

ABSTRACT

Aluminum alloys are one of the important materials in the industry due to the uniqueness of their properties and the variety of their applications. In this study, Al-5.5Zn and Al-5.5Zn-2Mg alloys containing stanum (Sn) have been fabricated using the casting method. Electrochemical impedance spectroscopy (EIS) and electrochemical polarisation technique were used in the investigation of surface electrochemical and corrosion behaviours of the alloys in tropical seawater. Corrosion rate, and the relationship between open circuit potential and exposure time were determined. The results of the EIS study showed that Sn acted as an activating element to the aluminum alloys by lowering their surface impedance. The results were also supported by the data from corrosion rate measurement.

Keyword: *Aluminum alloy; corrosion rate; electrochemical impedance; stanum; open circuit potential (OCP).*

1. INTRODUCTION

Aluminum (Al) alloys are unique materials with a variety of applications, including for structural, industrial and manufacturing equipment, and transportation on land, sea and air. To date, the popularity of this alloy for various industrial applications is increasing due to the combination of several attractive features, such as low density, high strength to weight ratio, good electrical conductivity and ease of availability (Mahdi *et al*., 2011; Miller *et al*., 2000; Sanders *et al*., 2004). For marine environments, aluminum alloy has significant potential to be used as sacrificial anodes for corrosion protection. Although the application of aluminum as anodic

material is relatively new, it has good merit due to several advantages that can be exploited, such as lightweight, simple design, high theoretical value for current capacity (2800 Ah/kg) and readily available at low cost. Aluminum can be alloyed with modifier metals, such as zinc and magnesium, to achieve better physical and chemical characteristics, while at the same time, elements such as mercury, indium and titanium can be chosen an activator for specific marine applications (Salinas *et al*., 1999; Breslin *et al*., 1993).

However, the performance of aluminum anode is unpredictable because of the tendency of aluminum to passivate. According to previous researchers, aluminum anode efficiency is also affected by various factors such as alloys solidification process, defects and microstructures of alloys, heat treatment, chemical composition, and environment applied (Lin & Shih, 1987). To overcome the passivation process, alloying elements such as mercury or indium have been selected to improve the activation properties of aluminum alloy, but this is contrary to the sensitivity of environmental issues. While indium is a suitable candidate for activation purposes, it is an expensive material. Therefore, another metal needs to be studied for the activation process in marine environment. Mahdi *et al.* (2010) have shown the potential of stanum (Sn) as an activator base on the impedance characteristics of Al-Zn alloys in chloride environment. The selection of Sn as an alternative activator will require knowledge of fabrication techniques, solidification kinetics of precipitation and intermetallic compounds in the aluminum matrix. The purposes of this study are to fabricate aluminum alloys with the addition of Sn as an alloying element and to characterise the electrochemical behavior of these alloys using various electrochemical methods. The results will be correlated with the ability of Sn to act as an activator for aluminum alloys in marine applications.

2. MATERIALS AND METHODS

Aluminum alloys were prepared through mixing of high purity grade metals (99.9%) of Al, zinc (Zn), magnesium (Mg) and Sn by heating at 850 °C and pouring into steel molds to produce rods with diameter of 18 mm. In order to avoid trapped air in the mold and to prevent internal microstructure defects caused by voids and micropores during casting process, the mold is heated in a furnace at 150 º C. Melting and casting processes are carried out in an inert environment (argon gas) to avoid oxidation. The chemical compositions of the samples (Table 1) were determined using an Spectra AA-10 atomic absorption spectrometer (AAS) with analytical procedures based on the ASTM E34-98 standard (ASTM, 1998). A Bruker AXS X-ray diffractometer (XRD) with Cuk_{α} radiation sources was used to identify the existence of phases in the fabricated samples. The scanning process was carried out at 0.002 °/sec with 2θ scanning angle from 20° to 80°. The surface morphology of the samples before the electrochemical tests (as-polished) was obtained using a Carl Zeiss LSM 5 Pascal confocal laser scanning microscope.

The electrode used in the electrochemical characterisation had exposed area of 1 cm^2 and was embedded in epoxy resin. Corrosion behavior study for the samples in tropical sea water, with pH 8.2 and solution temperature of 27 °C, was performed using direct current and alternate current electrochemical polarisation methods.

Table 1: Chemical compositions of the Al-Zn and Al-Zn-Mg samples.

Alloy (nominal %wt.)	Contents (%wt.)				
	Zn	Mg	Sn	Fe	Al
Al-5.5Zn	5.47	-	-	0.03	Bal.
Al-5.5Zn-2Sn	5.48	-	1.72	0.03	Bal.
Al-5.5Zn-2Mg	5.58	1.82	-	0.03	Bal
Al-5.5Zn-2Mg-2Sn	5.52	1.79	1.95	0.03	Bal

Corrosion rates were determined from Tafel plots by sweeping the potential ± 250 mV from the corrosion potential E_{corr}. Open circuit potential (OCP) measurements were recorded for every 10 s for an immersion period of 15 h. For the alternating current (AC) electrochemical method, the electrochemical impedance spectroscopy (EIS) technique was carried out at frequency range of $1x10^{-3}$ Hz to $1x10^{5}$ Hz with alternating voltage of less than 10 mV. A standard three-electrode system consisting of a working electrode (alloy specimen), a counter electrode (high density graphite) and a reference electrode (saturated calomel electrode) was used. All the electrochemical experiments were carried out with instruments equipped with a Gamry PC4-750 potentiostat / galvanostat that were controlled by the Gamry Framework V4.2 software.

3. RESULTS AND DISCUSSION

3.1 Surface Morphology before the Electrochemical Test

Observations using the confocal laser scanning microscope on the as-polished samples were made to study the shape and distribution of precipitates that may exist or be present in these alloys. Figure 1 shows the micrographs of the as-cast samples before the electrochemical tests. The micrographs show that the samples containing Sn has more black precipitates, with the sizes of the precipitates found to be evenly distributed, as compared with the samples without Sn. From the confocal laser scanning microscopy analysis, it was found that the black precipitates in the samples with 2% Sn are 15-25 μm in diameter, and 2-10 μm for the samples without Sn. These findings are in agreement with the results reported by other researchers (Yuan *et al.* 2000; Guillaumin & Mankowski, 1998). Stanum (Sn) has a very low solid solubility in aluminum at both high or low temperatures (about 0.1% wt at 627 ^{o}C). Therefore, during the solidification process it will be rejected to the grain boundaries, between dendrites structures, forming intermetallic compounds or secondary phases.

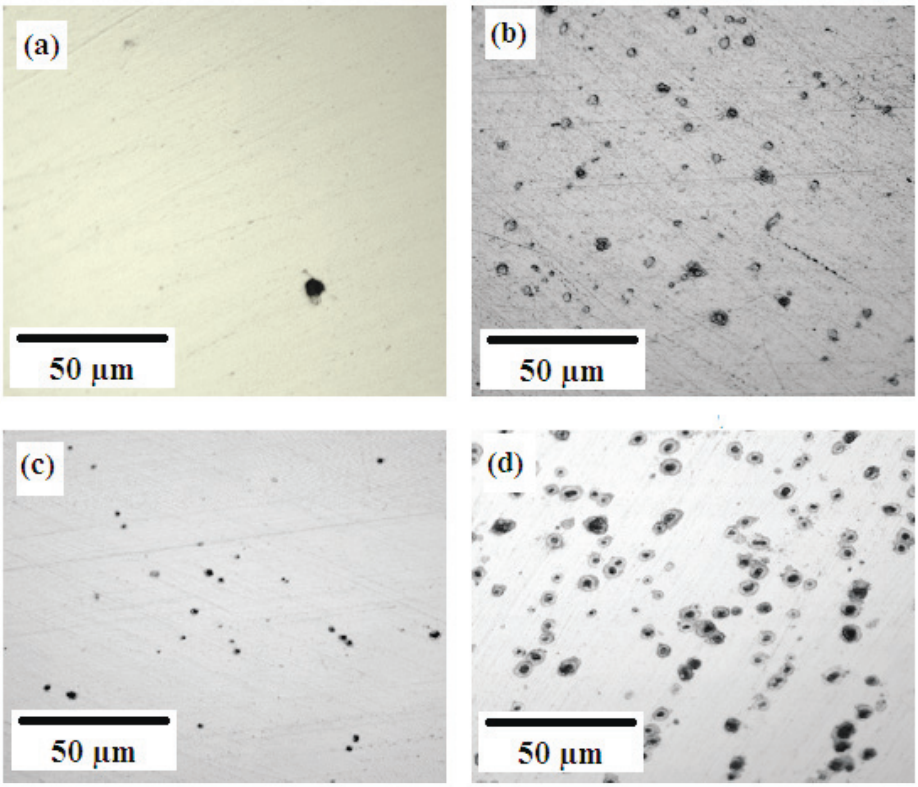

Figure 1: Confocal micrographs of the as-polished samples: (a) Al-5.5Zn; (b) Al-5.5Zn-2Sn; (c) Al-5.5Zn-2Mg; (d) Al-5.5Zn-2Mg-2Sn.

The presence of secondary phases was confirmed using XRD analysis, which indicates the presence of Mg_2Sn compounds in the Al-5.5Zn-2Mg-2Sn sample as shown in Figure 2. However, no secondary phases can be detected in the Al-5.5Zn-2Sn sample. XRD analysis found that the black precipitates are β-Sn phase as shown by the diffraction peak in Figure 2. The findings from microstructure and XRD data show that the presence of Sn clearly affects the surface structure of aluminum alloy. Defects on the alloy surface's oxide layer causes the surface of the alloy to become more active and prone to react with ionic species in aqueous solutions.

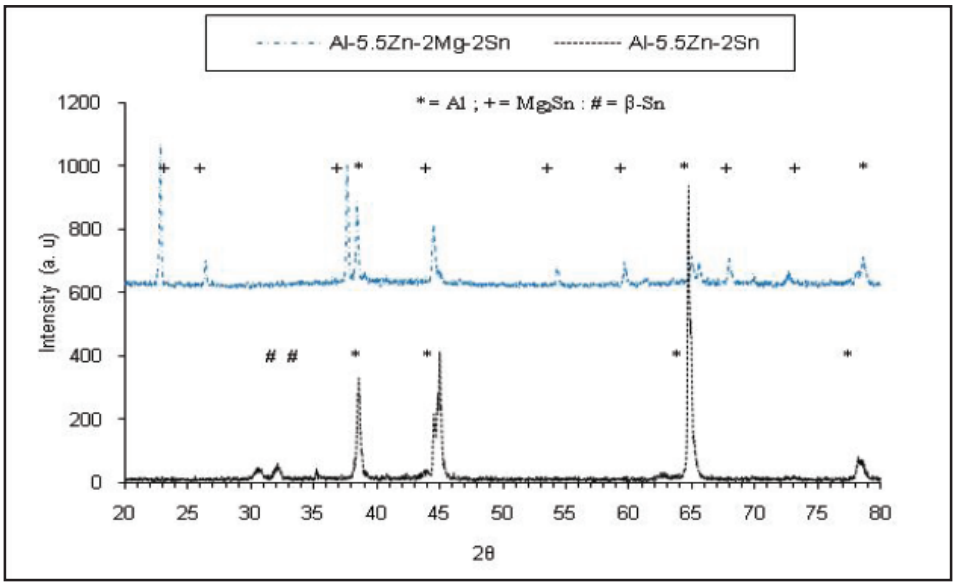

Figure 2: XRD spectrums for: Al-5.5Zn-2Mg-2Sn; and Al-5.5Zn-2Sn.

3.2 Electrochemical Measurements

The normal practice of monitoring the corrosion behavior of metals or alloys is by recording the values of OCP versus immersion time. Figures 3 and 4 show the effect of alloy composition on the OCP values for the Al-Zn-Sn and Al-Zn-Mg-Sn samples respectively. The average OCP values for the 15 h measurement are shown in Table 2. During initial state of immersion, the OCP values for both samples shifted towards the positive direction and only reached a stable value after approximately 5 h. These results indicate transient phenomena at the early stages of immersion before reaching a minimum voltage fluctuation in the range of 20-50 mV for the rest of the immersion period. The variation of OCP values observed in this study is a result of anodic and cathodic reactions occurring on the surface of the samples. The addition of Sn to the Al-5.5Zn sample resulted in potential shift in the electropositive direction due to the nature of Sn which is more cathodic than Al and Zn. On the other hand, the addition of 2% Mg to the Al-5.5Zn sample makes it more electronegative because Mg is an active metal.

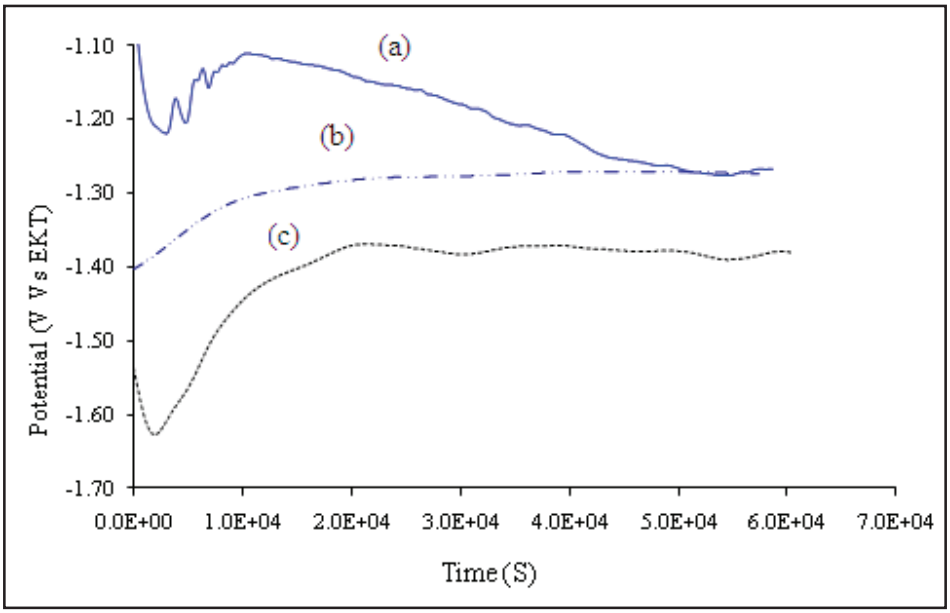

Figure 3: OCP versus immersion time in tropical sea water medium at 27 ºC: (a) Pure Al; (b) Al-5.5Zn-2Sn; (c) Al-5.5Zn.

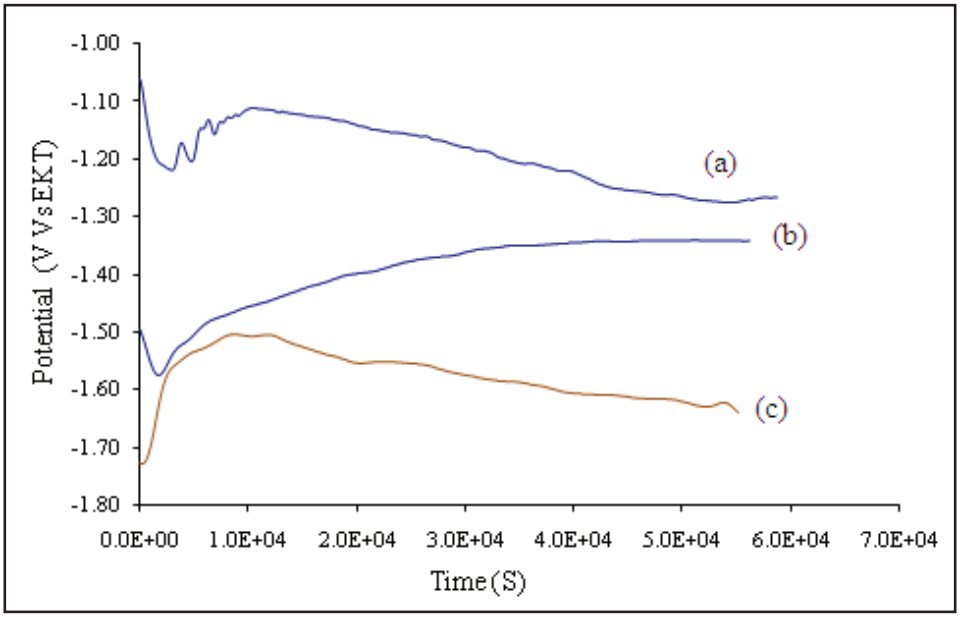

Figure 4: OCP versus immersion time in tropical sea water medium at 27 ºC: (a) Pure Al; (b) Al-5.5Zn-2Mg; (c) Al-5.5Zn-2Mg-2Sn.

Table 2: Average OCP values for the samples.

Sample	Open Circuit Potential (OCP) (V/SCE)
Pure Al	-1.23 ± 0.04
Al-5.5 Zn	-1.50 ± 0.05
Al-5.5Zn-2Sn	-1.33 ± 0.08
Al-5.5 Zn-2Mg	-1.40 ± 0.02
Al-5.5Zn-2Mg-2Sn	-1.62 ± 0.09

Corrosion resistance of aluminum alloys in aqueous medium can be evaluated based on polarisation resistance shown by the OCP values. Polarisation resistance depends on the condition of alloy's surface, such as the formation of oxide or hydroxide layer, which can prevent the interaction of the alloy with aggressive ionic species, thus increasing resistance of dissolution (Tang *et al*., 2011; Sebastián *et al*., 2011). If there is a strong protective and homogeneous oxide layer on the surface of the alloy, the corrosion resistance properties of the alloy would be very high. In short, electrical resistance at the surface of a metal or alloy is an important parameter that determines the nature of its corrosion resistance.

Aluminum is a very reactive metal and an oxide layer can form rapidly on the surface of its alloys when exposed or interacts with oxygen. When defects such as cracks, voids or holes are formed in the oxide layer, the active surface of the alloy is exposed to the medium (Zähr *et al*., 2011). Electrochemical impedance spectroscopy (EIS) can be used to examine the electrical resistance of the surface layer on a metal or alloy.

For aqueous electrochemical systems, polarisation resistance R_p is expressed as:

$$R_p = |Z_{\omega \to 0}| - |Z_{\omega \to \infty}| \quad (1)$$

where $|Z_{\omega \to \infty}|$ is the modulus of impedance that refers to the electrolyte resistance, while $|Z_{\omega \to 0}|$ | is the impedance modulus of the metal or alloy surface.

Figures 5 - 7 show the Nyquist plots for pure the Al, Al-5.5Zn and Al-5.5Zn-2Mg samples respectively after 1 to 8 h of immersion in the test solution. The EIS plots clearly show that the samples studied have different surface layer characteristics in term of polarisation resistance and capacitive behaviour. Both pure Al and alloy Al-5.5Zn showed similar resistance and capacitance behaviour at 1 h immersion. However, after 8 h of immersion, the Al-5.5Zn alloy clearly gives a lower impedance modulus, which indicates the presence of Zn in the alloy is able to change its electrochemical behavior. Nevertheless, when 2.0 wt.% Mg was added to Al-5.5Zn, there were increments in the both imaginary and real impedances. It is strongly believed that the presence of Mg can play a key role in forming a passive layer of known as $Mg(OH)_2$, as according to the following equations:

$$Mg \rightarrow Mg^{2+} + 2e^{-} \quad (2)$$

$$2H_2O + O_2 + 4e^{-} \rightarrow 4OH^{-} \quad (3)$$

The half reaction to Equations 2 and 3 gives the overall reaction:

$$Mg^{2+} + 2OH^{-} \rightarrow Mg(OH)_2 \quad (4)$$

The formation of this layer reduces electrochemical activities at the alloy surface due to increasing electrical resistance at the alloy-solution interface. The EIS results obtained from this study are in agreement with the average OCP values as shown in Table 2, which show that the presence of Mg in Al-5.5Zn results in the OCP values shifting towards a more electropositive direction. Aluminum alloys without Sn clearly show a much higher magnitude of impedance based on the observed values for resistance and capacitance compared to alloys containing Sn (Figures 5 and 6). For increasing immersion times, the samples without Sn showed lower impedance magnitudes based on size of semicircle due to the formation of more active sites or degradation of oxide layers. For the samples with Sn content, the semicircles in the Nyquist plots (Figures 5(b) and 6(b)) indicate the presence of inductive loops.

The presence of an inductive loop is caused by the process of adsorption and relaxation of Sn^{2+} species, or $Mg(OH)^{+}$ or $Mg(OH)_2$ generated by electrochemical activity on the surface of the alloy (Song *et el.*, 1997; Baril & Pebere, 2001). Impedance at low frequency refers to the charge or electron transfer process that results in an increase or decrease resistance. Increase in magnitude/of impedance values results in a bigger semicircule, which indicates high resistance to the flow of electron, whereas a smaller semicircle is achieved if the impedance is reduced. Therefore, based on the impedance diagram obtained in this study, Sn clearly plays a very important role as activator in helping the dissolution process of aluminum alloy in tropical sea water medium.

When aluminum alloy with a protective oxide layer is exposed to aggressive electrolyte, the impedance value is determined by the resistance (real impedance) and capacitance (imaginary impedance) of the layer. The presence of Sn, in the form of intermetallic Mg_2Sn for Al-Zn-Mg-Sn or β-Sn for Al-Zn-Sn, causes the oxide layer to form on the alloy surface have defects and inhomogenous chemical composition. This results in the electrical resistance at the location to be low so it will provide an advantage for initiation of corrosion or activation of the alloy. The results of this study are consistent with findings from Barbucci *et al.* (1998), which reported the role of intermetallic compounds in activating Al-Mg-Zn alloy.

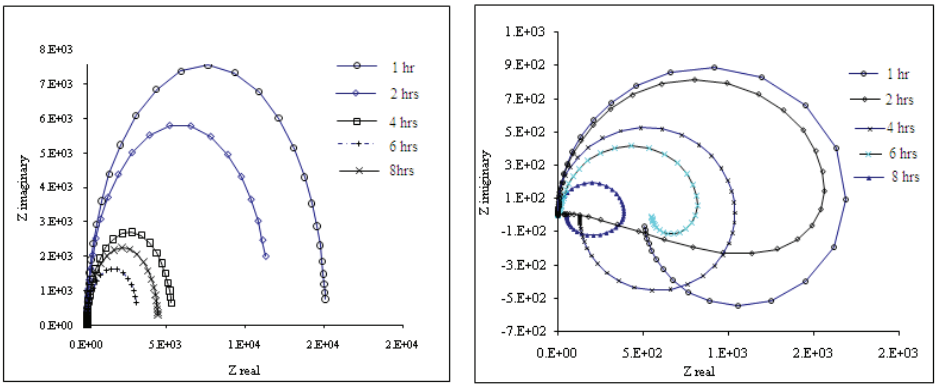

(a) **(b)**

Figure 5: Nyquist plots (EIS readings at OCP) for different immersion times for the samples: (a) Al-5.5Zn; (b) Al-5.5Zn-2Sn.

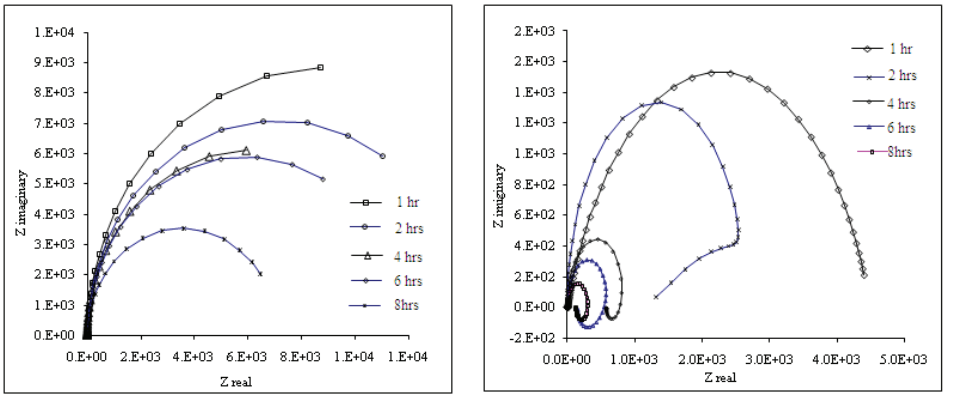

(a) **(b)**

Figure 6: Nyquist plots (EIS readings at OCP) for different immersion times for the samples: (a) Al-5.5Zn-2Mg; (b) Al-5.5Zn-2Mg-2Sn.

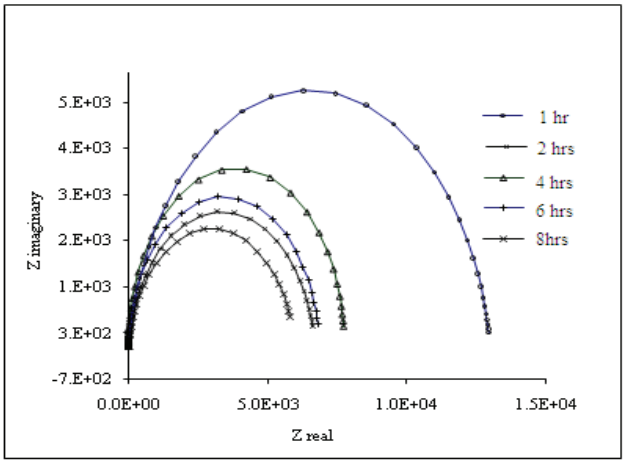

Figure 7: Nyquist plots (EIS readings at OCP) for different immersion times for different immersion times for pure Al.

From the Tafel plots, as shown in Figure 8, the presence of alloying elements Zn, Mg and Sn shifted the corrosion potential E_{corr} of the samples towards a more electronegative direction and anodic behaviour as compared to pure Al. The addition of Sn in the alloys significantly increased the rate of corrosion as compared to pure Al, Al-5.5Zn and Al-5.5-2Mg (Table 3). The formation of Mg_2Sn and β-Sn creates more local cathodic sites for further dissolution processes to take place during polarisation. The corrosion rate data of the samples also clearly supports the results obtained from the electrochemical impedance spectroscopy study which show that alloys with higher resistance and capacitance magnitudes produce lower rates of corrosion. These results further confirm that Sn plays the vital role as an activator in aluminum alloys, particularly aluminum alloys containing magnesium.

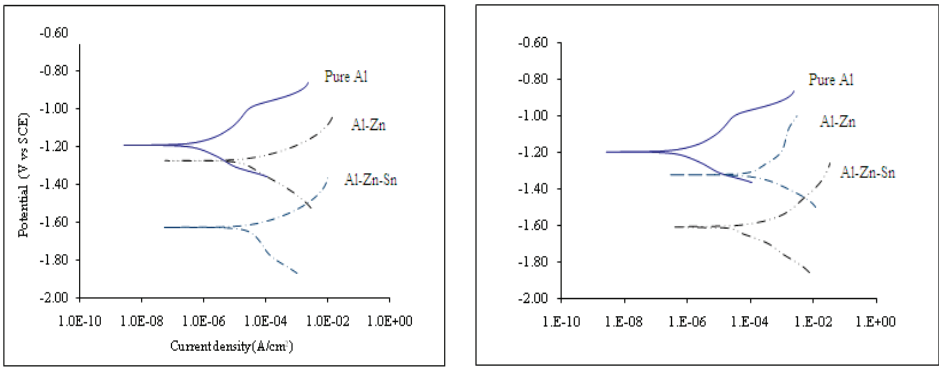

(a) **(b)**

Figure 8: Tafel plots for pure Al and aluminum alloys in tropical sea water medium, pH 8.2, temperature of 27 ºC: (a) Al-5.5Zn; (b) Al-5.5Zn-2Mg.

Table 3: Corrosion potential and rates obtained from the Tafel analysis.

Sample	E_{corr} (mV/SCE)	I_{corr} ($\mu A.cm^{-2}$)	Corrosion rate (μm/year)
Pure Al	-1200	1.2	$0.13x10^2$
Al-5.5Zn	-1660	23.2	$2.65\ x10^2$
Al-5.5Zn-2Sn	-1290	36.3	$4.15\ x10^2$
Al-5.5 Zn-2Mg	-1370	129.0	$14.79\ x10^2$
Al-5.5Zn-2Mg-2Sn	-1620	162.0	$18.53\ x10^2$

4. CONCLUSION

The electrochemical study of corrosion behavior for Al-Zn and Al-Zn-Mg alloys in tropical sea water medium has shown that the addition of alloying element Sn can act as activator to prevent aluminum alloy from passivating during the 15 h immersion test. The presence of Sn as β-Sn in Al-Zn and as Mg_2Sn in Al-Zn-Mg created oxide layers with defects and inhomogenous chemical composition. More defects and inhomogenities of protective oxide layer reduces the impedance properties of the alloys in aggressive electrolyte and at the same time, provide an activation effect by lowering resistance to polarisation and increasing the corrosion rates. The role of Sn as an activator in aluminum alloys is more pronounced with the presence of Mg in the alloy.

ACKNOWLEDGEMENTS

The authors wish to thank the Malaysian Government for the financial support and research facilities provided for this study. We also would like to express our appreciation to the staff of the Ship Technology Section and Weapons Technology Division, Science and Technology Research Institute of Defence (STRIDE), Ministry of Defence, Malaysia, for valuable discussions and support provided during the experimental stage and preparation of this manuscript.

REFERENCES

American Society for Testing and Materials (ATSM) (1998*). ASTM E 34-94: Standard Test Methods for Chemical Analysis of Aluminum and Aluminum Base Alloys*. American Society for Testing and Materials, Philadelphia, USA.

Barbucci, P., Cabot, L., Bruzzone, G. & Cerisola, G., (1998). Role of intermetallics in the activation of Al-Mg-Zn alloys. *J. Alloys Comp.*, **268:** 295-301.

Baril, G. & Pebere, N. (2001). The corrosion of pure magnesium in aerated and deaerated sodium sulphate solutions. *Corr. Sci.,* **43:** 471-484

Breslin, C. B., Friery, L. P. & Carrol, W. M.. (1993). Influence of impurity elements on electrochemical activity of aluminum activated by indium. *Corrosion,* **49**: 895-902.

Guillaumin, V. & Mankowski. G. (1998). Localized corrosion of 2024 T351 aluminum in chloride media. *Corr. Sci.,* **41:** 421-438.

Lin, J. C. & Shih, H. C., (1987). Improvement of the current efficiency of Al-Zn-In anode by heat treatment. *J. Electrochem. Soc*., **134**: 817-823.

Mahdi, C.I., Ahmad, M. Y., Daud, A. R. & Daud, M. (2010). The Effect of Sn on the impedance behavior of Al-Zn alloy in natural chloride solution. *Key Eng. Mat.* **442:** 322-329

Mahdi, C.I., Nik Hassanuddin Nik Yusoff, Mohd Subhi Din Yati, Mohd Moesli Muhammad & Irwan Mohd Nor (2011). Physical properties of Al-Zn-Mg-xSn Alloys: Hardness and electrical resistivity studies. *Defence S&T Tech. Bull.* **4:** 1-10.

Miller, W. S. Zhuang, L. Bottema, J. Wittebrood, A. J. De Smet, P. Haszler, A. & Vieregge A. (2000). Recent development in aluminium alloys for the automotive industry. *Mat. Sci.Eng.*, **280**: 37-49

Salinas, D. R., Garcia, S. G. & Bessone, J. B. (1999). Influence of alloying elements and microstructure on aluminum sacrificial anode performance: case of Al-Zn. *J.App. Electrochem.,* **29**: 1063-1071.

Sanders, Jr., R. E., Hollinshead, P. A. & Simielli, E. A. (2004). Industrial development of non-heat treatable aluminum alloys. *In* Nie, J.F., Morton, A.J. and Muddle, B.C. (Eds), *Materials Forum* 28, Institute of Materials Engineering Australasia Ltd., pp 53-64

Sebastián, F. Jr., Maffiotte, C., Samaniego, A., Galván, J. C. & Barranco, V. (2011). Effect of the chemistry and structure of the native oxide surface film on the corrosion properties of commercial AZ31 and AZ61 alloys. *Appl. Surf. Sci.*, **257**: 8558-8568

Song, G., Atrens, A., St. John, D., Wu, X. & Nairn, J. (1997). The anodic dissolution of magnesium in chloride and sulphate solutions. *Corr. Sci.,* **37:** 1981-2004.

Tang, J., Han, Z., Zuo, Y. & Tang, Y . (2011). A corrosion resistant cerium oxide based coating on aluminum alloy 2024 prepared by brush plating. *Appl. Surf. Sci.*, **257**: 2806-2812

Yuan, G. C., Li Z. J., Lou, Y. X. & Zhang, X. M., (2000). Study on crystallization and microstructure for new series of Al-Sn-Si alloys. *Mat. Sci. Eng.,* **A280:** 108-115.

Zähr, J., Oswald, S., Türpe, M., Ullrich, H.J. & Füssel U. (2011). Characterisation of oxide and hydroxide layers on technical aluminum materials using XPS. *Vacuum*, In Press.

FAULT DIAGNOSIS OF ROLLING-ELEMENT BEARINGS IN A GENERATOR USING ENVELOPE ANALYSIS

Mohd Moesli Muhammad*, Subhi Din Yati, Noor Arbiah Yahya & Noor Aishah Sa'at

Maritime Technology Division (BTM), Science and Technology Research Institute for Defence (STRIDE), Malaysia.

*moesli.muhammad@stride.gov.my

ABSTRACT

This paper presents the study of mechanical noise emitted by a naval ship's port generator using vibration analysis. Pre-inspection of the generator showed that the source of the abnormal noise was the alternator, which has two types of ball bearings, SKF 6226-C3 and SKF 6222-C3. Baseband time histories show that the port generator, with vibration accelerations above 20 m/s^2, is noisy as compared to the starboard generator, which is not facing any problems. Fast Fourier Transform (FFT) autospectrum analysis shows that the highest peak is obtained at frequency of 220 Hz, with maximum peak vibration acceleration of 7.47 m/s^2. Envelope analysis is used to detect the peak frequencies of the FFT autospectrum for comparison with the fault frequencies of both bearings. The peak at frequency of 110 Hz is identified as the ball pass frequency outer race (BPFO) of the SKF 6226-C3 bearing, with harmonics at 220 Hz and 330 Hz. The peaks of defect frequencies of the SKF 6222-C3 bearing were not detected, and thus, it can be concluded that the mechanical noise emitted by the port generator is caused by the SKF 6226-C3 bearing due to failure of its outer race. Sidebands grow around the BPFO frequency, indicating that the bearing is likely to be suffering a wear problem, and is entering stage 3 of bearing failure. It is recommended that the bearing be replaced before the deterioration enters stage 4 or catastrophic breakdown.

Keyword: *Generator; rolling-element bearing; defect frequencies; envelope analysis; Fast Fourier Transform (FFT).*

1. INTRODUCTION

Rolling-element bearings are critical parts of rotating machinery, and are among the most common of machine elements. Therefore, a lot of research has been conducted for many decades to study the cause of, and to analyse, bearing failures (Tandon & Choudhury, 1999; Grabulov *et al.*, 2010; Rafsanjani *et al.*, 2009; Kankar *et al.*, 2011). The main function of rolling-element bearings in machinery is to reduce rotational friction and support the loads from rotating shaft, thus allowing

efficient transmission of power. There are many types of rolling-element bearings, such as ball, roller, needle, and tapered and spherical rollers. The selection of types of rolling element bearings in machinery is based on load capacity, shaft diameter, rigidity and reliability (Budynas *et al.*, 2008).

Figure 1 shows the four components in rolling-element bearings that typically experience damage, which are rolling elements (balls / rollers), inner and outer races, and cage. Bearing vibration is usually dominated by low-frequency components caused by shaft rotation, stiffness variation and load fluctuations (Yang *et al.*, 2005). The characteristic defect frequencies are determined by shaft speed and bearing geometry. As shown in Figure 2, if the rotational speed of the races is constant, the value of defect frequencies is determined solely by the geometry of the bearing (Konstantin, 2002; Rai & Mohanty, 2007). The peak value at these frequency components are the features used in interpreting the bearing faults, which can be identified as follows:

i. Ball passing frequency outer race (*BPFO*): Local fault on the outer race.
ii. Ball passing frequency inner race *(BPFI*): Local fault on the inner race.
iii. Fundamental train frequency *(FTF*): Fault on the cage or mechanical looseness.
iv. Ball fault frequency (*BFF*): Local fault on the rolling elements. *BFF* is defined as:

$$BFF = 2 * BSF \tag{1}$$

where *BSF* is the ball spin frequency.

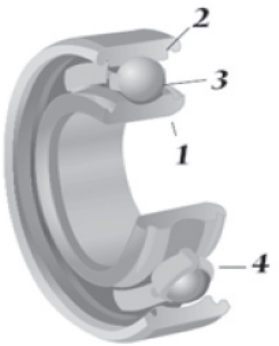

1. Inner race
2. Outer race
3. Balls
4. Cage

Figure 1: Components of rolling-element ball bearing (adapted from NTN, 1994).

These bearing fault frequencies are expressed in Equations 2 - 6. In these equations, n is the number of balls / rollers, and f_r is the shaft speed. In some cases, the defect frequencies calculated using these equations deviate from those which are obtained by measurement. This is because these equations use the shaft speed that

is provided by the manufacturer, but the actual shaft speed may be different during vibration measurement (Orhan *et al.*, 2006).

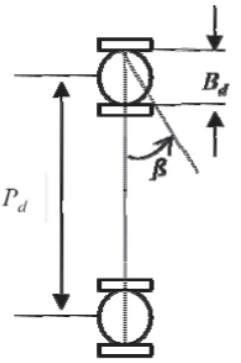

B_d: Ball diameter
P_d: Pitch diameter
β: Contact angle

Figure 2: Geometry of a rolling-element bearing (adapted from NTN, 1994).

$$BPFO = \frac{n}{2} f_r \left(1 - \frac{B_d}{P_d} \cos \beta \right) \tag{2}$$

$$BPFI = \frac{n}{2} f_r \left(1 + \frac{B_d}{P_d} \cos \beta \right) \tag{3}$$

$$BFF = \frac{P_d}{B_d} f_r \left(1 - \left(\frac{B_d}{P_d} \cos \beta \right)^2 \right) \tag{4}$$

$$BSF = \frac{P_d}{2B_d} f_r \left(1 - \left(\frac{B_d}{P_d} \cos \beta \right)^2 \right) \tag{5}$$

$$FTF = \frac{f_r}{2} \left(1 - \frac{B_d}{2} \cos \beta \right) \tag{6}$$

When a defect or local fault occurs on the inner / outer race or rolling elements, the interaction between the race and rolling elements generates time varying and non-uniform discontinuous forces that cause vibrations. As a result, the vibration signals become amplitude modulated each time contact with the defect is made. Figure 3 shows the impact that results when a localised defect present on the surface of a bearing strikes another surface, causing an excitation of the resonances of the bearing and overall mechanical system. The vibration signal from the early stage of a defective bearing may be masked by machine noise, making it difficult to detect the fault using spectrum analysis alone. This becomes more difficult when the signal from the bearing is relatively low in energy and buried within other high frequency vibrations of rotational components such as gear-mesh and blade pass. At this stage, it is not easy to interpret and relate the high amplitudes of the signals in the original spectrum to the fault severity (Zhang *et al.*, 2008; Sheen, 2010).

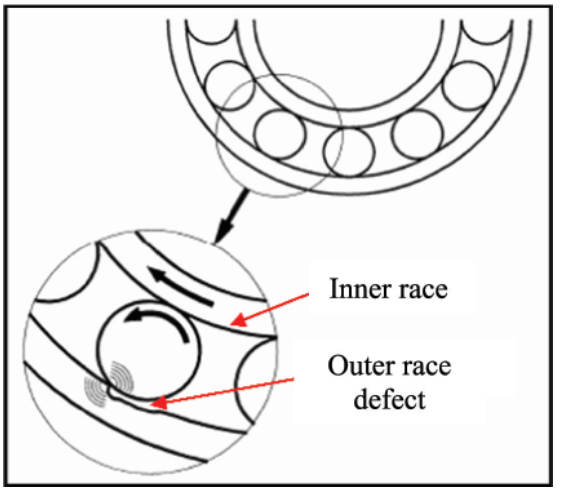

Figure 3: A defect in the outer race causes a shock impulse to spread through the bearing's components and machine structure (adapted from Courrech, 2003).

Envelope analysis is a technique that is used to filter out low frequency rotational signals, and to extract and enhance the repetitive components of bearing defect signals (SKF, 2000; Randall *et al.*, 2011). This technique is able to distinguish between different bearing faults associated with individual components. In this process, suspected high frequency resonance excitation caused by a local bearing is extracted, while low amplitude high frequency harmonics of bearing defect frequencies are shifted into a low frequency range. These components are enhanced while suppressing higher amplitude harmonics of rotational components and random broadband noise. This post-processed signal can then be examined and further analysed in the frequency domain to define the peak of bearing defect frequencies.

This paper presents the study of mechanical noise emitted from a naval ship's port generator. The primary purpose of this study is to employ envelope analysis to analyse and detect the defect frequencies of components of rolling-element bearings in the generator.

2. METHODOLOGY

A diesel generator generally consists of a diesel engine as the prime mover and an alternator as a converter to convert the mechanical energy to electrical energy, with both being connected to each other through a flexible coupling. In this study, the port engine was investigated due to an alarming abnormal sound which started, and then, increased. Pre-inspection of the generator showed that the source of the abnormal noise was the alternator. The shaft in the alternator is supported by two types of ball bearings, SKF 6226-C3 and SKF 6222-C3, where each bearing is located at different points. The bearing specifications are shown in Table 1. As a reference, the starboard generator, which was not facing any problems, was measured to compare the peak levels of vibrations.

Table 1: Specifications of ball bearings which support the shaft of the alternator (SKF, 2009).

Parameter	SKF 6226-C3	SKF 6222-C3
Ball diameter B_d (mm)	32	29
Pitch diameter P_d (mm)	180	155
Number of balls n	9	10
Contact angle β (°)	0	0

The measurements were acquired for both the port and starboard generators in three directions using a Bruel and Kjaer (B&K) type 4321 triaxial charge accelerometer, with sensitivity of 10 pc/g and a dynamic range of 0.1 to 12 kHz. The three axes of measurements were x (horizontal), y (vertical) and z (axial). The x- and y- axes, which represent radial or rotational axes, are the two perpendicular axes in the plane of rotation, while the z-axis is the direction in line with, or parallel to, the shaft. The output of the accelerometer was fed to a B&K converter 2647A, which was connected to a Portable Pulse 3560B front-end analyzer (5-channel input and 1-channel output). The generator was run at constant speed of 1,800 RPM or 30 Hz shaft revolutions for 5 minutes before the measurements were taken. All other machineries within the vicinity of the generator were switched off in order to reduce the background noise.

The schematic diagram of the diesel generator and the location of the accelerometer is shown in Figure 4. The accelerometer was mounted using a magnetic mount and positioned perpendicular to the alternator bearing housing.

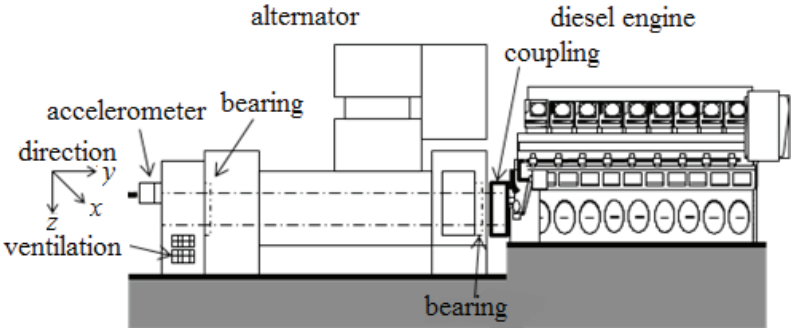

Figure 4: Location of the accelerometer.

The collected data was analysed using Pulse Labshop, Version 10.3, with the sampling frequency of the signal set to 6.4 kHz and resolution of 1,600 lines. The spectrum signal was sampled using exponential mode with averages of 10, while time weighting was set to Hanning window. The post-processing of the envelope spectrum span was set to frequency of 1 kHz and resolution of 1,600 lines, giving the delta frequency Δf a value of 625 mHz.

The data was analysed by comparing the Fast Fourier Transform (FFT) autospectrums of the port and starboard generators. High frequencies in the FFT autospectrum which are suspected to be caused by the bearings are identified and extracted for envelope analysis to define the peak frequencies for comparison with the bearing fault frequencies in Table 2.

Table 2: Characteristic defect frequencies calculated using Equations 2 - 6.

Defect	Defect Frequency (Hz)	
	SKF 6226-C3	SKF 6222-C3
Fundamental train frequency *FTF*	12	12.2
Ball spin frequency *BSF*	82	77
Ball fault frequency *BFF*	164	155
Ball passing frequency outer race *BPFO*	110	122
Ball passing frequency inner race *BPFI*	159	178

3. RESULTS AND DISCUSSION

Figure 5 displays the baseband time histories of the port and starboard generators. It is observed that the baseband time history of the port generator is quite noisy as compared to the starboard generator. The average amplitude of the port generator is high and above 20 m/s^2, whereas for the starboard generator, it is below 20 m/s^2. The signals in both baseband time histories are dominated by noise. Therefore, no significant part of the repeated pulse of impact faults caused by the components of the port generator can be recognised or detected.

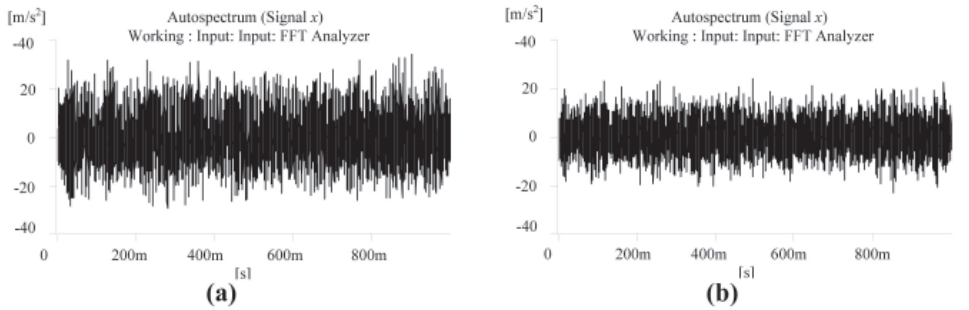

Figure 5: Baseband time histories of the (a) port and (b) starboard generators.

Figure 6 shows the overall level of vibration acceleration in root mean square (RMS) of the port and starboard generators for each of the three axes. The port generator showed high vibrations in all three axes, in which *y*-axis is only slightly lower than *x* -axis, with the *x*- and *y*-axes having higher levels than the *z*-axis. The graph also shows that the overall levels of the starboard generator are very close to one another for the three axes, with the range between the maximum and minimum being 0.6 m/s^2.

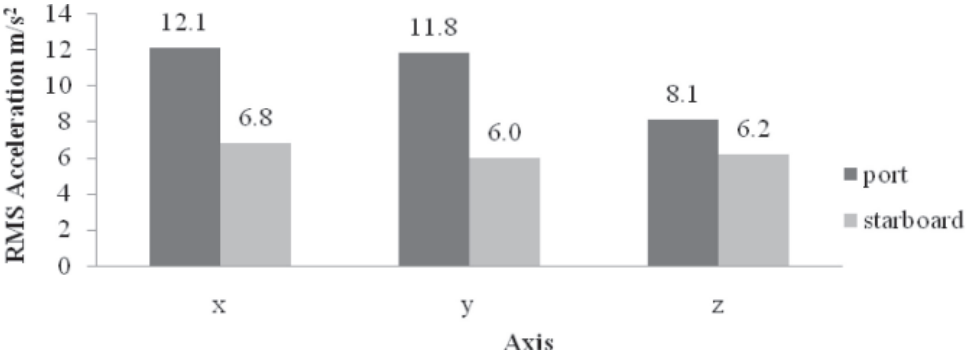

Figure 6: Overall level of vibration acceleration in RMS of port and starboard generators.

Figure 7 shows the FFT autospectrums of the *x*-, *y*- and *z*- axes of the port and starboard generators. The results show the same trend as the RMS values obtained; that the port generator exhibits higher levels of vibrations as compared to the starboard generator. Most of the high peaks of the three axes of the port generator are obtained at frequency ranges below 400 Hz, with vibration accelerations of over 3 m/s^2.

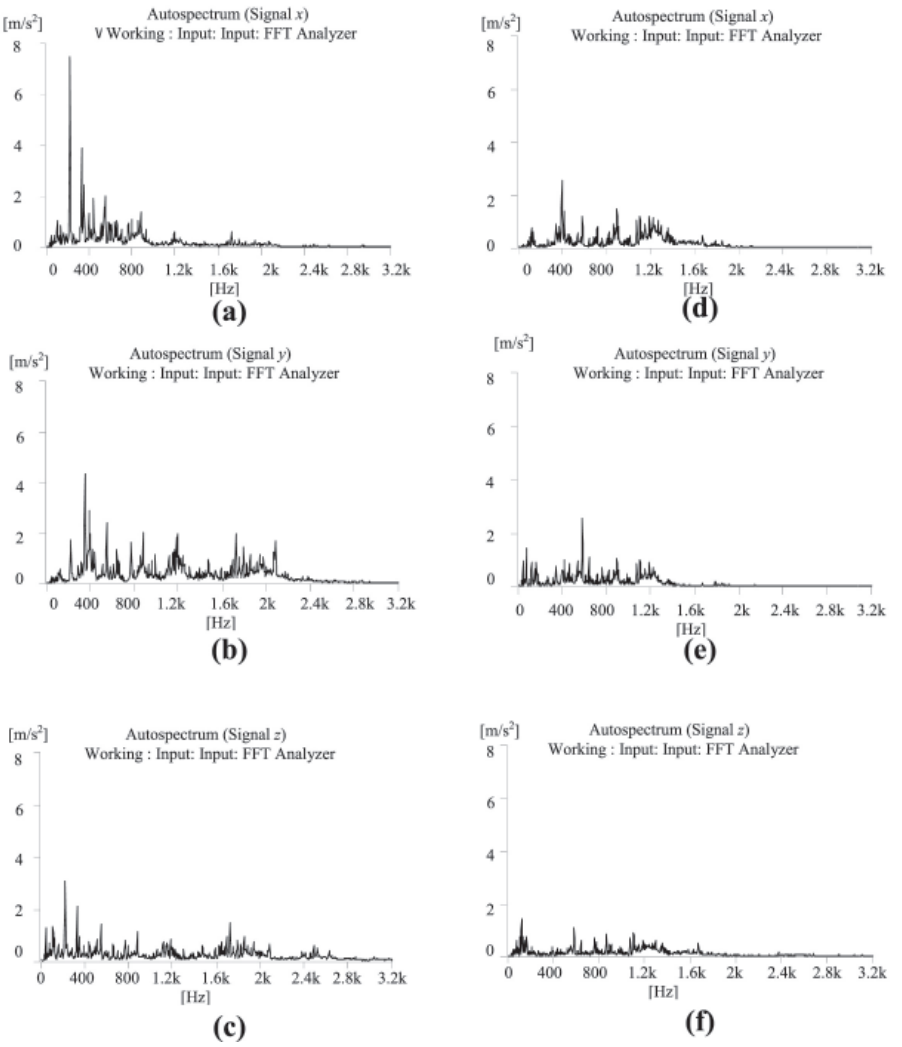

Figure 7: FFT autospectrums of the two generators: (a) *x*-; (b) *y*-; and (c) *z*- axes of the port. (d) *x*-; (e) *y*-; and (f) *z*- axes of the starboard.

Examination of the zoomed FFT autospectrums (0 - 1 kHz) of the three axes of the port generator in Figure 8 shows that the highest peak occurred at the *x*- axis with frequency of 220 Hz and vibration acceleration of 7.47 m/s^2. This indicates the possibility that the problem with the port generator may be due to bearing fault occurring at the *x*- axis, meaning that the fault frequencies may be from the rotational axis and probably comes from inner or outer race fault impacts.

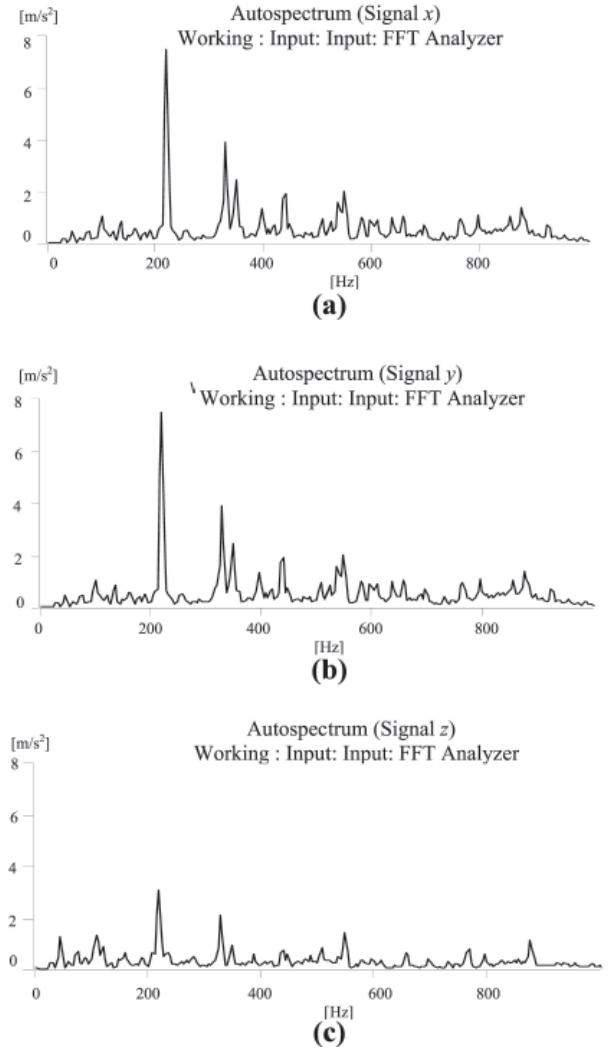

Figure 8: Zoomed FFT autospectrums (0 – 1 kHz) of the (a) *x*-; (b) *y-;* and (c) *z*- axes of the port generator.

In order to verify that the peak at frequency of 220 Hz is contributed by fault of the ball bearings, the FFT autospectrums of the port generator were filtered out using the envelope technique, with their envelope spectrums shown in Figure 9. In analysing the envelope spectrums, the absolute peak level is not considered, as the main objective is to examine the peaks at the bearing frequencies indicated in Table 2. The peak at frequency of 110 Hz is identified as the *BPFO* of the SKF 6226-C3 bearing, with harmonics at 220 Hz and 330 Hz. The peaks of defect frequencies of the SKF 6222-C3 bearing were not detected, and thus, it can be concluded that the mechanical noise emitted by the port generator is caused by the SKF 6226-C3 bearing due to failure of its outer race.

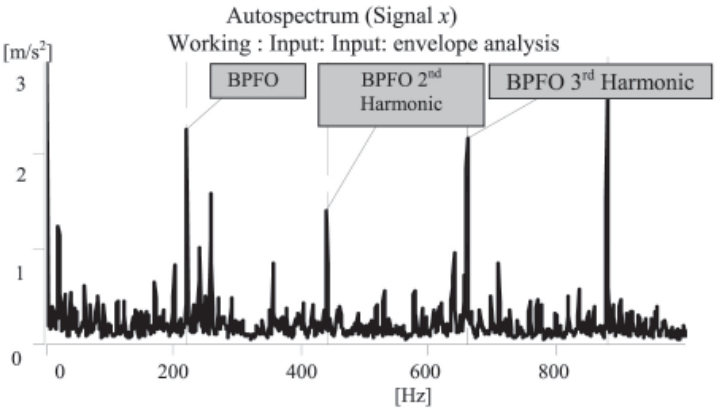

(a)

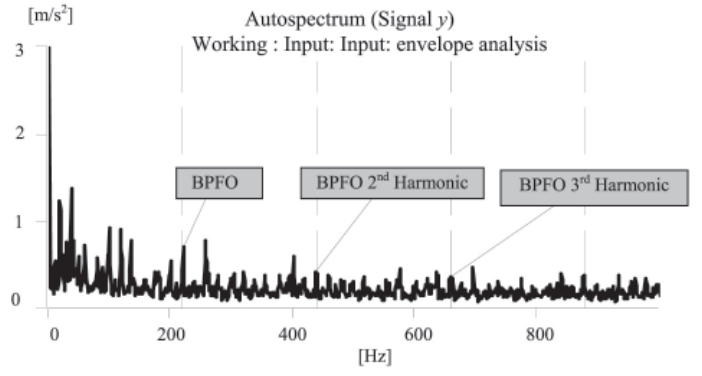

(b)

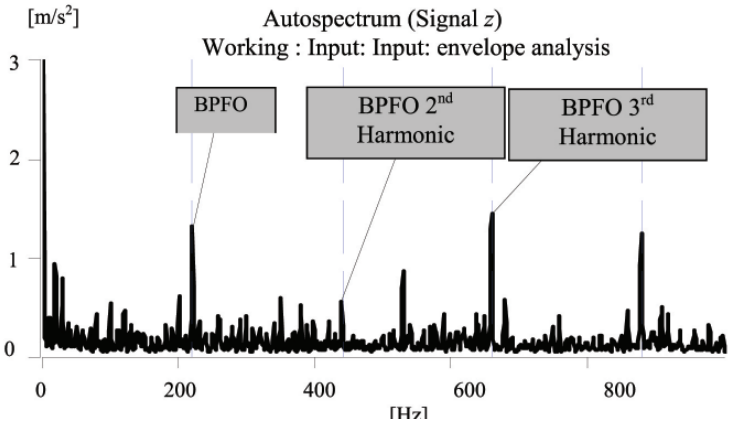

Figure 9: Envelope spectrums of the (a) *x*-; (b) *y-;* and (c) *z*- axes of the port generator.

The occurrence of growing number of sidebands around the *BPFO* defect frequency (Figure 10) is evidence of severe defects in the bearing. The bearing is likely to be suffering a wear problem and is entering stage 3 of bearing failure. At this stage, the rate of wear becomes highly unpredictable. The remaining life of the bearings will largely depend on its lubrication, temperature, cleanliness and dynamic loads being imposed upon it by vibration forces from imbalance, misalignment etc. At this point, there will be noticeable change in sound level and frequency, and slight increase in bearing housing temperature (Berry, 2002). It is recommended that the bearing be replaced before it enters stage 4 of bearing failure, which indicates that the bearing is approaching catastrophic failure. At this stage, the remaining life of the bearing will be unpredictable due to unexpected failure; it may be able to be operated for a week, or could fail within an hour. The bearing should not be allowed to operate in order to avoid a sudden catastrophic breakdown.

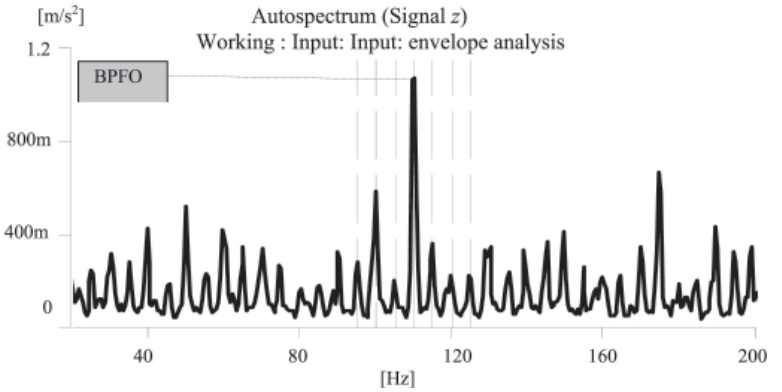

Figure 10: A number of sidebands, with separations of 5 Hz, grow around the *BPFO* defect frequency of the SKF 6226-C3 bearing.

4. CONCLUSION

The findings of the vibration analysis conducted determined that the mechanical noise emitted by the port generator was caused by failure of the SKF 6226-C3 bearing. The results indicate that the bearing is suffering a wear problem and is entering stage 3 of bearing failure. It is proposed that the bearing be replaced before the deterioration enters stage 4 or catastrophic breakdown.

ACKNOWLEDGEMENTS

This study was conducted as part of the Ninth Malaysia Plan (RMK9) project entitled *Royal Malaysian Navy Ship Propulsion System Condition Based Monitoring*. The authors would like to thank the Science and Technology Research Institute for Defence (STRIDE) for providing research facilities and technical assistance. The authors also gratefully acknowledge the officers and personnel of the Royal Malaysian Navy (RMN) for their support and cooperation during the course of the study.

REFERENCES

Berry, J.E. (2002). *How to Implement an Effective Condition Monitoring Program Using Vibration Analysis*. Technical Associates of Charlotte Inc., USA.

Budynas, R.G. & Nisbett, J.K. (2008). *Shigley's Mechanical Engineering Design*. McGraw Hill Companies Inc, New York, USA.

Courrech, J. (2003). *Envelope Analysis for Effective Rolling-Element Bearing Fault Detection – Fact or Fiction?* Bruel and Kjear Vibro, Denmark.

Grabulov, A., Petrov, R. & Zandbergen H.W. (2010). EBSD Investigation of The Crack Initiation and TEM/FIB Analyses of The Microstructural Changes Around The Cracks Formed Under Rolling Contact Fatigue (RCF). *Int. J. Fatigue*, **32**: 576-583.

Kankar, P.K., Sharma, S. C. & Harsha, S. P. (2011). Rolling Element Bearing Fault Diagnosis Using Wavelet Transform. *Neurocomputing*, **74**: 1638-1645.

Konstantin, H. (2002). *Envelope Analysis of Local Faults in Rolling Element Bearings*. Bruel & Kjaer, Naerum, Denmark.

NTN (1994). *An introduction Introduction to Ball Bearings*. NTN Bearing Corporation, Mount Prospect, USA.

Orhan, S., Aktu¨rk, N. & Celik, V. (2006). Vibration Monitoring for Defect Diagnosis of Rolling Element Bearings As A Predictive Maintenance Tool: Comprehensive Case Studies. *NDT&E Int*, **39**: 293–298.

Rafsanjani, A., Abbasion, S., Farshidianfar, A. & Moeenfard, H. (2009). Nonlinear Dynamic Modeling of Surface Defects in Rolling Element Bearing Systems. *J. Sound Vib.*, **319**: 1150-1174.

Rai, V.K. & Mohanty, A.R. (2007). Bearing Fault Diagnosis Using FFT of Intrinsic Mode Functions In Hilbert Huang Transform. *Mech. Syst. Signal Pr.*, **21:** 2607-2615.

Randall, R. B. & Antoni, J. (2011). Rolling Element Bearing Diagnostics – A Tutorial. *Mech. Syst. Signal Pr.,* **25**: 485-520.

Sheen, Y. T. (2010). An Envelope Analysis Based on The Resonance Modes of The Mechanical System For The Bearing Defect Diagnosis. *Measurement*, **43**: 912-934.

SKF. (2000). *Vibration Diagnostic Guide*. SKF Reliability Systems, Gothernburg, Sweden.

SKF. (2009). *SKF Interactive Engineering Catalogue*. Available online at: http://www.skf.com/portal/skf/home/products?maincatalogue=1&newlink=first&lang=en (Last access date: 12 October 2009).

Tandon, N. & Choudhury, A. (1999). A review of vibration and acoustic measurement methods for the detection of defects in rolling element bearings. *Tribol. Int.,* **32**: 469–480.

Yang, H., Mathew, J. & Ma, L. (2005). Fault Diagnosis of Rolling Element Bearings Using Basis Pursuit. *Mech. Syst. Signal Pr.*, **19**: 341–356.

Zhang, B., Georgoulas, G., Orchard, M., Saxena, A., Brown, D., Vachtsevanos, G. & Liang, S. (2008). Rolling Element Bearing Feature Extraction and Anomaly Detection Based on Vibration Monitoring. *16th Mediterranean Conference on Control and Automation*. 25-27 June 2008, Congress Centre, Ajaccio, France.

FINITE ELEMENT ANALYSIS (FEA) OF A TEAR-DROP SHAPED UNMANNED UNDERWATER VEHICLE (UUV)

Fadzli Ibrahim[1*] & Mohd Fauzy Mohd Nor[2]

[1]Mechanical & Aerospace Technology Division (BTJA)
[2]Weapons Technology Division (BTP)
Science and Technology Research Institute for Defence (STRIDE), Ministry of Defence, Malaysia

[*]E-mail: fadzli.ibrahim@stride.gov.my

ABSTRACT

This paper provides a case study on the structural integrity of a tear-drop shaped unmanned underwater vehicle (UUV) using finite element analysis (FEA). The overall design in terms of shape and load arrangement was subject to suitability for the purpose of underwater inspection and observation. This preliminary design study covers both the mainframe and external body of the UUV. Aluminium 6061 was initially selected as the material for the mainframe, while low density polyethylene (LDPE) was selected for the external body. The results of FEA simulations and matrix analyses show that the overall design with the chosen materials is suitable for further studies and development. However, it is proposed that further research be conducted on vehicle stability and performance in non-ideal environments using computational fluid dynamics (CFD) simulations and subsequently with experimental analysis by developing an actual prototype.

Keywords: *Unmanned underwater vehicle (UUV); tear-drop shape; material selection; finite element analysis (FEA); matrix analysis.*

1. INTRODUCTION

Stress analysis is an engineering discipline that determines stress in materials and structures subjected to static or dynamic forces or loads. It is required for the study and design of structures, such as mechanical parts and structural frames, under given or expected loads. Stress analysis can be applied as a design step for structures that do not yet exist (Hibler, 2005).

A FEA system consists of a computer model of a design or material that is stressed and analysed for specific results. It is used to verify that a suggested design will be able to perform to the required specifications prior to construction or manufacturing. FEA discretises solid bodies into small and finite volumes called finite elements, where elasticity principles can be easily applied. Its procedure

requires a pre-processing operation that converts a computer aided design (CAD) model into a discretised form known as mesh. A solver then is used to evaluate the various equations formed from the mesh. A post-processing module is finally used for the interpretation of the results obtained (Zienkiewicz *et al*., 2005; Rao, 2010).

This paper provides a case study on the structural integrity of the UUV using FEA. A tear-drop shape design was selected in order to have good manoeuvrability and smooth fluid flow for the purpose of underwater observation and inspection (Alvarez *et al*., 2009). The overall weight (in air) of the UUV, including the mainframe, should not exceed 100 kg, while the overall dimensions should be less than 1 m in length, 1 m in width and 0.5 m in height, or 0.5 m^3 in volume. The basic configuration for payloads should cover a built-in controller, two units of thrusters, batteries, underwater lighting, underwater camera / video, a depth sensor and a gyro compass. This preliminary design study covers both the external body and mainframe of the UUV.

In order to conduct this investigation, CAD is used in combination with computer aided engineering (CAE). This project starts with solid modelling using a CAD parametric software, CATIA V5 R19. The generated model is then analysed using a CAE analysis software, Msc. Patran-Nastran.

Msc. Patran is a pre / post-processing software for FEA, providing solid modelling, meshing and analysis setup tools that streamline the creation of analysis ready models for use by Msc. Nastran, which is a FEA solver. Msc. Nastran is designed to simulate stress, dynamics or vibration of complex systems. The integration of both softwares provides sufficiently accurate results to evaluate the performance of products (Msc. Software, 2011).

2. DESIGN

The UUV was designed for underwater observation in Malaysian seas, specifically in the Strait of Malacca. As the Strait of Malacca is shallow and narrow, with average depth of 53 m (Kassim *et al*., 2007), the proposed operational depth of the UUV was 50 m. This was considered as a reasonable depth for initial development, with the requirement expected to be increased for future projects, such as operation in the South China Sea which has an average depth of 120 m.

The main concern for the mainframe structure is to have sufficient room for easy housing, accessibility and maintenance of components. The mainframe should also be designed modularly for future changes or upgrades (Rahim *et al*., 2010; Hussain *et al*., 2011). The overall conceptual design was established in order to have a rough idea of the arranwgement of all the equipment for the purpose of load analysis (Figure 1).

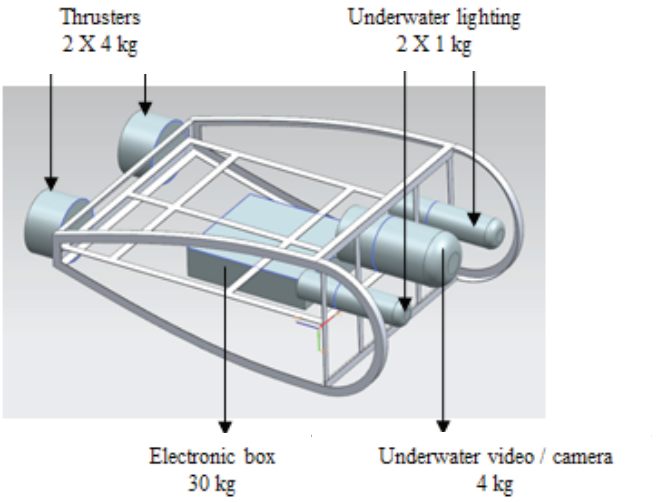

Figure 1: Estimated load arrangement for the UUV design.

As the UUV will be subjected to saltwater environments, it is crucial to select materials that are corrosion resistant, light and strong, but with acceptable cost for manufacturing. The initial materials chosen were aluminium 6061 (Al 6061) for the mainframe and LDPE for the external body, though further analysis should be conducted to ensure the suitability of the materials.

3. FEA SIMULATIONS

The preliminary design of the UUV was based on various choices of materials which was analysed using FEA simulations. This is crucial in order to determine that the chosen material could withstand the given pressure or force. The results of the simulations were compared with yield strength in order to ensure that the computed maximum deflection and stress do not exceed the maximum limit (in this case, referring to the material plasticity region).

The proposed UUV has to withstand water pressure of up to depth of 50 m. This operational depth was used to determine the thickness and construction of the pressure compartment. The maximum pressure P that should be withstood is:

$$\text{Pressure } P = P_{atm} + \rho g h \quad (1)$$
$$= 101.325 \text{ kPa} + 1000 \text{ kg/m}^3 \text{ x } 9.81 \text{ m/s}^2 \text{ x } 50 \text{ m}$$
$$= 0.4906 \text{ MPa}$$

where P_{atm} is atmospheric pressure, ρ is the density of water, g is gravity acceleration and h is depth.

As the UUV is yet to be manufactured and the costs of materials is not a primary concern, using a relatively high value of safety factor is acceptable in order to increase confidence levels and to ensure that the material chosen shall withstand the given pressure (Mac Donald, 2007; Shigley *et al*., 1989). Hence, using a safety factor of 2.5, the maximum pressure to be withstood will be:

Pressure P = 2.5 x 0.4906
= 1.23 MPa

This pressure value will considered as acting on the overall perpendicular surface of the external body and mainframe. Tables 1 and 2 show the data used for the FEA analysis. Examples of the simulations conducted are shown in Figures 2 and 3, while the results obtained are shown in Tables 3 and 4. For all the materials for the external body, maximum displacement and stress occurred at nodes 16,888 and 12,084 respectively, while for all the materials for the mainframe, maximum displacement and stress occurred at nodes 18,033 and 16,131 respectively.

Table 1: Properties of materials that were considered for the external body (Source: George *et al.*, 2002; Hibler, 2005).

Material	Modulus of Elasticity *E* (GPa)	Poisson Ratio *v*	Density (g/cc)
Low Density Polyethylene (LDPE)	0.315	0.45	0.922
Polycarbonate	2.36	0.37	1.20
Fibreglass (E-Glass)	73.0	0.33	2.60
Perspex (Acrylic)	2.76	0.39	1.19

Table 2: Properties of materials that were considered for the mainframe (Source: George *et al.*, 2002; Hibler, 2005).

Material	Modulus of Elasticity *E* (GPa)	Poisson Ratio *v*	Density (g/cc)
Aluminium 6061 (Al 6061)	68.9	0.33	2.70
Stainless Steel (SS304)	193	0.29	8.00
Alloy Steel	205	0.29	7.85
Titanium	116	0.34	4.50

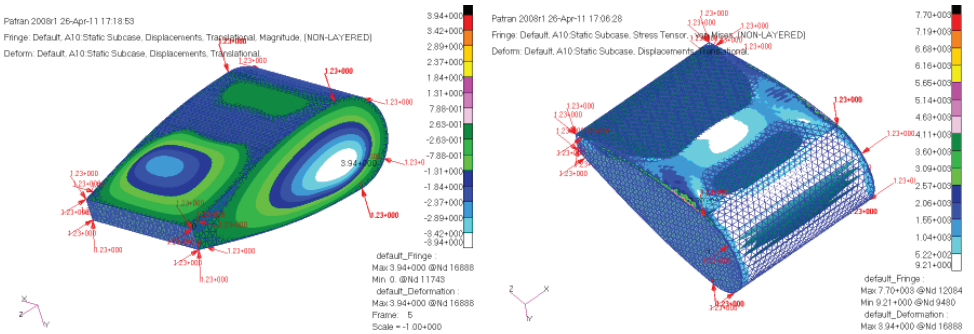

(a) (b)

Figure 2: FEA simulations conducted for the external body using LDPE: (a) Maximum displacement; (b) Maximum stress.

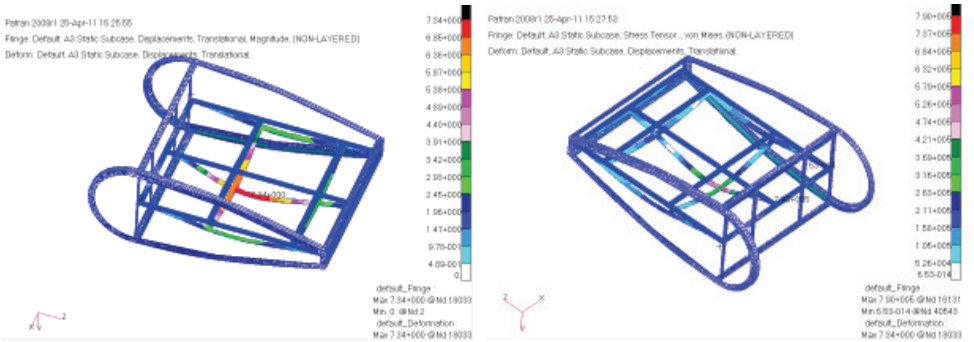

(a) (b)

Figure 3: FEA simulations conducted for the mainframe using aluminium 6061: (a) Maximum displacement; (b) Maximum stress.

Table 3: Results of FEA simulations for materials for the external body.

Material	Maximum deflection (mm)	Maximum stress (kPa)	Yield Strength (MPa)
Low density polyethylene (LDPE)	3.94	7.70	11.2
Polycarbonate	0.637	8.49	64.3
Fibreglass	0.0216	8.71	1900
Perspex	0.528	8.36	68.9

Table 4: Results of FEA simulations for materials for the mainframe.

Material	Maximum deflection (mm)	Maximum stress (MPa)	Yield Strength (MPa)
Aluminium 6061 (Al 6061)	7.34	0.790	55.2
Stainless Steel (SS304)	2.62	0.791	215
Alloy Steel	2.46	0.791	435
Titanium	4.36	0.789	140

From the results obtained, it is clear that the maximum deflection and stress obtained from the FEA simulations for all the materials, for both the external body and mainframe, do not exceed the materials' yield strengths. Since the safety factors for all the chosen materials in terms of material deflection and stress have been complied (i.e. all the materials are able to withstand the given pressure / forces), the materials can be directly compared with each other during selection.

4. MATRIX ANALYSIS

Matrix analysis was employed to select the best material for the external body and mainframe. This was performed by setting 'corrosion resistance' as the highest weightage of the criterion since it is the most important factor that directly affects the UUV's design. 'Relative cost' is set as the lowest weightage of criterion since this project will not considered for manufacturing, though it could become a future objective.

The trade-off analyses that were conducted to form the matrix analyses are as shown in Tables 5 and 6. The results obtained show that the total marks for the external body materials are comparatively similar, with LDPE receiving the highest marks. For the mainframe, aluminium 6061 is the most suitable option to be selected. These results prove that the initial selection that was made can be reasonably accepted for further development.

Table 5: Trade-off analysis for materials for the external body.

Property	Weightage	Fibreglass	LDPE	Perspex	Polycarbonate
Yield Strength (MPa)	4	5	3	3	3
Density (g/ cm^3)	3	2	5	4	4
Fabrication	2	3	4	3	2
Corrosion resistance	6	5	5	5	5
Magnetic susceptibility	5	5	5	5	5
Relative cost	1	4	4	3	1
TOTAL MARKS		**91**	**94**	**88**	**84**

Scale:

1 : Very Good; 2 : Good; 3 : Moderate; 4 : Fair; 5 : 5 Poor

Table 6: Trade-off analysis for materials for the mainframe.

Property	Weightage	Stainless steel 304	Aluminium 6061	Steel alloy	Titanium
Yield Strength (MPa)	4	3	2	4	3
Density (g/ cm^3)	3	1	5	1	4
Fabrication	2	4	5	5	4
Corrosion resistance	6	4	4	1	4
Magnetic susceptibility	5	3	4	1	2
Relative cost	1	4	5	5	1
TOTAL MARKS		**66**	**82**	**45**	**67**

Scale:

1 : Very Good; 2 : Good; 3 : Moderate; 4 : Fair; 5 : 5 Poor

5. CONCLUSION AND RECOMMENDATIONS

This study was conducted to verify the suitability of the preliminary design of a tear-drop shaped UUV. FEA simulations conducted on the UUV, with the selected material profiles, show that it can sufficiently withstand the given pressure at depth of 50 m. The results of the matrix analysis confirm that aluminium 6061 and LDPE are comparatively suitable for the mainframe and external body respectively. On the whole, the proposed design of the UUV with the materials selected is theoretically suitable for further development.

Future work should include the study of vehicle stability and performance in non-ideal environments, including the effect of currents and wakes. In order to realise this, the UUV's design should be guided using CFD simulations in order to yield a hydrodynamic optimum configuration i.e. manoeuvrability and low drag. Analysis on other related sub-systems, such as propulsion, electronics, control and communications systems, should also be included.

REFERENCES

Alvarez, A., Bertram, V. & Gualdesi, L. (2009). Hull hydrodynamic optimization of autonomous underwater vehicles operating at snorkeling depth. *Ocean Eng.,* **36**: 105-112.

George, S.B., Henry, R.C. & John, A.V. (2002). *Materials Handbook, 15th Edition*. McGraw Hill Companies, New York.

Hibler, R.C., (2005). *Mechanic of Materials*. Prentice Hall, New York.

Hussain, N.A.A., Ibrahim, F., Nasuddin, N.M., Yaacob, R., Naim, H.M., Sulaiman, N.E.S., Ramli, R., Rashid, M.R.M., Ramle, I., Ismail, A.S., Louisnaden, E. & Ibrahim, N.A. (2011). Rekabentuk dan pembangunan sebuah kenderaan robotik bawah air (*remotely operated vehicle*). *Defence S&T Tech. Bull.,* **4**: 77-91.

Kassim, K.Y., Ahmad, A. & Mahyam, M.I. (2007). *Keadaan Laut Perairan Semenanjung Malaysia Untuk Panduan Nelayan.* Malaysia Fisheries Department, Terengganu.

Mac Donald, B.J., (2007). *Practical Stress Analysis with Finite Elements.* Glasnevin, Dublin.

Msc. Software (2011). *Patran : FE Modeling and Pre/Post Processing*. Available online at: http://www.mscsoftware.com/Products/CAE-Tools/Patran.aspx (Last access date: 15 April 2011)

Rahim, K.I.A., Othman, A.R. & Arshad, M.R. (2010). Pressure hull development using hybrid composite with metal liner concept. *3rd International Conference on Underwater System Technology: Theory and Application 2010 (USYS'10)*, 162-167.

Rao, P.N. (2010). *CAD/CAM Principles and Applications 3rd Edition*. McGraw Hill, New Delhi.

Shigley, J.E. & Mischke, C.R. (1989). *Mechanical Engineering Design 5th Edition.* McGraw Hill Companies, Singapore.

Zienkiewicz, O.C., Taylor, R.L., & Zhu, J.Z. (2005). *The Finite Element Method: Its Basis & Fundamentals*. Elsevier, Burlington.

DEVELOPMENT OF A MINI REMOTELY OPERATED VEHICLE (ROV) FOR UNDERWATER TRAINING

Nur Afande Ali Hussain, Norazlina Md Nasuddin, Nor Emi Salwani Sulaiman, Rosdi Yaacob, Rozi Ramli, Mohd Ridzuan Mohd Rashid, Idayu Ramle, Ayu Sahida Ismail, Elizabeth Louisnaden & Nor Alyani Ibrahim

Maritime Technology Division (BTM), Science & Technology Research Institute for Defence (STRIDE), Ministry of Defence, Malaysia.

*Email: afande.hussain@stride.gov.my

ABSTRACT

This paper presents the design and development of a mini remotely operated vehicle (ROV) system for training purposes at the STRIDE Maritime Technology Division (BTM). The mini ROV is designed for operation in shallow water environments and is capable to dive up to 5.6 m depth. Based on the concept design developed using Solidworks, the buoyancy force and stability required to overcome the total weight of the platform was planned by tuning the locations of the thrusters and electronics compartment. The fabrication processes were divided into several developments including the controller system, thrusters and mainframe. The field test of the mini ROV was conducted successfully in the KD Duyong training pool, with no leakage problems occurring in the electronics compartment. However, manoeuvring difficulties were found at 5 m depth, as the thrusters needed to overcome the surrounding water pressure. This can be overcome using DC motors with the higher rating of motor torque.

Keywords: *Mini remotely operated vehicle (ROV); Solidworks; thrusters; controller system; mainframe.*

1. INTRODUCTION

Underwater environment investigations often require the use of unmanned underwater vehicles (UUVs) to perform survey, exploration, monitoring and data collection. In general, UUVs can be classified into two categories, which are remotely operated vehicles (ROVs) and autonomous underwater vehicles (AUVs) (Yuh, 2000; Zain *et al.*, 2004; Antonelli *et al.*, 2008; Muljowidodo *et al.*, 2010). A mini ROV can be classified based on the total weight of the vehicle being not more than 15 kg (Lobecker & Nicholson, 2000; Stepanek & Conger, 2009). Mini ROVs can conduct similar functions as larger UUVs, while being cheaper and easier to build and maintain (Brundage *et al.*, 2006). This platform can be transported, and operated by one person without any additional operators.

The STRIDE Maritime Technology Division's (BTM) previous ROV prototype (Ali Hussain *et al.*, 2011), a general class ROV for underwater inspection purposes, is currently under development. Its total weight is 37 kg and is suitable to dive up to 50 m depth. A mini ROV platform offers similar manoeuvring conditions as the general purpose ROV and can allow ROV pilots to develop underwater control and navigation skills. Hence, it was determined that a mini ROV platform is the best solution for our ROV pilot training programme. The mini ROV platform will also be used as a supporting vehicle for the general purpose ROV, while performing additional missions and tasks.

The design and development of the mini ROV involved 2D and 3D modelling Solidworks design, and selection of suitable body frame material, propulsion type, underwater cables and power system. The Solidworks environment allows the user to plan the overall design and develop ideas into the final design prototype. Based on buoyancy calculation, only three thrusters are needed for this prototype due to its size and weight. Brushed DC motors and twisted pair cables are the best solution for the thrusters and underwater cable systems respectively based on size and performance. A direct control scheme is implemented by changing the DC motor rotation for underwater manoeuvring. We managed to design a simple underwater housing and sealing method to prevent any water leakage during the field test. Materials and parts selected for the project are based on cost, market availability and simplicity in the fabrication process.

2. DESIGN AND DEVELOPMENT

The platform is designed to operate with low power consumption, and hence, proper material and propulsion system should be selected to meet the weight and buoyancy requirements of the vehicle. The proposed operational depth of the platform was limited to 6 m in order to reduce voltage drop and ohmic losses in the underwater cable. The platform frame is made up of PVC pipes with dimensions of 40 cm x 30 cm x 18 cm with respect to length, width and height. PVC was chosen because it is a light weight material, low in cost, has proven design in underwater conditions (Ahmad, 2005) and is easy to work with.

In order to reduce total power consumption, the platform employs only three thrusters, with two thrusters used for horizontal movements, and the other thruster used for vertical movements. The concept design was developed using Solidworks, with suitable PVC material size being selected (Figures 1 and 2). The thrusters' allocations is designed to counter rolling effects and added mass. The payload is limited for only for an electronics compartment, which is made using acrylic housing, with several LED lights being mounted together to indicate electronic status and conditions.

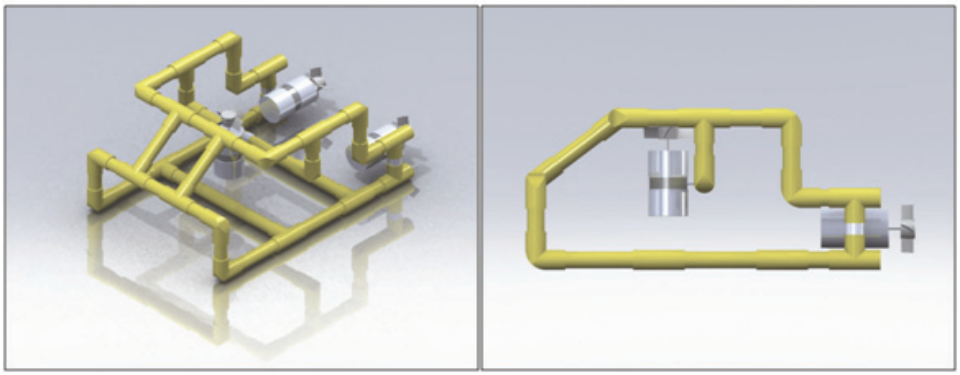

Figure 1: 3D concept design of the mini ROV platform.

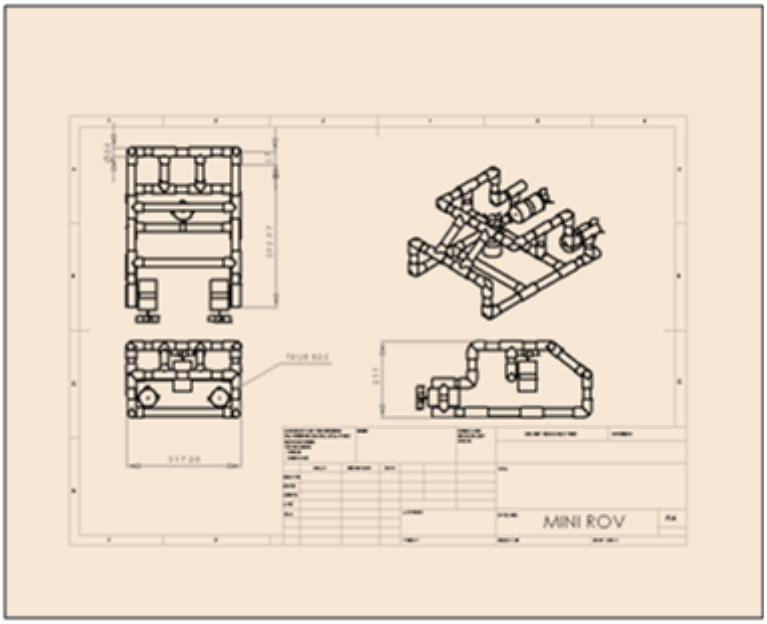

Figure 2: 2D drawing of the mini ROV platform.

In order to overcome the downward force of the mainframe, cylinder shaped buoys, made from polyurethane, are attached onto the mini ROV mainframe as shown in Figure 3. The total length of the buoyancy material is 34 cm with diameter of 4 cm. The buoyancy system is designed for the platform to have slightly positive buoyancy so that it is easy for the platform to dive, and float slowly when the vertical thrusters are in idle position (Ali Hussain *et al.*, 2009; Arima *et al.*, 2009)

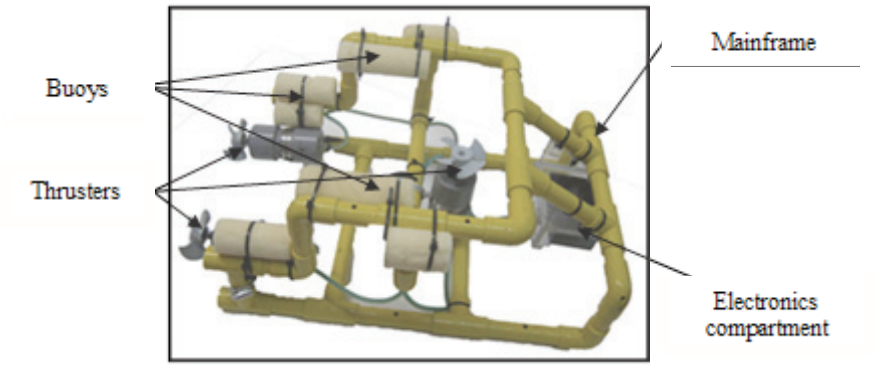

Figure 3: The mini ROV platform with buoyancies attached.

3. SYSTEM DESIGN

The overall system of the mini ROV consists of the controller station, power system and mainframe as shown in Figure 4. The controller station consists of an electronic box for electronic controller housing. The schematic representation of the system design is shown in Figure 4. The main component of the mini ROV control system is the controller box, which is made with special PVC casing with dimensions of 16 cm x 12 cm x 8 cm with respect to length, width and height. The power source for the platform is a 12V lead acid battery that provides power for the thrusters through a UTP CAT 5 cable. This cable was chosen as it has proven performance in underwater missions (Abidin *et al.*, 2011) and is capable to support eight independent cables in a single UTP CAT 5 cable.

3.1 Controller System

The main components of the mini ROV's control system (Figure 5) are the controller box, PCB board and wiring connections. The controller box acts as a controller where all signals from the user via the control unit are processed and transmitted to the PCB. The controller box provides waterproof protection for the PCB board and other electronic instruments. The controller box is designed using a switching analogue mechanism, instead of the joystick approach usually used for ROVs, due to its robustness and simplicity. In order to control the vertical movements of the mini ROV, the user needs to control the push buttons on the controller box. The toggle switches are used to control horizontal movements.

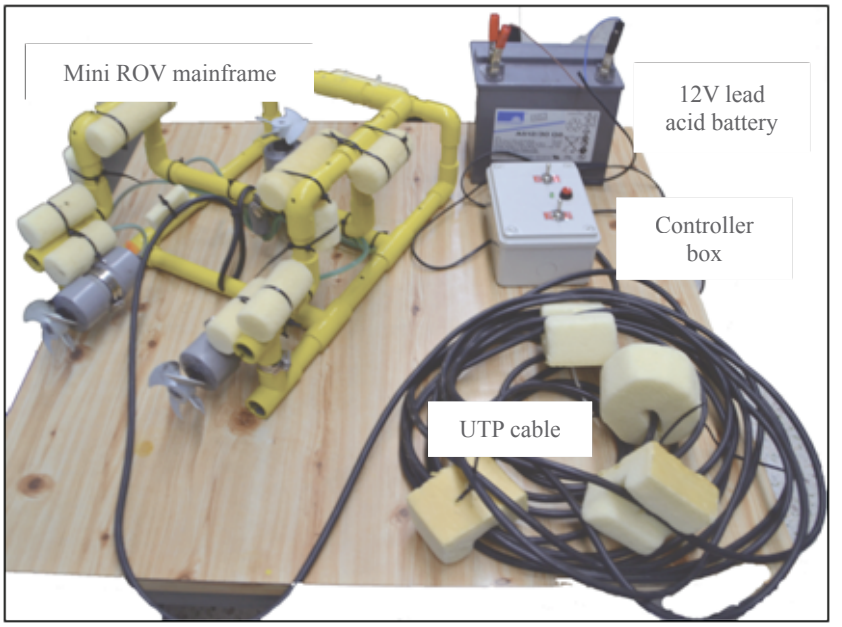

Figure 4: The mini ROV system.

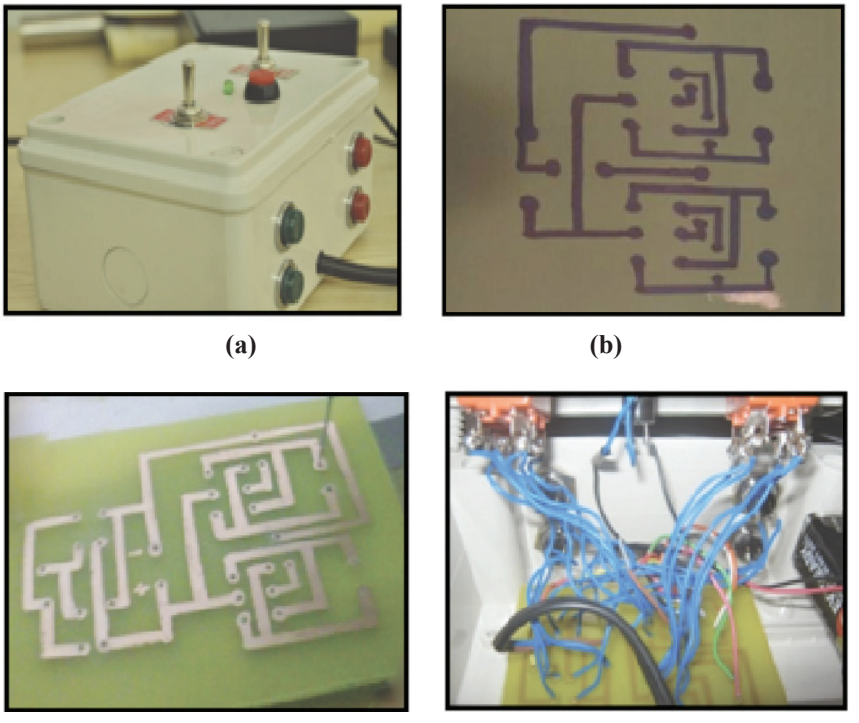

(a) **(b)**

(c) **(d)**

Figure 5: The mini ROV's controller system: (a) Controller box; (b) PCB schematic; (c) PCB under fabrication; (d) Wiring connection.

The button and toggle switches for configuration of control signals can be seen in Figure 6. In order to dive, both dive buttons need to be pushed, while to float, both float buttons should be pushed. These sequences will rotate the vertical underwater thruster clockwise (CW) for floating and counter clockwise (CCW) for diving sequence. For the horizontal thrusters, for forward direction, both toggle switches need to be in up position for CW rotation of the thrusters, while for backwards direction, the toggle switches should be in the down position for CCW rotation of the thrusters.

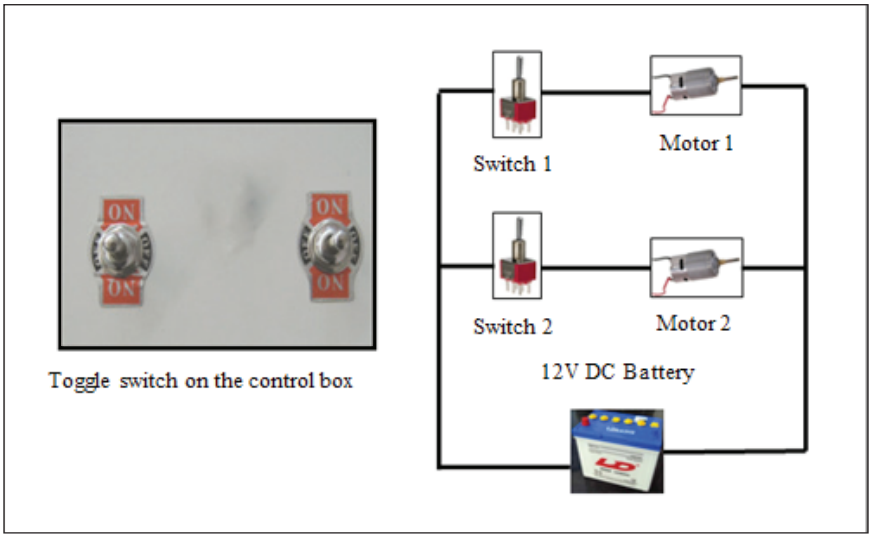

(a)

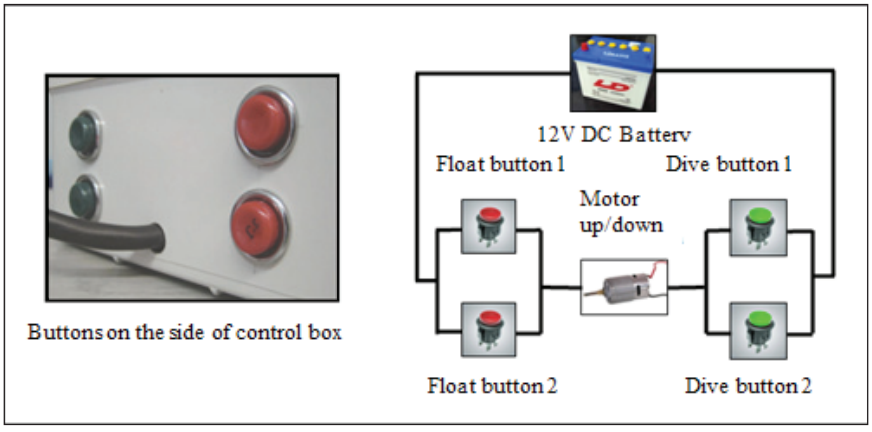

(b)

Figure 6: The mini ROV's thrusters control system: (a) Buttons for vertical movement; (b) Toggle switches for horizontal movement.

3.2 Development of Thrusters

Each thruster is made using a Mabuchi TD 038827 DC brush motor and PVC material selected for the motor's watertight compartment. The DC motor is capable of operating at no load speed of 23400 rpm, which can provide 1998 g.cm of torque.

Each fabricated thruster was tested inside a water tank to ensure that there is proper water resistance between the motor shaft and PVC housing to avoid leakage. The shafts need to be applied with grease for each underwater testing to prevent any water absorption into the DC motor. Each thruster is powered using a 12V DC, 1.5 A power source, and its speed can be controlled using a command signal from the controller box via the UTP cable. The shafts and propellers were fabricated according to our requirements. Figure 7 shows the details of the design and development of the thrusters.

(a)

(b)

(c)

(d)

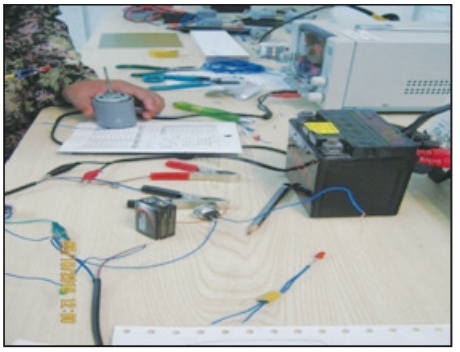

(e) **(f)**

Figure 7: Design and development of the mini ROV's thrusters: (a) Shaft fabrication; (b) Fabricated shafts; (c) Shaft integration with DC motor; (d) PVC underwater housing; (e) Motor functionality test; (f) Sealing process.

Figure 8 shows one of the completed thrusters. The underwater PVC housing is made of PVC pipe with length of 10 cm and diameter of 5 cm. The diameter of the propeller is 7 cm.

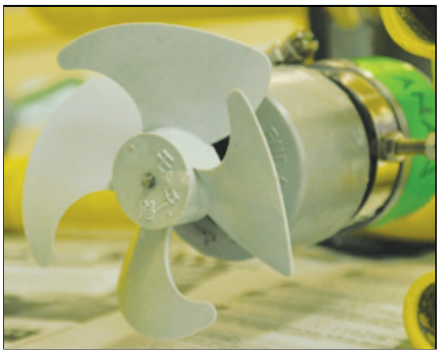

Figure 8: A completed thruster, consisting of a Mabuchi DC motor with PVC housing.

3.3 Mainframe Development

The development and fabrication of the mini ROV's mainframe can be divided into three main activities, which are measuring and cutting PVC material based on the Solidworks 3D and 2D design, painting the PVC pieces, and installation of the pieces into the complete mini ROV mainframe. These activities were conducted in the BTM mechanical workshop, with detailed description provided in Figure 9.

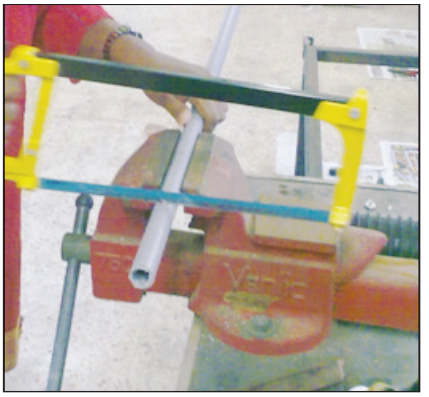

(a)

(b)

(c)

(d)

Figure 9: Development and fabrication of the mini ROV's main frame: (a) PVC pipe measurement and cutting; (b) Drilling; (c) Installation and painting; (d) The complete mainframe.

4. FIELD TEST

The field test of the mini ROV was conducted at the KD Duyong training pool in the Royal Malaysian Navy's (RMN) Lumut Base (Figure 10). We successfully conducted the test for the hardware and control systems without any leakage problems in the electronics compartment. The test was conducted for pool's maximum depth of 5.6 m. Manoeuvring difficulties were found at 5 m depth, as the thrusters needed to overcome the surrounding water pressure. This can be overcome using DC motors with the higher rating of motor torque.

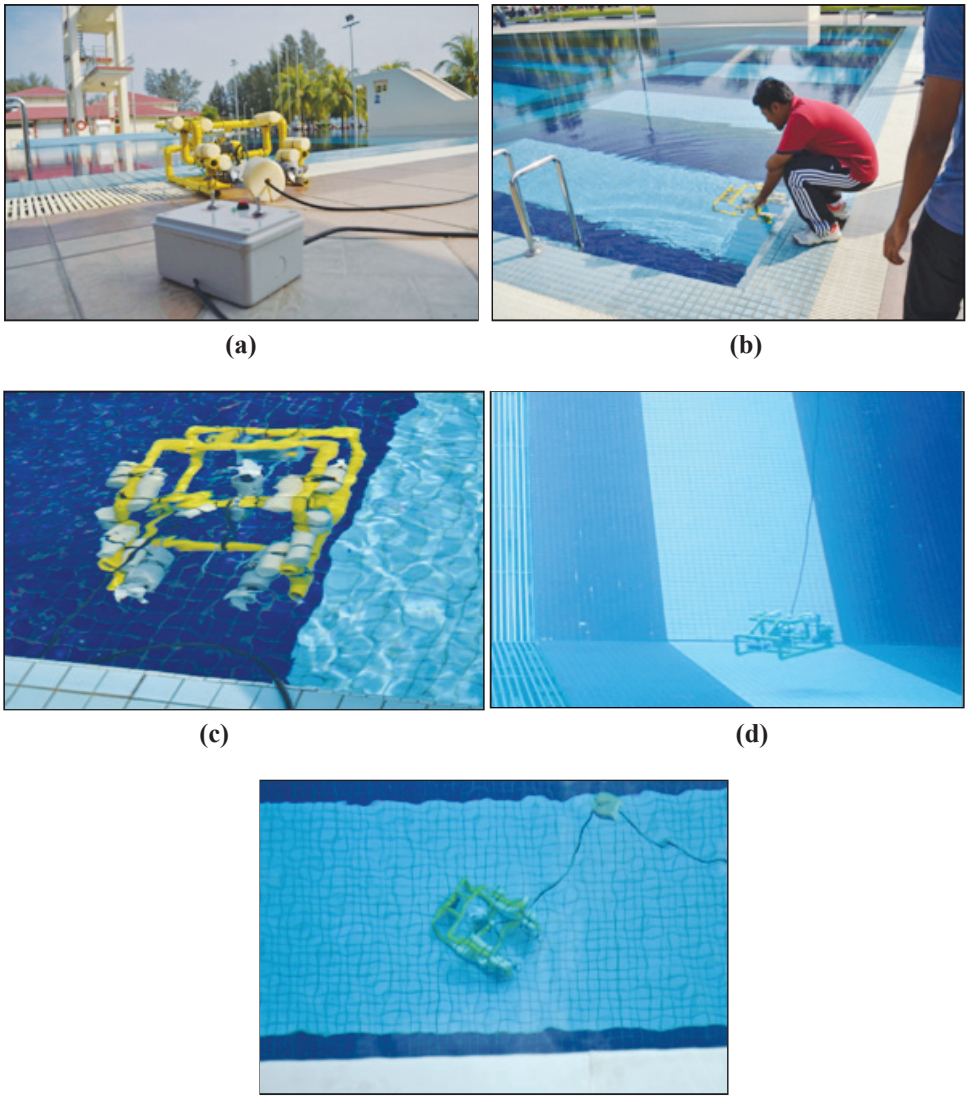

Figure 10: Field test of the mini ROV at KD Duyong: (a) The mini ROV ready to be deployed; (b) Deployment; (c) Mini ROV in idle position; (d) Side and (e)top views of the pool.

5. CONCLUSION

In this paper, the design, development and field test of the mini ROV have been described. The total cost of this project is less than RM 500. The active involvement of BTM's technical and support staff shows the great effort and determination in order to make this project a success. This is important to promote understanding and development of relevant technical skills, and to foster cooperation between research officers and technical staff. In addition, we managed to train five industrial

trainees from various universities in order to expose them to maritime technology activities. For future development of the mini ROV, we propose to add underwater cameras and lighting system, and to upgrade the current thrusters system.

REFERENCES

Abidin, Z., Arshad, M.R., Izman, K. & Kassim, M.H. (2011). TUISS: Towed Underwater Inspection and Survey System. *3rd International Conference on Underwater System Technology: Theory and Application 2010 (USYS'10)*, 1- 2 November 2010, Cyberjaya, Malaysia.

Ahmad, M.A. (2005). *The Development of a Simple Low Cost Underwater Vehicle*. Bachelor of Mechanical Engineering (Marine Technology) Degree Thesis, Universiti Teknologi Malaysia (UTM), Skudai, Johor.

Ali Hussain, N.A., Ting, M.N., Arshad, M.R. & Mokhtar, R.M. (2009). Modeling and system identification of underwater glider for shallow water applications. *School of Electrical & Electronics 2nd Postgraduate Cooloquium (EEPC 2009)*, November 2009, Bukit Jawi Resort, Penang.

Ali Hussain, N.A., Ibrahim, F., Nasuddin, N.M., Yaacob, R., Naim, H.M., Sulaiman, N.E.S., Ramli, R., Mohd Rashid, M.R., Ramle, I., Ismail, A.S., Louisnaden, E. & Ibrahim, N.A. (2011). Rekabentuk dan pembangunan sebuah kenderaan robotik bawah permukaan air (remotely operated vehicle). *Defence S&T Tech. Bull.,* **4**: 77-91.

Antonelli, G., Fossen, T.I. & Yoerger, D. (2008). Field and service robotics. Underwater Robotics. In Siciliano, B. & Khatib, O. (Eds.), *Springer Handbook of Robotics.* Springer-Verlag, Heidelberg, pp. 987-1008.

Arima, M., Ichihashi, N. & Miwa, Y. (2009). Modelling and motion simulation of an underwater glider with independently controllable main wings. *OCEANS 2009 IEEE Bremen: Balancing Technology with Future Needs,* 11-14 May 2009, pp. 1-6.

Brundage, H.M., Cooney, L., Huo, E., Licther, H., Oyebode, O., Sinha, P., Stanway, M.J., Stefanov-Wagner, T., Stiehl, K. & Walker, D. (2006). Design of an ROV to compete in the 5th Annual MATE ROV Competition and Beyond. *OCEANS 2006,* 18-21 September 2006, pp. 1-5.

Lobecker, R. & Nicholson, C. (2000). Application of new technologies to the MAX ROVER and Mini-MAX 2000 ROVs. *OCEANS 2000 MTS/IEEE Conference and Exhibition.*11-14 September 2000, pp. 157-161.

Muljowidodo, K., Nugroho, S.A. & Prayogo, N.C. (2010). Design, analysis, and testing composite gull of "SHRIMP" ROV. *3rd International Conference on Underwater System Technology: Theory and Application 2010 (USYS'10)*, 1- 2 November 2010, Cyberjaya, Malaysia.

Stepanek, M. & Conger, J.J. (2009). Techniques and tips: Get the most out of a mini-ROV. *OCEANS 2009, MTS/IEEE Biloxi - Marine Technology for Our Future: Global and Local Challenges,* 26-29 October 2009, pp. 1-7.

Yuh, J. (2000). Design and control of autonomous underwater robots: A survey. *Auton. Robot.,* **8**: 7-24.

Zain, Z. M., Ahmad, R.B. & Arshad, M.R. (2004). Design and development of an RS232-based ROV controller system. *IEEE Region 10 Annual International Conference, Proceedings/TENCON,* 24 November 2004, pp. 487-490.

THE EFFECT OF SMOOTHED SUNSPOT NUMBER (SSN) ON HF RADIO COMMUNICATIONS IN PENINSULAR MALAYSIA FOR THE YEARS 2009 TO 2011

Rafidah Abd Malik[1*], Dinesh Sathyamoorthy[1], Ab Sukor Zakariya[1], Aminudin Tompang[1], Halimah Tufail Mohamed[1], Mohd Rizal Ahmad Kamal[1], Abd Roni Rajab[2], Lim Say Lay[2], Hanizah Kasmoni[3], Norhayati Zahari[1], Jamilah Jaafar[1], Mohd Hafizi Che Mat[1], Hasniza Hambali[1], Zuraini Abd Manaf[3] & Muslihana Mustafa[2]

[1]Instrumentation & Electronics Technology Division (BTIE)
[2]Weapons Technology Division (BTP)
[3]Maritime Technology Division (BTM)
Science & Technology Research Institute for Defence (STRIDE), Ministry of Defence, Malaysia

*E-mail: rafidah.abdmalik@stride.gov.my

ABSTRACT

Sunspots, which are a natural phenomenon that occurs due to magnetic activity on the sun's surface, can be counted using smoothed sunspot number (SSN). Flares and prominences of SSNs radiate free ions in the ionosphere. This has significant effect on the stability of the ionosphere, resulting in the frequencies that can be used for high frequency (HF) communications to vary depending on time of day and season. In this study, the effect of SSN on HF radio communications in Peninsular Malaysia for the years 2009 to 2011 is evaluated. This study was carried out in a period where SSN values rise from low levels in 2009 to much higher levels in 2011, making it suitable to observe the effect of SSN values on HF frequencies employed. It is observed that as SSN values increase, the range of operating HF frequencies that can be used also increases. SSN values also have effect on frequencies that can be used for daily HF communications.

Keywords: *High frequency (HF) communications; ionosphere; sunspot; smoothed sunspot number (SSN); HF prediction.*

1. INTRODUCTION

The ionosphere refers to the regions of the upper atmosphere, where charges, either positive or negative, are present in quantities large enough to influence the trajectory of radio waves (Sizun, 2003; Atkins, 2008; Blaunstein & Plohotniuc, 2008; Nishida, 2010). There are a variety of operational communications systems

that are dependent upon the ionosphere, while there are others that are influenced by the ionosphere. Short-wave systems, such as medium frequency (MF) and high frequency (HF) systems, and long-wave systems, such as very low frequency (VLF) and low frequency (LF) systems, are dependent on the ionosphere. On the other hand, some very high frequency (VHF) systems, such as meteor-burst systems, and higher frequency Satellite Communications (SATCOM) systems in the ultra high frequency (UHF) and super high frequency (SHF) bands are influenced by the ionosphere (Goodman, 2003; Blaunstein & Plohotniuc, 2008; Nishida, 2010).

HF radio communications is dependent for most of its applications on the use of the ionosphere, which enables radio communications signals to be reflected and refracted back to the earth so that they can travel over great distances around the world, as shown in Figure 1. As radio communications signals can travel all over the world on HF bands, it is widely used in many areas, including broadcasting, military, maritime and amateur radio. Radio transmitters using relatively low power can be used to communicate to the other side of the world. Although radio propagation using the ionosphere may not be as reliable as that provided by satellites, it nevertheless provides a very cost effective and efficient form of radio communications. To enable the most to be made of ionospheric propagation, many radio users make extensive use of HF propagation programs to predict the areas of the world to which signals may travel or the probability of them reaching a given area (Dong & Li, 2007; Keller, 2010).

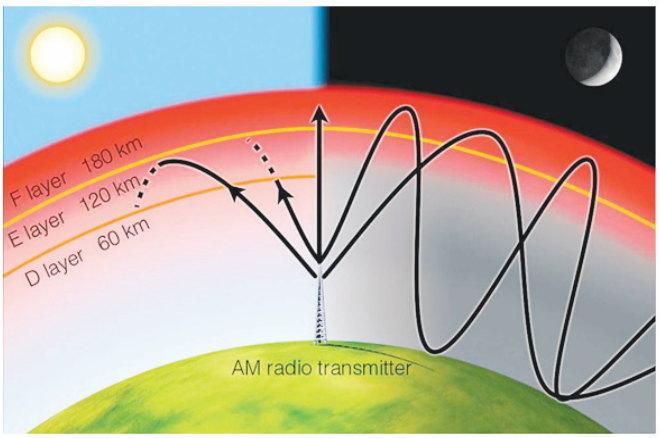

Figure 1: HF radio waves (Atkins, 2008).

However, the ionosphere is not a stable medium that allows the use of the same set of frequencies over the year, or even over 24 hours. Thus, a frequency which may provide successful communications at a particular time may not achieve it an hour later. Hence, users should determine the right frequencies to transmit HF signals (IPS, 1998; Keller, 2010). Based on that, most HF radio systems have

automatic link establishment (ALE) facilities to help the radios to locate better links or channels. ALE is the principle where a specialised radio modem, known as an ALE adaptive controller, is assigned the task of automatically controlling a HF receiver and transmitter in order to establish the highest quality communications link with one or multiple HF radio stations (Dong & Li, 2007; Keller, 2010).

Sunspots have significant effect on the stability of the ionosphere. In this study, the effect of smoothed sunspot number (SSN) on HF radio communications in Peninsular Malaysia for the years 2009 to 2011 is evaluated. Sunspots have an eleven-year activity cycle, with 2008 being the beginning of Solar Cycle 24. This study was carried out in a period where SSN values rise from low levels in 2009 to much higher levels in 2011, making it suitable to observe the effect of SSN values on HF frequencies employed.

2. SUNSPOTS

2.1 Generation of Sunspots

Ionisation of the ionosphere is caused by radiation from sunspots, which is one of the most notable phenomena on the surface of the sun. Sunspots are related to magnetic activity on the photosphere (Figure 2), which has magnetic fields of approximately 2,500 times the power of any on Earth. Sunspots appear in the form of roughly circular dark surfaces called umbras, surrounded by less dark regions known as penumbras. The maximum magnetic field is found in the middle of the umbra, as shown in Figure 3. The field lines at this point are usually directed away from the surface, but at the outer edge of the sunspot, the magnetic fields tend to bend over towards the edge. Sunspots are the most evident as well as the earliest demonstration of the existence of solar activity (IPS, 1998; Sizun, 2003; Atkins, 2008; Blaunstein & Plohotniuc, 2008; Bushby, 2008).

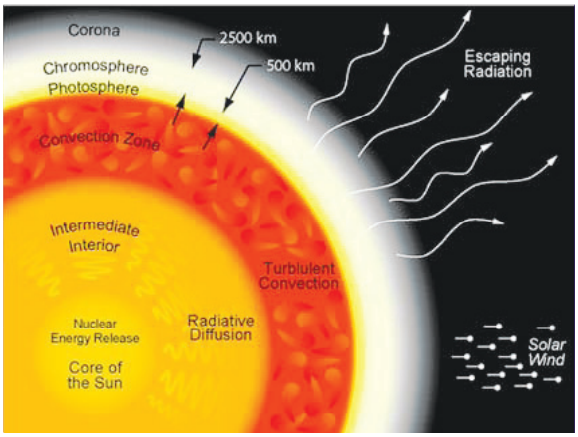

Figure 2: Internal make-up of the sun (ARRL, 2008).

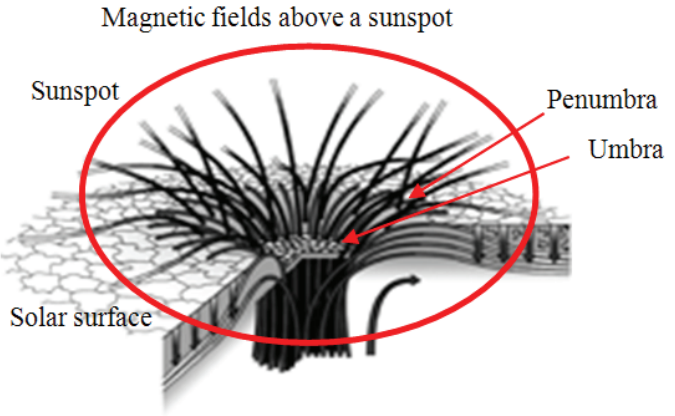

Figure 3: Schematic of the magnetic field structure within the umbra and penumbra of a typical sunspot. The magnetic field lines are predominantly vertical within the umbra. Within the penumbra, some of the field lines still have a significant vertical component, while those that are associated with the dark filaments are largely horizontal (Bushby, 2008).

Sunspots appear on the surface of the sun as dark and cooler areas. These spots may last a few days or they may be present for several months. They appear to be dark, because they have a lower temperature than the surrounding surface, typically around 3,000 K rather than 6,000 K for the rest of the surface (Sizun, 2003; ARRL, 2008). The dimensions of sunspots are extremely variable. Sunspots usually occur in groups of approximately ten, while other sunspots frequently exceed the diameter of the Earth (Atkins, 2008; Blaunstein & Plohotniuc, 2008).

2.2 Smoothed Sunspot Number (SSN)

Sunspots can be counted using SSN, which is calculated by counting the number of sunspot groups, followed by the number of individual spots. SSN is then given as the sum of the number of individual spots plus ten times the number of groups.

Space Weather Prediction Center (SWPC), National Oceanic and Atmospheric Administration (NOAA) computes the daily "Boulder Sunspot Number" using a formula devised by Rudolph Wolf in 1848 (Sizun, 2003; Blaunstein & Plohotniuc, 2008):

$$R=k\,(10g+s) \qquad (1)$$

where

R is the sunspot number;
g is the number of sunspot groups on the solar disk;
s is the total number of individual spots in all the groups;
k is a variable scaling factor (usually < 1) that accounts for observing conditions and the type of telescope (binoculars, space telescopes, etc.).

Sunspots have an eleven-year activity cycle that can be predicted (Figure 4). When sunspots are at their peak, the sun actually becomes brighter. This is because magnetically brighter areas surround each sunspot, more than making up for the dimmer areas. They last peaked in 2001, and had their last big dip in 1995 (Atkins, 2008; Blaunstein & Plohotniuc, 2008; NASA, 2011).

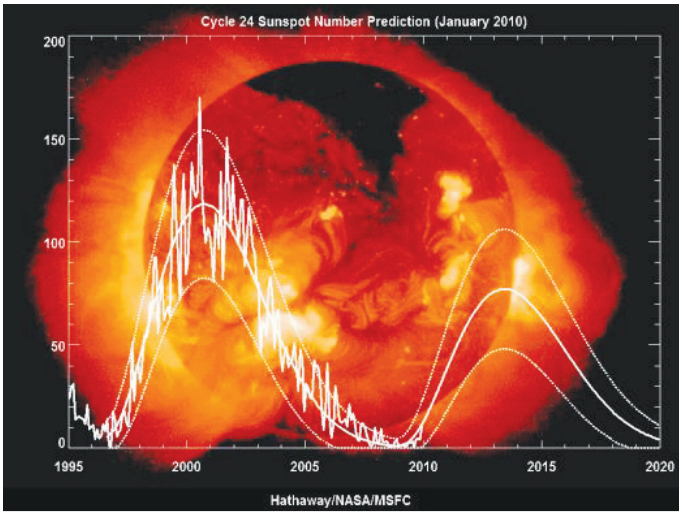

Figure 4: Prediction of SSN values (NASA, 2011).

During an active solar period, higher SSN values are produced, such as during the beginning of 2000. While higher SSN values allow better transmission between two points, SSN values that are too high will interfere with the transmission of HF signals (Dong & Li, 2007; Blaunstein & Plohotniuc, 2008; Keller, 2010). This happened on 8 August 2011 when the National Aeronautics and Space Administration (NASA) detected an eruption of strong solar flares, but the impact of these phenomena on communications and satellite systems was very small because the eruption was not facing the Earth (Figure 5). There were reports of HF radio interferences in Asia following the solar flare (NASA, 2011; Kosmo Online, 2011).

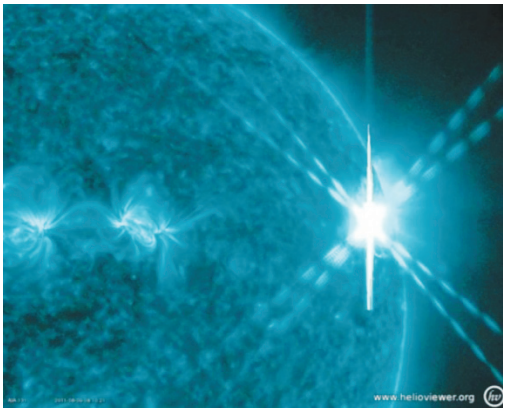

Figure 5: Still video image taken by NASA's Solar Dynamics Observatory showing the solar flare on 8 August 2011 as it appeared in the ultraviolet range of the light spectrum. The flare registered as an X6.9 class sun storm, the largest of Solar Cycle 24 (NASA, 2011).

3. METHODOLOGY

3.1 SSN Data

SSN data for the years 2009 to 2011, as shown in Figure 6, was obtained from Ionospheric Prediction Service (IPS) (2011). However, the SSN values for the period of August to December 2011 are predicted values. It is observed that the SSN values in 2009 were approaching zero, while the values in 2010 increased by more than 10 units. For 2011, the SSN values increased every month, except in June, where the values fell by 37 units. Observatory stations all over the world have predicted that the SSN values will increase until the solar maximum in 2013, after which they will gradually fall, as shown in Figure 4 (NASA, 2011).

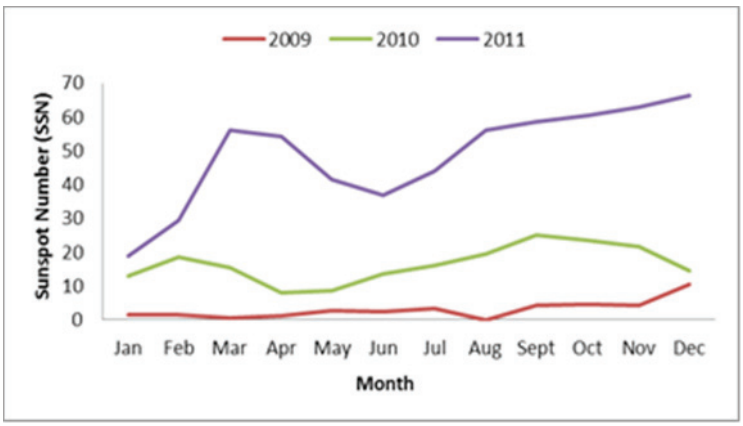

Figure 6: SSN values for the years 2009 to 2011.

3.2 HF Frequencies Prediction

By knowing the SSN values, the Maximum Usable Frequency (MUF) can be predicted or expected. MUF is the highest possible frequency that can be used to transmit over a particular path under given ionospheric conditions (Harris, 1996; Freeman, 2007; ARRL, 2008). MUF is important for determining the best HF frequency to use in communicating between two locations as shown in Figure 7. Prediction of HF frequencies using prediction software, such as the Advanced Stand Alone Prediction System−(ASAPS), shows the approximate range of frequencies that can be transmitted. All prediction software take SSN values as an input parameter, in addition to time of day, month, longitude and latitude of the transmitter and receiver stations, and type of antenna (Freeman, 2007; Dong & Li, 2007; Keller, 2010).

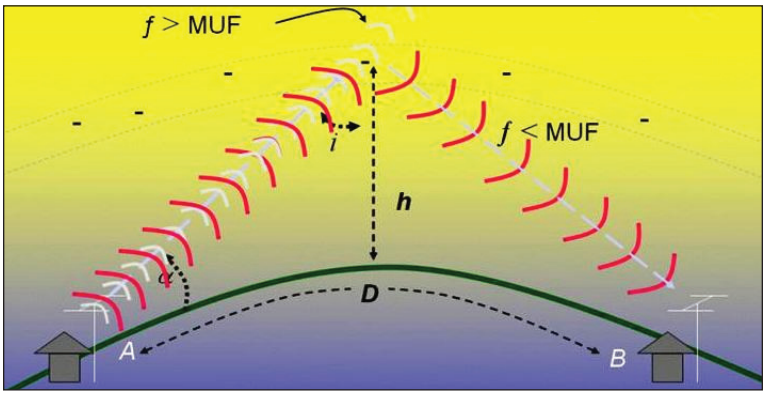

Figure 7: MUF between two points (Delta DX, 2007).

The ASAPS uses the T-index which is also called as "equivalent sunspot number". The T-index is an indicator of the highest frequencies able to be refracted from regions in the ionosphere. The higher the T- index, the higher the frequencies able to be refracted from an ionospheric region. The index is based on the measurement of ionospheric *fo*F2 values, which indicate the strength of the ionosphere in terms of transmitted frequency penetration, obtained from ionograms. Following geomagnetic activity, the typical ionospheric response at mid-latitudes is to become depressed, which will result in a drop in the value of the T-index produced from ionospheric stations within the depressed ionospheric region. The T-index is also forecasted by IPS and is used in the prediction of point-to-point frequencies in HF communications (IPS, 1998).

The GRAFEX frequency predictions in Figure 8, computed using the ASAPS shows that in 2009, only HF frequencies in the lower range can be used for communications due to the low T-index values. In 2010 (Figure 9), the frequency range increased slightly but still does not have a big impact. The T-index value

increased from 12 in January 2010 to 22 in December 2010. For the years 2009 to 2010, the HF frequencies that can be used are between 3.0 to 7.5 MHz. However, in 2011 (Figure 10), as the T-index values increase significantly, the frequency range also increases, with the highest frequency range being up to 8.5 MHz.

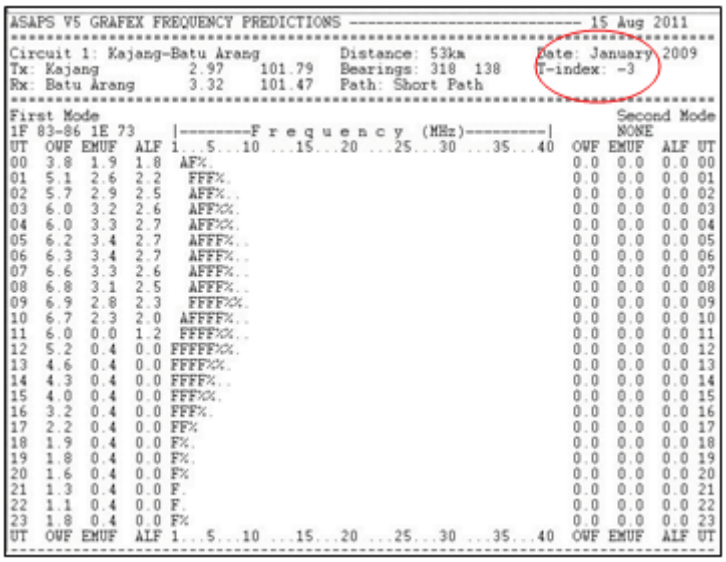

```
ASAPS V5 GRAFEX FREQUENCY PREDICTIONS ---------- 15 Aug 2011
Circuit 1: Kajang-Batu Arang          Distance: 53km      Date: January 2009
Tx: Kajang          2.97   101.79     Bearings: 318  138  T-index: -3
Rx: Batu Arang      3.32   101.47     Path: Short Path
First Mode                                                Second Mode
1F 83-86 1E 73    |--------F r e q u e n c y  (MHz)---------|   NONE
UT  OWF EMUF  ALF 1...5...10 ...15...20 ...25...30 ...35...40  OWF EMUF  ALF UT
00  3.8  1.9  1.8  AF%.                                       0.0  0.0  0.0 00
01  5.1  2.6  2.2   FFF%.                                     0.0  0.0  0.0 01
02  5.7  2.9  2.5   AFF%..                                    0.0  0.0  0.0 02
03  6.0  3.2  2.6   AFF%%.                                    0.0  0.0  0.0 03
04  6.0  3.3  2.7   AFF%%.                                    0.0  0.0  0.0 04
05  6.2  3.4  2.7   AFFF%..                                   0.0  0.0  0.0 05
06  6.3  3.4  2.7   AFFF%..                                   0.0  0.0  0.0 06
07  6.6  3.3  2.6   AFFF%..                                   0.0  0.0  0.0 07
08  6.8  3.1  2.5   AFFF%..                                   0.0  0.0  0.0 08
09  6.9  2.8  2.3   FFFF%%.                                   0.0  0.0  0.0 09
10  6.7  2.3  2.0  AFFFF%..                                   0.0  0.0  0.0 10
11  6.0  0.0  1.2  FFFF%%..                                   0.0  0.0  0.0 11
12  5.2  0.4  0.0 FFFFF%%.                                    0.0  0.0  0.0 12
13  4.6  0.4  0.0 FFFF%%.                                     0.0  0.0  0.0 13
14  4.3  0.4  0.0 FFFF%..                                     0.0  0.0  0.0 14
15  4.0  0.4  0.0 FFF%%.                                      0.0  0.0  0.0 15
16  3.2  0.4  0.0 FFF%.                                       0.0  0.0  0.0 16
17  2.2  0.4  0.0 FF%                                         0.0  0.0  0.0 17
18  1.9  0.4  0.0 F%.                                         0.0  0.0  0.0 18
19  1.8  0.4  0.0 F%.                                         0.0  0.0  0.0 19
20  1.6  0.4  0.0 F%                                          0.0  0.0  0.0 20
21  1.3  0.4  0.0 F.                                          0.0  0.0  0.0 21
22  1.1  0.4  0.0 F.                                          0.0  0.0  0.0 22
23  1.8  0.4  0.0 F%                                          0.0  0.0  0.0 23
UT  OWF EMUF  ALF 1...5...10 ...15...20 ...25...30 ...35...40  OWF EMUF  ALF UT
```

(a)

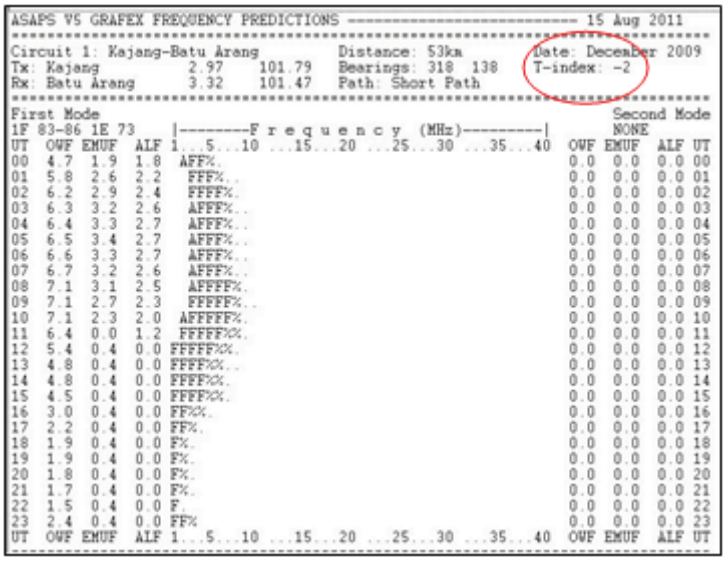

```
ASAPS V5 GRAFEX FREQUENCY PREDICTIONS ---------- 15 Aug 2011
Circuit 1: Kajang-Batu Arang          Distance: 53km      Date: December 2009
Tx: Kajang          2.97   101.79     Bearings: 318  138  T-index: -2
Rx: Batu Arang      3.32   101.47     Path: Short Path
First Mode                                                Second Mode
1F 83-86 1E 73    |--------F r e q u e n c y  (MHz)---------|   NONE
UT  OWF EMUF  ALF 1...5...10 ...15...20 ...25...30 ...35...40  OWF EMUF  ALF UT
00  4.7  1.9  1.8  AFF%.                                      0.0  0.0  0.0 00
01  5.8  2.6  2.2   FFF%..                                    0.0  0.0  0.0 01
02  6.2  2.9  2.4   FFFF%.                                    0.0  0.0  0.0 02
03  6.3  3.2  2.6   AFFF%..                                   0.0  0.0  0.0 03
04  6.4  3.3  2.7   AFFF%..                                   0.0  0.0  0.0 04
05  6.5  3.4  2.7   AFFF%..                                   0.0  0.0  0.0 05
06  6.6  3.3  2.7   AFFF%..                                   0.0  0.0  0.0 06
07  6.7  3.2  2.6   AFFF%..                                   0.0  0.0  0.0 07
08  7.1  3.1  2.5   AFFFF%.                                   0.0  0.0  0.0 08
09  7.1  2.7  2.3   FFFFF%..                                  0.0  0.0  0.0 09
10  7.1  2.3  2.0  AFFFFF%.                                   0.0  0.0  0.0 10
11  6.4  0.0  1.2  FFFFF%%.                                   0.0  0.0  0.0 11
12  5.4  0.4  0.0 FFFFF%%.                                    0.0  0.0  0.0 12
13  4.8  0.4  0.0 FFFF%%..                                    0.0  0.0  0.0 13
14  4.8  0.4  0.0 FFFF%%.                                     0.0  0.0  0.0 14
15  4.5  0.4  0.0 FFFF%%.                                     0.0  0.0  0.0 15
16  3.0  0.4  0.0 FF%%.                                       0.0  0.0  0.0 16
17  2.2  0.4  0.0 FF%.                                        0.0  0.0  0.0 17
18  1.9  0.4  0.0 F%.                                         0.0  0.0  0.0 18
19  1.9  0.4  0.0 F%.                                         0.0  0.0  0.0 19
20  1.8  0.4  0.0 F%.                                         0.0  0.0  0.0 20
21  1.7  0.4  0.0 F%.                                         0.0  0.0  0.0 21
22  1.5  0.4  0.0 F.                                          0.0  0.0  0.0 22
23  2.4  0.4  0.0 FF%                                         0.0  0.0  0.0 23
UT  OWF EMUF  ALF 1...5...10 ...15...20 ...25...30 ...35...40  OWF EMUF  ALF UT
```

(b)

Figure 8: GRAFEX frequency predictions for: (a) January and (b) December 2009.

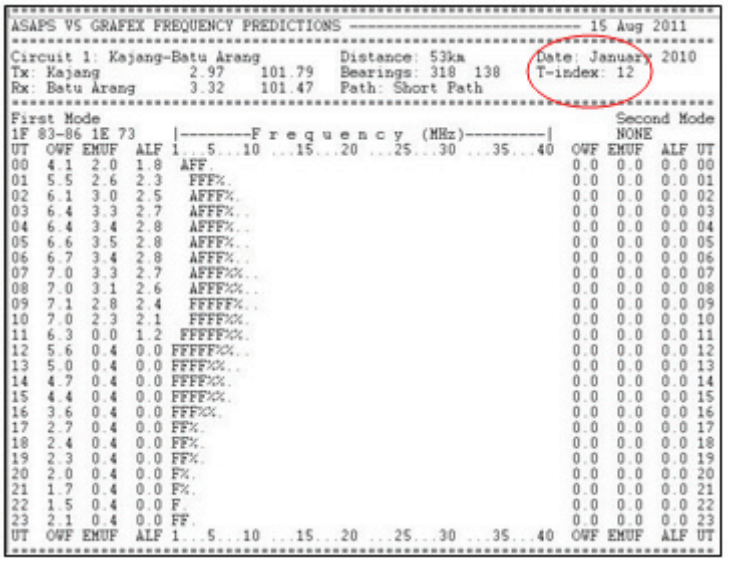

```
ASAPS V5 GRAFEX FREQUENCY PREDICTIONS ---------- 15 Aug 2011

Circuit 1: Kajang-Batu Arang          Distance: 53km      Date: January 2010
Tx: Kajang          2.97    101.79    Bearings: 318  138  T-index: 12
Rx: Batu Arang      3.32    101.47    Path: Short Path

First Mode                                                    Second Mode
1F 83-86 1E 73    |--------F r e q u e n c y  (MHz)---------|      NONE
UT  OWF EMUF  ALF 1...5...10 ...15...20 ...25...30 ...35...40  OWF EMUF  ALF UT
00  4.1  2.0  1.8  AFF.                                       0.0  0.0  0.0 00
01  5.5  2.6  2.3   FFF%.                                     0.0  0.0  0.0 01
02  6.1  3.0  2.5   AFFF%.                                    0.0  0.0  0.0 02
03  6.4  3.3  2.7   AFFF%..                                   0.0  0.0  0.0 03
04  6.4  3.4  2.8   AFFF%..                                   0.0  0.0  0.0 04
05  6.6  3.5  2.8   AFFF%..                                   0.0  0.0  0.0 05
06  6.7  3.4  2.8   AFFF%..                                   0.0  0.0  0.0 06
07  7.0  3.3  2.7   AFFF%%..                                  0.0  0.0  0.0 07
08  7.0  3.1  2.6   AFFF%%..                                  0.0  0.0  0.0 08
09  7.1  2.8  2.4   FFFFF%..                                  0.0  0.0  0.0 09
10  7.0  2.3  2.1   FFFFF%..                                  0.0  0.0  0.0 10
11  6.3  0.0  1.2  FFFFF%%..                                  0.0  0.0  0.0 11
12  5.6  0.4  0.0 FFFFF%%..                                   0.0  0.0  0.0 12
13  5.0  0.4  0.0 FFFF%%..                                    0.0  0.0  0.0 13
14  4.7  0.4  0.0 FFFF%%.                                     0.0  0.0  0.0 14
15  4.4  0.4  0.0 FFFF%%.                                     0.0  0.0  0.0 15
16  3.6  0.4  0.0 FFF%%.                                      0.0  0.0  0.0 16
17  2.7  0.4  0.0 FF%.                                        0.0  0.0  0.0 17
18  2.4  0.4  0.0 FF%.                                        0.0  0.0  0.0 18
19  2.3  0.4  0.0 FF%.                                        0.0  0.0  0.0 19
20  2.0  0.4  0.0 F%.                                         0.0  0.0  0.0 20
21  1.7  0.4  0.0 F%.                                         0.0  0.0  0.0 21
22  1.5  0.4  0.0 F.                                          0.0  0.0  0.0 22
23  2.1  0.4  0.0 FF.                                         0.0  0.0  0.0 23
UT  OWF EMUF  ALF 1...5...10 ...15...20 ...25...30 ...35...40  OWF EMUF  ALF UT
```

(a)

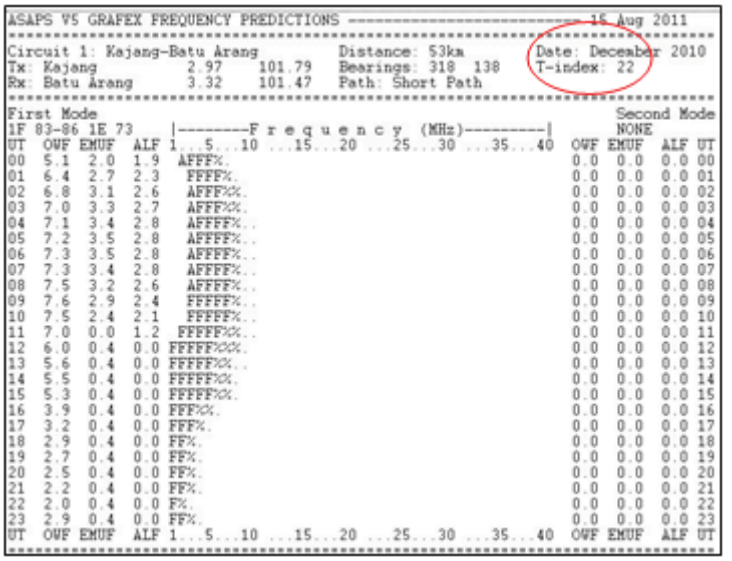

```
ASAPS V5 GRAFEX FREQUENCY PREDICTIONS ---------- 15 Aug 2011

Circuit 1: Kajang-Batu Arang          Distance: 53km      Date: December 2010
Tx: Kajang          2.97    101.79    Bearings: 318  138  T-index: 22
Rx: Batu Arang      3.32    101.47    Path: Short Path

First Mode                                                    Second Mode
1F 83-86 1E 73    |--------F r e q u e n c y  (MHz)---------|      NONE
UT  OWF EMUF  ALF 1...5...10 ...15...20 ...25...30 ...35...40  OWF EMUF  ALF UT
00  5.1  2.0  1.9  AFFF%.                                     0.0  0.0  0.0 00
01  6.4  2.7  2.3   FFFF%.                                    0.0  0.0  0.0 01
02  6.8  3.1  2.6   AFFF%%.                                   0.0  0.0  0.0 02
03  7.0  3.3  2.7   AFFF%%.                                   0.0  0.0  0.0 03
04  7.1  3.4  2.8   AFFFF%..                                  0.0  0.0  0.0 04
05  7.2  3.5  2.8   AFFFF%..                                  0.0  0.0  0.0 05
06  7.3  3.5  2.8   AFFFF%..                                  0.0  0.0  0.0 06
07  7.3  3.4  2.8   AFFFF%..                                  0.0  0.0  0.0 07
08  7.5  3.2  2.6   AFFFF%..                                  0.0  0.0  0.0 08
09  7.6  2.9  2.4   FFFFF%..                                  0.0  0.0  0.0 09
10  7.5  2.4  2.1   FFFFF%..                                  0.0  0.0  0.0 10
11  7.0  0.0  1.2  FFFFF%%..                                  0.0  0.0  0.0 11
12  6.0  0.4  0.0 FFFFF%%%.                                   0.0  0.0  0.0 12
13  5.6  0.4  0.0 FFFFF%%..                                   0.0  0.0  0.0 13
14  5.5  0.4  0.0 FFFFF%%.                                    0.0  0.0  0.0 14
15  5.3  0.4  0.0 FFFFF%%.                                    0.0  0.0  0.0 15
16  3.9  0.4  0.0 FFF%%.                                      0.0  0.0  0.0 16
17  3.2  0.4  0.0 FFF%.                                       0.0  0.0  0.0 17
18  2.9  0.4  0.0 FF%.                                        0.0  0.0  0.0 18
19  2.7  0.4  0.0 FF%.                                        0.0  0.0  0.0 19
20  2.5  0.4  0.0 FF%.                                        0.0  0.0  0.0 20
21  2.2  0.4  0.0 FF%.                                        0.0  0.0  0.0 21
22  2.0  0.4  0.0 F%.                                         0.0  0.0  0.0 22
23  2.9  0.4  0.0 FF%.                                        0.0  0.0  0.0 23
UT  OWF EMUF  ALF 1...5...10 ...15...20 ...25...30 ...35...40  OWF EMUF  ALF UT
```

(b)

Figure 9: GRAFEX frequency predictions for: (a) January and (b) December 2010.

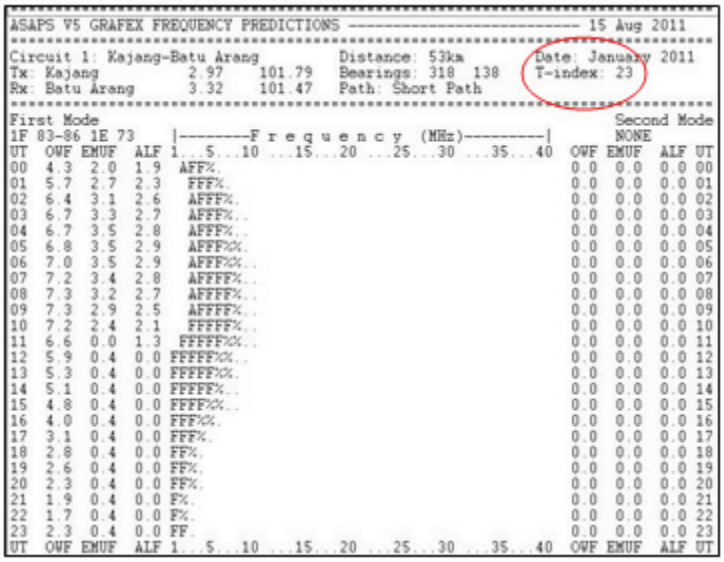

ASAPS V5 GRAFEX FREQUENCY PREDICTIONS ---------- 15 Aug 2011

Circuit 1: Kajang-Batu Arang — Distance: 53km — Date: January 2011
Tx: Kajang 2.97 101.79 — Bearings: 318 138 — T-index: 23
Rx: Batu Arang 3.32 101.47 — Path: Short Path

First Mode — 1F 83-86 1E 73 — Second Mode: NONE

UT	OWF	EMUF	ALF	1...5...10...15...20...25...30...35...40	OWF	EMUF	ALF	UT
00	4.3	2.0	1.9	AFF%.	0.0	0.0	0.0	00
01	5.7	2.7	2.3	FFF%.	0.0	0.0	0.0	01
02	6.4	3.1	2.6	AFFF%.	0.0	0.0	0.0	02
03	6.7	3.3	2.7	AFFF%..	0.0	0.0	0.0	03
04	6.7	3.5	2.8	AFFF%..	0.0	0.0	0.0	04
05	6.8	3.5	2.9	AFFF%%.	0.0	0.0	0.0	05
06	7.0	3.5	2.9	AFFF%%..	0.0	0.0	0.0	06
07	7.2	3.4	2.8	AFFFF%..	0.0	0.0	0.0	07
08	7.3	3.2	2.7	AFFFF%..	0.0	0.0	0.0	08
09	7.3	2.9	2.5	AFFFF%..	0.0	0.0	0.0	09
10	7.2	2.4	2.1	FFFFF%..	0.0	0.0	0.0	10
11	6.6	0.0	1.3	FFFFF%%..	0.0	0.0	0.0	11
12	5.9	0.4	0.0	FFFFF%%..	0.0	0.0	0.0	12
13	5.3	0.4	0.0	FFFFF%%.	0.0	0.0	0.0	13
14	5.1	0.4	0.0	FFFFF%..	0.0	0.0	0.0	14
15	4.8	0.4	0.0	FFFF%%..	0.0	0.0	0.0	15
16	4.0	0.4	0.0	FFF%%.	0.0	0.0	0.0	16
17	3.1	0.4	0.0	FFF%.	0.0	0.0	0.0	17
18	2.8	0.4	0.0	FF%.	0.0	0.0	0.0	18
19	2.6	0.4	0.0	FF%.	0.0	0.0	0.0	19
20	2.3	0.4	0.0	FF%.	0.0	0.0	0.0	20
21	1.9	0.4	0.0	F%.	0.0	0.0	0.0	21
22	1.7	0.4	0.0	F%.	0.0	0.0	0.0	22
23	2.3	0.4	0.0	FF.	0.0	0.0	0.0	23
UT	OWF	EMUF	ALF	1...5...10...15...20...25...30...35...40	OWF	EMUF	ALF	UT

(a)

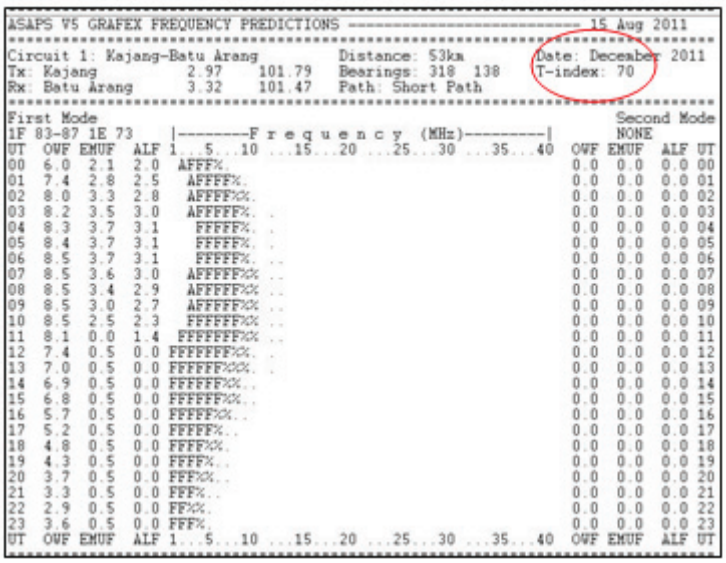

ASAPS V5 GRAFEX FREQUENCY PREDICTIONS ---------- 15 Aug 2011

Circuit 1: Kajang-Batu Arang — Distance: 53km — Date: December 2011
Tx: Kajang 2.97 101.79 — Bearings: 318 138 — T-index: 70
Rx: Batu Arang 3.32 101.47 — Path: Short Path

First Mode — 1F 83-87 1E 73 — Second Mode: NONE

UT	OWF	EMUF	ALF	1...5...10...15...20...25...30...35...40	OWF	EMUF	ALF	UT
00	6.0	2.1	2.0	AFFF%.	0.0	0.0	0.0	00
01	7.4	2.8	2.5	AFFFF%.	0.0	0.0	0.0	01
02	8.0	3.3	2.8	AFFFF%%.	0.0	0.0	0.0	02
03	8.2	3.5	3.0	AFFFFF%..	0.0	0.0	0.0	03
04	8.3	3.7	3.1	FFFFF%..	0.0	0.0	0.0	04
05	8.4	3.7	3.1	FFFFF%..	0.0	0.0	0.0	05
06	8.5	3.7	3.1	FFFFF%...	0.0	0.0	0.0	06
07	8.5	3.6	3.0	AFFFFF%%..	0.0	0.0	0.0	07
08	8.5	3.4	2.9	AFFFFF%%..	0.0	0.0	0.0	08
09	8.5	3.0	2.7	AFFFFF%%..	0.0	0.0	0.0	09
10	8.5	2.5	2.3	FFFFFF%%..	0.0	0.0	0.0	10
11	8.1	0.0	1.4	FFFFFFF%%..	0.0	0.0	0.0	11
12	7.4	0.5	0.0	FFFFFFF%%..	0.0	0.0	0.0	12
13	7.0	0.5	0.0	FFFFFF%%%..	0.0	0.0	0.0	13
14	6.9	0.5	0.0	FFFFFF%%..	0.0	0.0	0.0	14
15	6.8	0.5	0.0	FFFFFF%%..	0.0	0.0	0.0	15
16	5.7	0.5	0.0	FFFFF%%..	0.0	0.0	0.0	16
17	5.2	0.5	0.0	FFFFF%..	0.0	0.0	0.0	17
18	4.8	0.5	0.0	FFFF%%.	0.0	0.0	0.0	18
19	4.3	0.5	0.0	FFFF%..	0.0	0.0	0.0	19
20	3.7	0.5	0.0	FFF%%..	0.0	0.0	0.0	20
21	3.3	0.5	0.0	FFF%..	0.0	0.0	0.0	21
22	2.9	0.5	0.0	FF%%.	0.0	0.0	0.0	22
23	3.6	0.5	0.0	FFF%.	0.0	0.0	0.0	23
UT	OWF	EMUF	ALF	1...5...10...15...20...25...30...35...40	OWF	EMUF	ALF	UT

(b)

Figure 10: GRAFEX frequency predictions for: (a) January and (b) December 2011.

3.3 Transmission of HF Frequencies

A few predicted HF frequencies (MUF) were selected for transmission tests which were conducted between the STRIDE laboratories in Kajang, Batu Arang and Lumut (Figure 11). The Telefunken HF radio communications system (Figure 12), which complies with key radio communications standards, including MIL-STD-810 and MIL-STD-188-141B ALE (Telefunken, 2006), was used as the transceiver system for the transmission tests, which were conducted between April 2009 to September 2011.

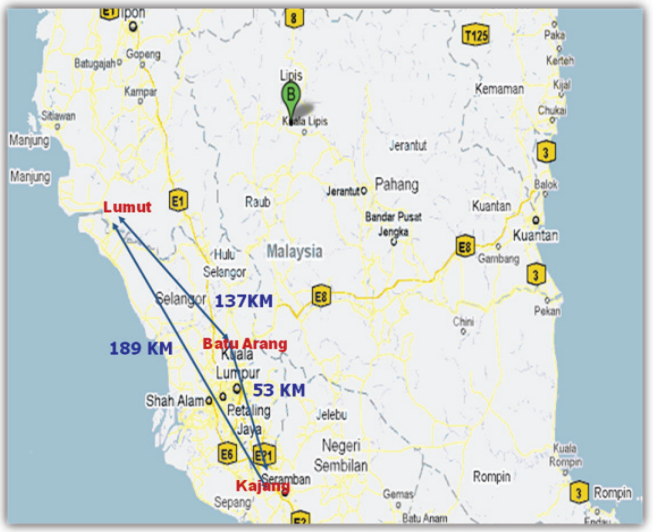

Figure 11: The three base stations chosen for the tests.

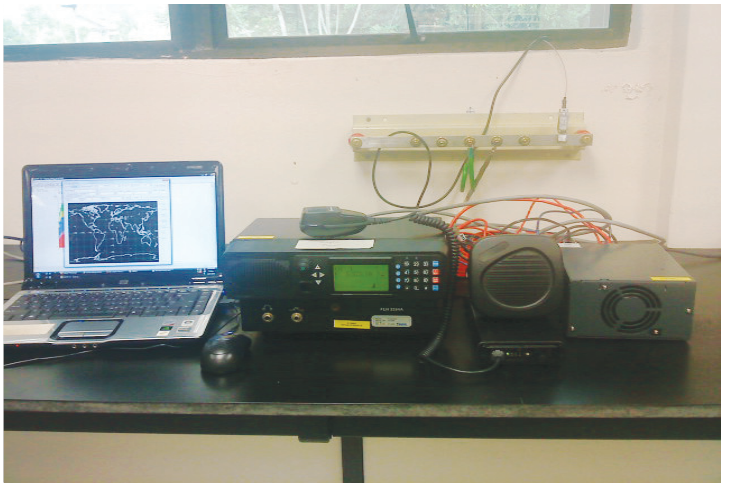

Figure 12: The Telefunken HF radio communications system used in the tests.

4. RESULTS AND ANALYSIS

The frequencies used for the tests are shown in Figures 13 to 16, where the red dots represent frequencies that have achieved successful communication at the time of the tests. When the HF signals are transmitted, some of these frequencies can be utilised for transmission while others cannot be used. This is due to changes in ionosphere ionisation, which depends on radiation from sunspots. The ionised atmosphere allows the radiated wave to travel faster through it. The lower the frequency of the wave, the less penetration effect it has, with the greater the proportion of it being turned back toward earth (Harris, 1996; Zain, 2000; Freeman, 2007).

In the test conducted in July 2009 (Figure 13), 45 HF frequencies were used for transmission, but only 20% of the frequencies achieved successful communication. The very low SSN values in 2009 resulted in low operating HF frequency range. In 2010, the SSN values slightly increased, enabling more frequencies through the ionosphere. The test conducted in February 2010 (Figure 14) indicates that 53% of the 45 HF frequencies used achieved successful transmission. For the test conducted in September 2011 (Figure 15), 60% of the 75 HF frequencies used achieved successful communication. This is because in 2011, the SSN values have largely increased, resulting in more penetrating energy into the ionosphere.

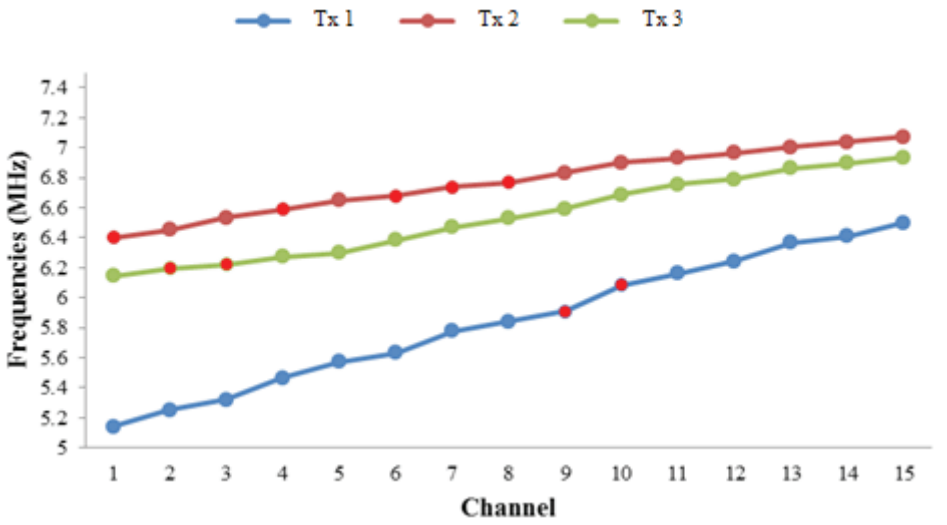

Figure 13: Frequencies used for tests conducted in July 2009 between Lumut and Batu Arang.

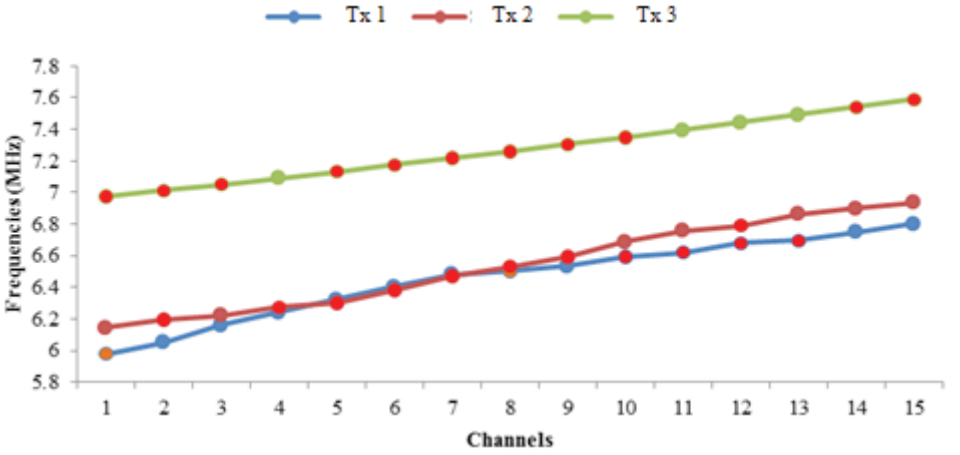

Figure 14: Frequencies used for tests conducted in February 2010 between Kajang and Batu Arang.

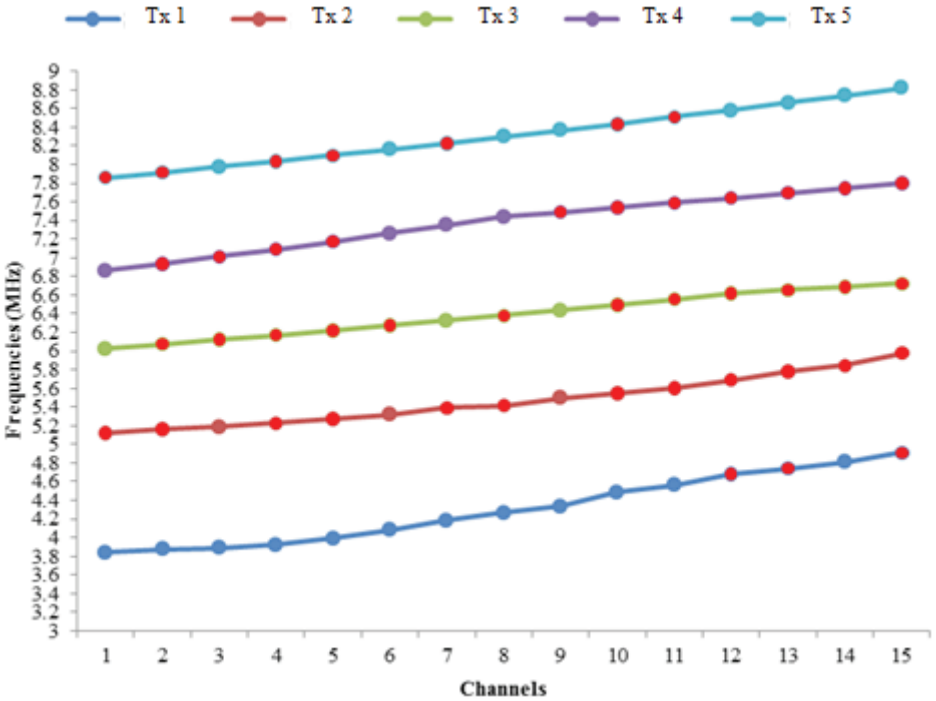

Figure 15: Frequencies used for tests conducted in September 2011 between Kajang and Lumut.

Figure 16 shows the frequencies employed for tests conducted between Kajang and Lumut for three consecutive days (24 to 26 March 2010). The three tests used the same frequencies, with it being observed that certain frequencies could be used on a certain day, but not for other days. There were also frequencies that could be used for all three days. The frequencies that cannot be used at the time of the tests could still be used during other periods depending on the time of day, the angle at which the wave strikes the ionosphere, and the degree of ionisation present (Zain, 2000; Freeman, 2007).

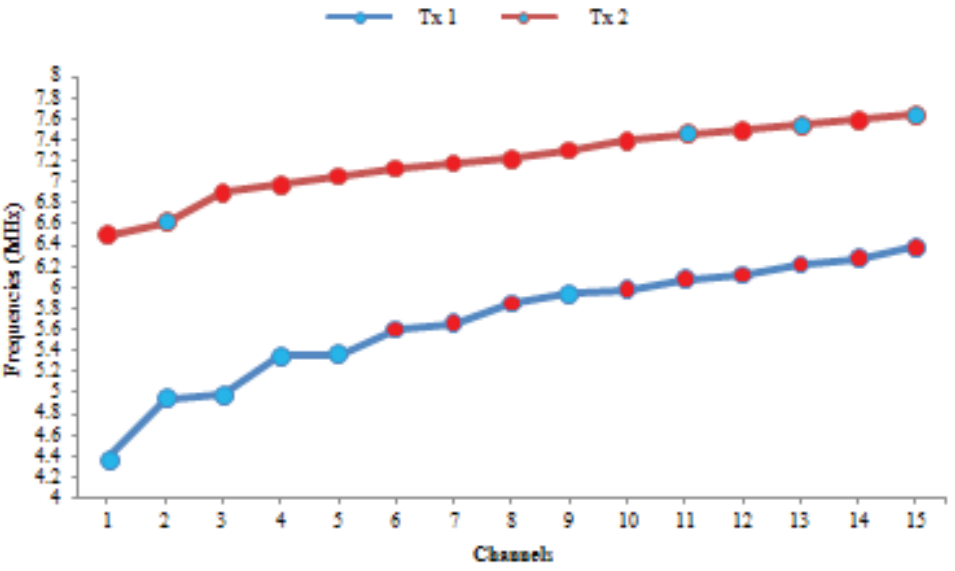
Tx 1
Tx 2
Frequencies (MHz)
Channels

(a)

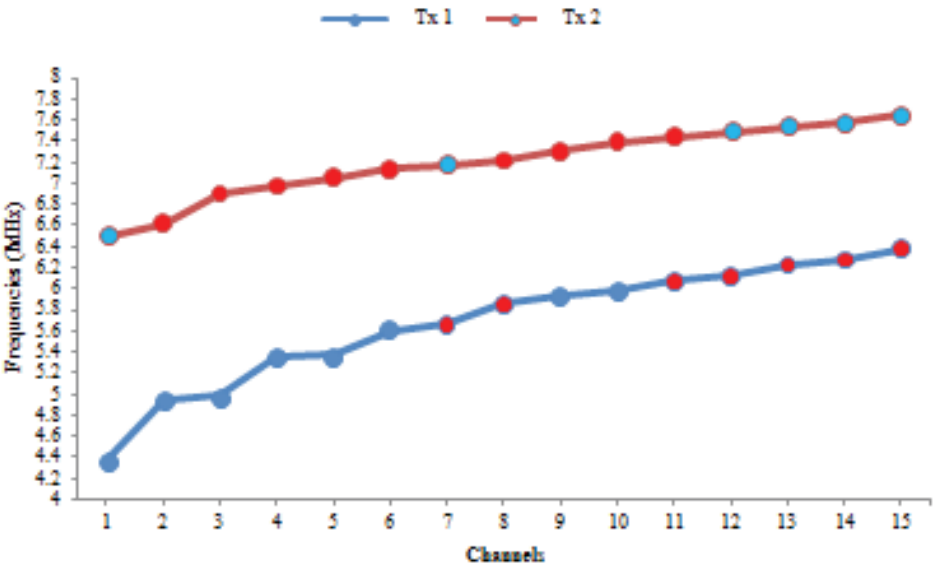
Tx 1
Tx 2
Frequencies (MHz)
Channels

(b)

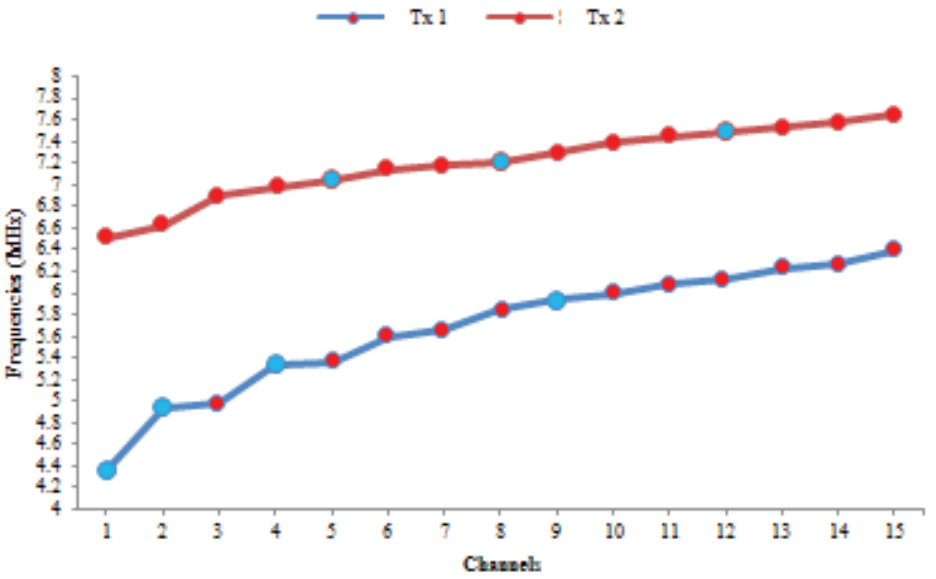

(c)

Figure 16: Frequencies used for test conducted on three consecutive days in 2010 between Kajang and Lumut: (a) 24; (b) 25; and (c) 26 March 2010.

The results of the test conducted on 24 March (Figure 16(a)) indicate that 73% of frequencies could be used. On the second day (Figure 16(b)), only 50% of frequencies could be used, while 77% of frequencies could be used on the third day (Figure 16(c)). The HF frequencies that could be used for transmissions during the test were constantly changing according to changes of ions in the ionosphere, which are ionised by flares and prominences resulting from SSNs. According to Zain (2000), HF signals can penetrate ions with weak ionisation, while with stronger ionisation, the signals may be refracted. With even stronger ionisation, the wave energy may be totally absorbed and dissipated in the ionosphere.

Wireless communications, especially HF communications systems, largely depend on space weather and the associated ionospheric conditions. Solar–terrestrial hazards such as particle radiation, solar flares and magnetic storms modify the electron-density profile in the ionosphere, resulting in disturbed conditions for radio-communications systems. The effected ionosphere modifies the transmission properties of this medium (Stanislawska *et al*., 2005; Blaunstein & Plohotniuc, 2008; Nishida, 2010). Therefore, the operating HF frequency range is dependent on SSN, as shown in Table 1. These results not only can be used for the period of 2009 to 2011, but can also be used as a reference for future predictions.

Table 1: Determined operating HF frequency ranges for the years 2009-2011.

Year	SSN	Frequency (MHz)
2009	0 - 11	3 – 7.1
2010	7 - 26	3 – 7.5
2011	19 - 70	3 – 8.5

5. CONCLUSION

Based on the transmission tests that have been conducted, it is observed that SSN has large impact on HF communications systems. Apart from SSN, there are other factors that influence the transmission of HF signals, including selection of antenna, elevation angle, critical frequency and link budget. However, these factors can be controlled and minimised, while SSN is a natural factor that cannot be controlled but can be predicted.

ACKNOWLEDGEMENT

This study was conducted as part of the Ninth Malaysia Plan (RMK9) project entitled *Study on Behaviour of Operating High Frequency (HF) Radio Frequencies for the Malaysian Armed Forces (MAF)*. The authors would like to thank the Science & Technology Research Institute for Defence (STRIDE) for providing research facilities and technical assistance during the experimental works.

REFERENCES

American Radio Relay League (ARRL) (2008). *The Sun and Sunspots*. American Radio Relay League (ARRL). Newington, Connecticut.

Atkins, N. (2008). *Survey of Meteorology*. Lyndon State College, Lyndon, Vermont.

Blaunstein, N. & Plohotniuc, E. (2008). *Ionosphere and Applied Aspects of Radio Communication and Radar*. CRC Press, Boca Raton Florida.

Bushby, P.J. (2008). Magnetic fields in the solar photosphere. *Phil. Trans. R. Soc. A,* **366**: 4465-4476.

Delta DX Association (2007). *HF Propagation*. Available online at:
http://www.deltadx.net/ABCDx/Sections/Propagation.htm (Last access date: 15 September 2011).

Dong, B.H. & Li, S.Q. (2007). Current status and developing tendency for high frequency communications. *Inform. Electron. Eng.*, **7**: 2007-01-000

Freeman, R. L. (2007). *Radio System Design for Telecommunications*. Wiley-Interscience, New Jersey.

Goodman, J. M. (2003). Operational communication systems and relationships to the ionosphere and space weather. *Adv. Space Res.*, **36**: 2241-2252.

Harris Corporation (1996). *Radio Communications in the Digital Age, Volume One: HF Technology*. Harris Corporation, Melbourne, Florida.

IPS Radio and Space Services (1998). *Introduction to HF Radio Propagation*. IPS Radio and Space Services, Surry Hills, New South Wales, Australia.

IPS Radio and Space Services (2011). *IPS Radio and Space Services*. Available online at: http://www.ips.gov.au (Last access date: 10 October 2011).

Keller, J. (2010). Military HF radio communications may prove effective for Internet relay chat in land, sea, and air applications. *Mil. Aerosp. Electron.*, **21**: 9.

Kosmo Online (2011). *Matahari Hambur Letusan Amat Kuat*. Available online at: http://www. Kosmo! Online - Dunia.mht (Last access date: 11 August 2011).

National Aeronautics and Space Administration (NASA) (2011). *Solar Cycle Prediction*. Available online at: http://solarscience.msfc.nasa.gov/predict.shtml (Last access date: 6 September 2011).

Nishida, A. (2010). The rise of space weather research in Japan. *Space Weather*, **8**: S04001.

Sizun, H. (2003). *Radio Wave Propagation for Telecommunication Applications*. Springer – Verlag, Paris.

Stanislawska, I., Bradley, P. A., Gulyaeva T. L. & Rothkaehl, H. (2005). Improved HF propagation and system performance predictions under ionospherically extreme conditions. *Adv. Space Res.*, **37**: 1069–1074.

Telefunken Racoms (2006). *Telcor R125F/T – 125 Watt HF-SSB Transceiver 1.6 to 30 MHz*. Telefunken, Berlin.

Zain, A.F.M. & Abdullah, M. (2000). Death of HF radio communication: Fact or myth? *4th International Wireless & Telecommunication Symposium,* 15-19 May 2000, Subang Jaya, Malaysia.

DETERMINATION OF SUITABLE RF DETECTORS FOR DETECTION OF WIRELESS SPY DEVICES

Dinesh Sathyamoorthy[1*], Nur Atiqah Japri[2], Mohd Faudzi Muhammad[1], Mohd Idris Ishak[1], Shalini Shafii[1], Aliah Ismail[1], Zainal Fitry M Amin[1], Siti Zainun Ali[1] & Mohd Hasrol Hisam M Yusoff[1]

[1]Instrumentation and Electronics Technology Division (BTIE), Science & Technology Research Institute for Defence (STRIDE), Ministry of Defence, Malaysia
[2]Faculty of Electrical and Electronics Engineering (FKEE), Universiti Tun Hussein Onn Malaysia (UTHM), Malaysia

[*]E-mail: dinesh.sathyamoorthy@stride.gov.my

ABSTRACT

In a previous study, the determination of suitable RF detectors for detection of wireless spy devices was conducted via the measurement of two key parameters; operating bandwidth and power level threshold. However, this study was limited to RF detectors with maximum operating frequency of up to 3 GHz (based on provided specifications). This paper is aimed at extending this study to RF detectors with specified maximum operating frequency of at least 6 GHz, which is considered as sufficient to cover standard wireless communications frequencies. Four RF detectors were considered for the study; Lanmda (model LM-DC 2), Skynet (model XB-68), Mini Gadgets (model CD-RFLD) and Comenzi (model RFS-DT1). Each of the evaluated RF detectors has a variable power level threshold. It was found that the Lanmda RF detector has the largest operating bandwidth (14 MHz - 4.85 GHz), followed by the Comenzi (9 MHz - 3.82 GHz) and Mini Gadgets (156 MHz - 3.44 GHz) RF detectors, while the Skynet RF detector has the smallest operating bandwidth (0.3 MHz - 2.91 GHz). It was observed that the evaluated RF detectors have varying power level threshold performances over frequency. The Comenzi RF detector generally has the lowest power level threshold performance over the tested frequencies. However, the Comenzi RF detector's significantly low power level thresholds could render it susceptible to false alarms, and make it difficult to hone in on possible targets. The Lanmda RF detector's power level thresholds make it suitable for the user to sweep the suspected area using its lowest power level threshold, and then, hone in on the target using higher power level thresholds. Furthermore, its larger operating bandwidth allows it to detect a wider range of signal frequencies. It should be noted that while this operating bandwidth is sufficient to cover most commonly used wireless communications frequencies, it is unsuitable for detection of the increasingly popular 5 and 5.8 GHz communications frequencies.

Keywords: *RF detector; maximum and minimum operating frequencies; operating bandwidth; power level threshold; signal detection.*

1. INTRODUCTION

Radio frequency (RF) detectors are used to detect RF signals transmitted in given proximities. They are generally used to detect transmissions from wireless spy devices, such as listening bugs or cameras, hidden in objects or covertly placed in rooms (hence the nickname "bug detector"). An RF detector is usually able to sweep a room or area for bugs and warn the user about active RF transmitters (Peterson, 2001, 2007; Taylor, 2005; Savry & Vacherand, 2010). RF detectors are also used to detect unauthorised wireless communications in restricted areas, which is usually followed by the immediate jamming of the corresponding signal (RABC, 2001; Sambhe *et al.*, 2008; Mishra, 2009; Burke & Owen, 2010). In addition, RF detectors provide important protection to pacemaker users (Pinski & Trohman, 2002a, b; Patel *et al.*, 2007; Seidman *et al.*, 2010), and to those who work in the presence of RF or microwave hazards (USN, 1997; Curtis, 2003; MOL, 2009; Wu *et al.*, 2010).

The performance of RF detectors is dependent on two key parameters; operating bandwidth and power level threshold. A number of wireless spy devices are designed to transmit signals with low power levels in order to avoid detection (Peterson, 2001, 2007; Davis, 2004; Taylor, 2005). An RF detector with low power level threshold is required for detection of such devices. However, if the detector has a power level threshold that is too low, it could cause false alarms, such as from mobile phones or Bluetooth devices. In addition, RF detectors with larger operating bandwidths allow for the detection of a wider range of transmitted signal frequencies (Peterson, 2001, 2007; Taylor, 2005; Savry & Vacherand, 2010).
In a previous study (Dinesh *et al.*, 2011), the determination of suitable RF detectors for detection of wireless spy devices was conducted via the measurement of operating bandwidth and power level threshold. However, this study was limited to RF detectors with maximum operating frequency of up to 3 GHz (based on provided specifications). This paper is aimed at extending this study to RF detectors with specified maximum operating frequency of at least 6 GHz, which is considered as sufficient to cover standard wireless communications frequencies (Webb, 2007; Molisch, 2011). The study was conducted via a series on tests held by the Instrumentation & Electronics Technology Division (BTIE) from March to June 2011 (STRIDE, 2011a-h). Four RF detectors were considered for the study (Figure 1):

i) Lanmda (model LM-DC2) (Lanmda, 2011)
ii) Skynet (model XB-68) (Skynet, 2011)
iii) Mini Gadgets (model CD-RFLD) (Mini Gadgets, 2011)
iv) Comenzi (model RFS-DT1) (Comenzi, 2011).

Based on the provided specifications of the respective RF detectors, the operating bandwidths of the devices are as shown in Table 1. Each of the evaluated RF detectors has a variable power level threshold. For the purposes of this study, the lowest power level threshold is considered as Channel A, while the highest power level threshold is considered as Channel B.

(a) **(b)** **(c)** **(d)**

Figure 1: The RF detectors evaluated in this study: (a) Lanmda (model LM-DC2); (b) Skynet (model XB-68); (c) Mini Gadgets (model CD-RFLD); (d) Comenzi (model RFS-DT1).

The power level thresholds for the RF detectors are not provided in the respective specifications. It should be noted that all four RF detectors are not high precision meters. The power level thresholds for the RF detectors are not fixed for the respective devices' operating bandwidths, but rather vary with frequency.

Table 1: Operating bandwidths of the evaluated RF detectors, based on provided specifications.

RF Detector	*Operating Bandwidth*
Lanmda (model LM-DC2)	10 MHz - 6 GHz
Skynet (model XB-68)	1 MHz - 6.5 GHz
Mini Gadgets (model CD-RFLD)	1 MHz - 6.5 GHz
Comenzi (model RFS-DT1)	1 MHz - 6.5 GHz

2. METHODOLOGY

The apparatus used in the tests were an Advantest U3751 spectrum analyser (Advantest, 2009), a Hewlett Packard 83620B signal generator (Hewlett Packard, 1998), an Aeroflex-IFR 2026B signal generator (Aeroflex, 2005), a Hyperlog 60180 directional antenna (Aaronia, 2009), and a Diamond RH799 omnidirectional antenna (Diamond, 2010). The test setup is as shown in Figure 2.

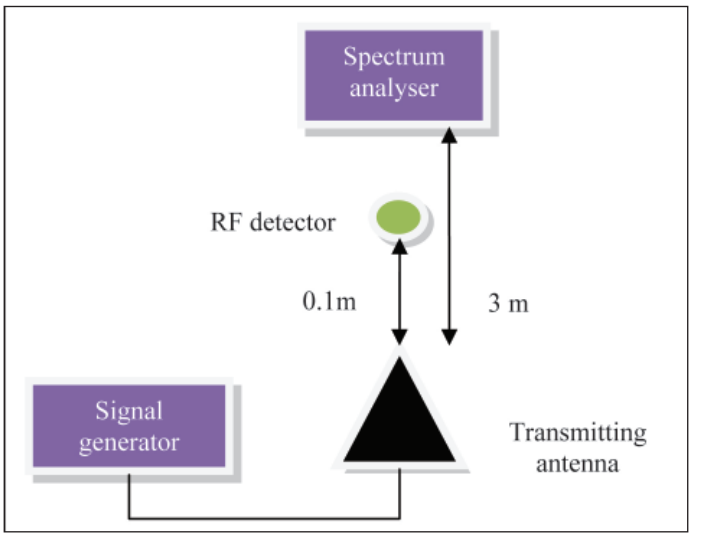

Figure 2: The test setup.

The spectrum analyser is placed 3 m away from the transmitting antenna to avoid damage from power levels that are too high. The computation of the received power levels at the location of the RF detector is performed as in the appendix. For transmissions below 700 MHz, the Diamond antenna is used, while for transmissions of 700 MHz and above, the Hyperlog antenna is used. For transmissions below 10 MHz, the IFR 2026B signal generator is used, while for transmissions of 10 MHz and above, the Hewlett Packard 82620B signal generator is used. For the each RF detector, the test procedure is conducted for both Channels A and B.

In order to determine the minimum operating frequencies of each RF detector, transmission is set at power level of 24 dBm and frequency of 0.3 MHz (minimum transmitted frequency allowed by the IFR 2026B signal generator). The frequency is increased incrementally by 0.1 MHz until the signal is detected. The received power level at this point is recorded. These steps are repeated for transmission power levels of 23 to -20 dBm (decrements of 1 dBm). In order to determine the maximum operating frequencies of each RF detector, the procedure is repeated, with the starting transmission frequency set at 8 GHz, and the frequency being decreased decrementally by 0.1 MHz until signal detection.

In order to determine the power level threshold of each RF detector, transmission is set at power level of -30 dBm and frequency of 20 MHz. The power level is increased incrementally by 0.1 dBm until the signal is detected. The received power level at this point is recorded. The procedure is repeated for transmission frequencies of 40 to 100 MHz (increments of 20 MHz), and 200 MHz to 8 GHz (increments of 100 MHz).

3. RESULTS AND DISCUSSION

The measured minimum and maximum operating frequencies of the RF detectors over the tested power levels are as shown in Figures 3 and 4 respectively. The maximum operating frequency increases with power level, and vice-versa for the minimum operating frequency. All the plots have linear regressions with high coefficients of determination R^2, indicating that the variances of these parameters are largely due to the variance of power level, rather than from other factors.The errors in the goodness of fit plots were caused by detector oscillator instability.

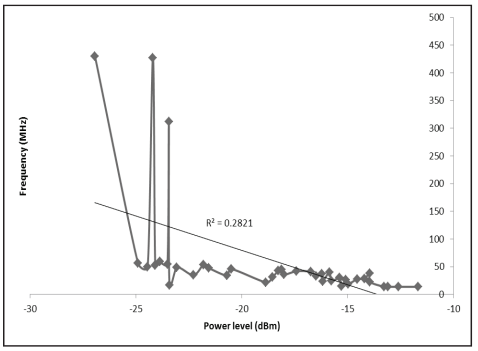

(a)

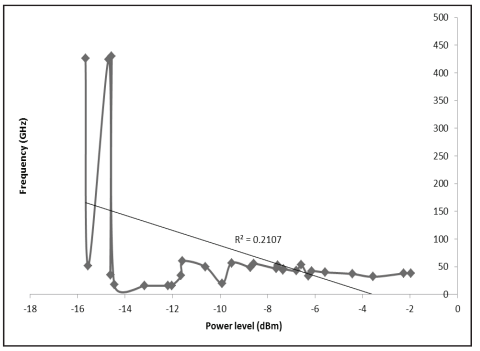

(b)

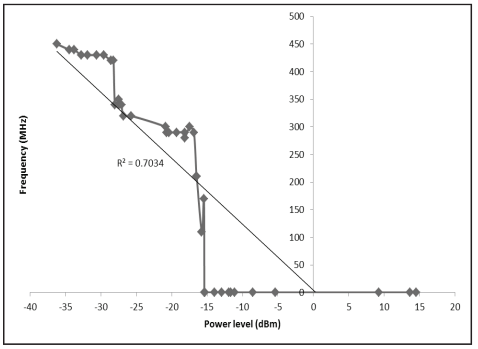

(c)

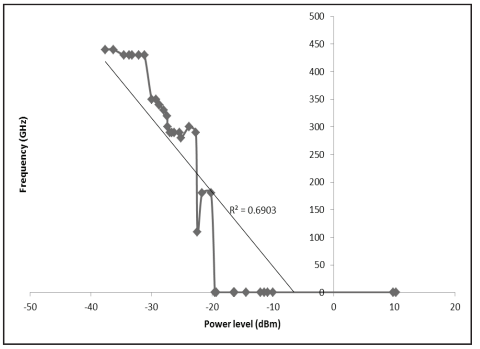

(d)

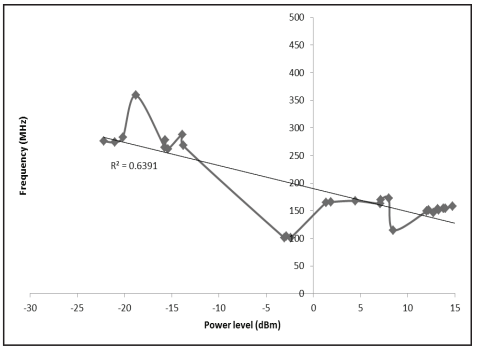

(e)

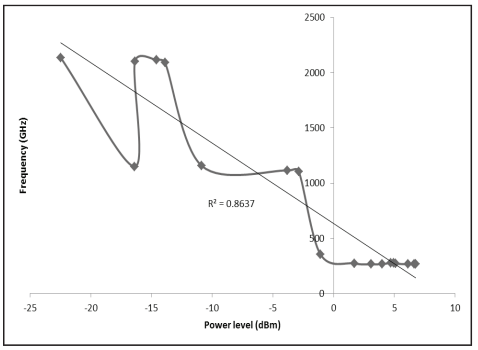

(f)

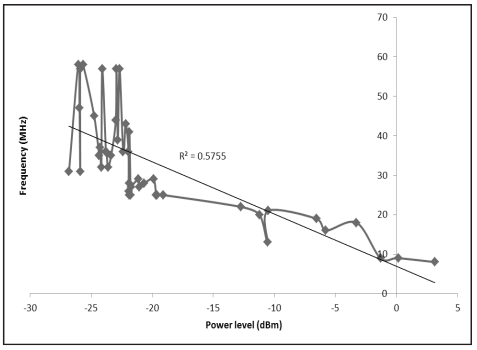

(g)

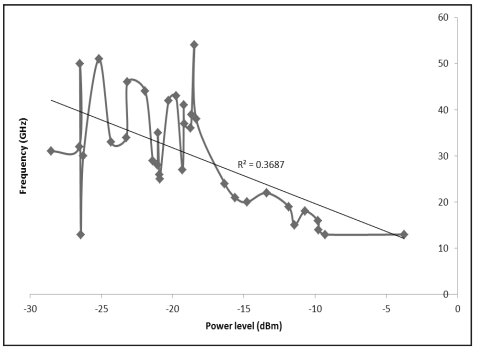

(h)

Figure 3: Minimum operating frequencies of the evaluated RF detectors: (a) Lanmda (model LM-DC2): Channel A; (b) Lanmda (model LM-DC 2): Channel B; (c) Skynet (model XB-68): Channel A; (d) Skynet (model XB-68): Channel B; (e) Mini Gadgets (model CD-RFLD): Channel A; (f) Mini Gadgets (model CD-RFLD): Channel B; (g) Comenzi (model RFS-DT1): Channel A; (h) Comenzi (model RFS-DT1): Channel B.

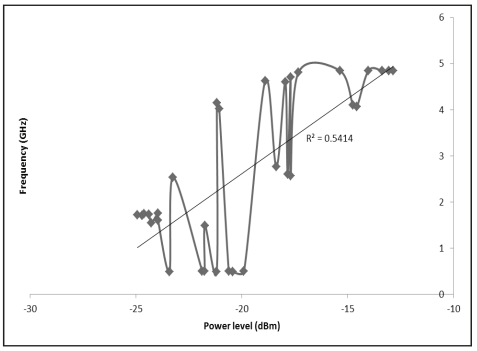

(a)

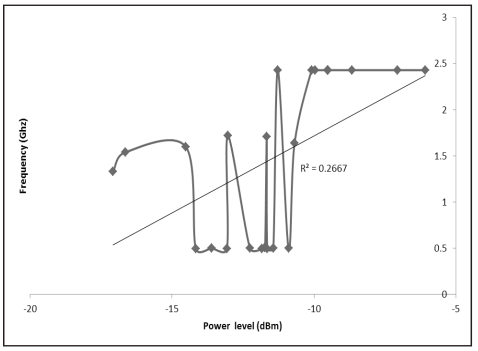

(b)

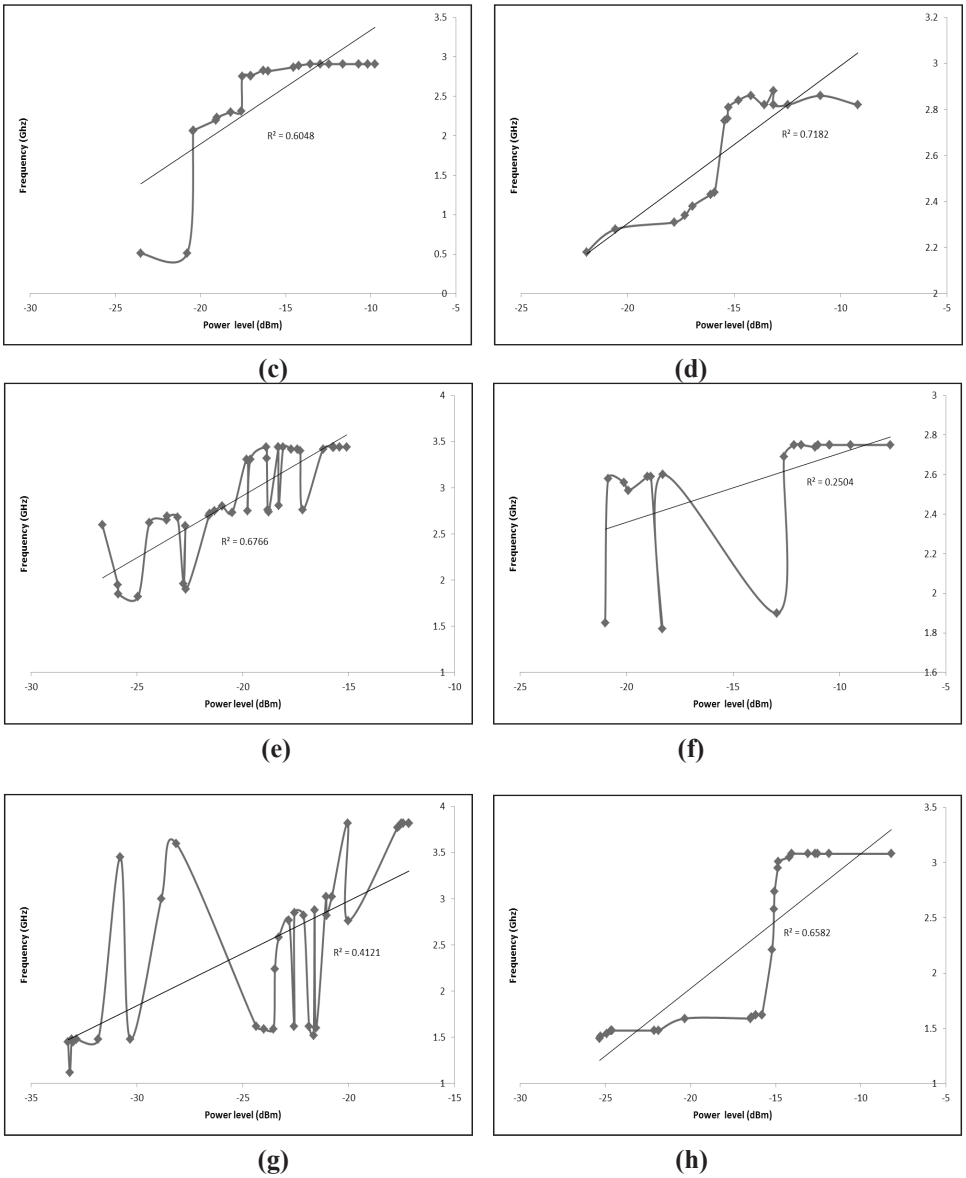

Figure 4: Maximum operating frequencies of the evaluated RF detectors: (a) Lanmda (model LM-DC2): Channel A; (b) Lanmda (model LM-DC 2): Channel B; (c) Skynet (model XB-68): Channel A; (d) Skynet (model XB-68): Channel B; (e) Mini Gadgets (model CD-RFLD): Channel A; (f) Mini Gadgets (model CD-RFLD): Channel B; (g) Comenzi (model RFS-DT1): Channel A; (h) Comenzi (model RFS-DT1): Channel B.

The operating bandwidths of the RF detectors, determined based on minimum and maximum operating frequencies at the highest power levels at which stability in the plots was achieved, are as shown in Table 2. While there are tested power levels that have lower minimum and higher maximum operating frequencies, respectively, this is due to detector oscillator instability. As expected, for each RF detector, Channel A has larger operating bandwidth as compared to Channel B. However, for the Skynet RF detector, the difference in operating bandwidth for Channels A and B is much smaller as compared to the other RF detectors. Of the evaluated RF detectors, the Lanmda RF detector has the largest operating bandwidth (14 MHz - 4.85 GHz), followed by the Comenzi (9 MHz - 3.82 GHz) and Mini Gadgets (156 MHz - 3.44 GHz) RF detectors, while the Skynet RF detector has the smallest operating bandwidth (0.3 MHz - 2.91 GHz).

Table 2: Measured operating bandwidths of the evaluated RF detectors.

RF Detector	*Operating Bandwidth*	
	Channel A	**Channel B**
Lanmda (model LM-DC2)	14 MHz – 4.85 GHz	38 MHz – 2.43 GHz
Skynet (model XB-68)	0.3 MHz – 2.91 GHz	0.3 MHz – 2.82 GHz
Mini Gadgets (model CD-RFLD)	156 MHz - 3.44 GHz	266 MHz - 2.75 GHz
Comenzi (model RFS-DT1)	9 MHz - 3.82 GHz	16 MHz – 3.08 GHz

Based on the plots in Figure 5, it is observed that the evaluated RF detectors have varying power level threshold performances over frequency. For the Lanmda, Mini Gadgets and Comenzi RF detectors, Channel A has lower power level threshold as compared to Channel B. However, for the Skynet RF detector, there are no significant differences between the power level threshold performances of Channels A and B. From the comparison of the power level thresholds of each RF detector's Channel A (Figure 6), it is observed that the Comenzi RF detector generally has the lowest power level threshold over the tested bandwidths.

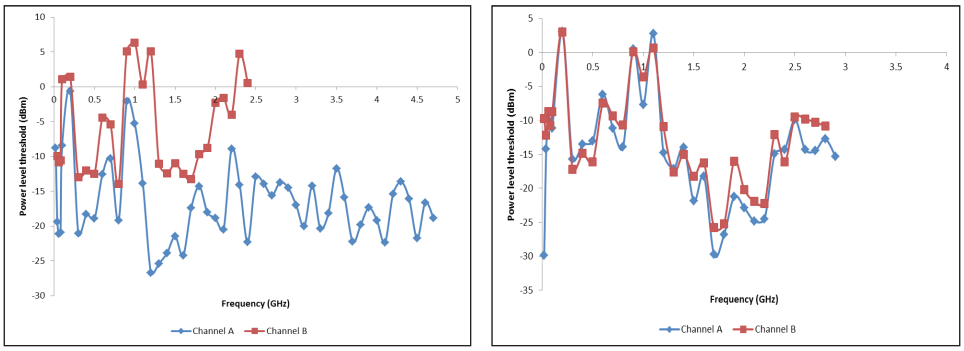

(a) **(b)**

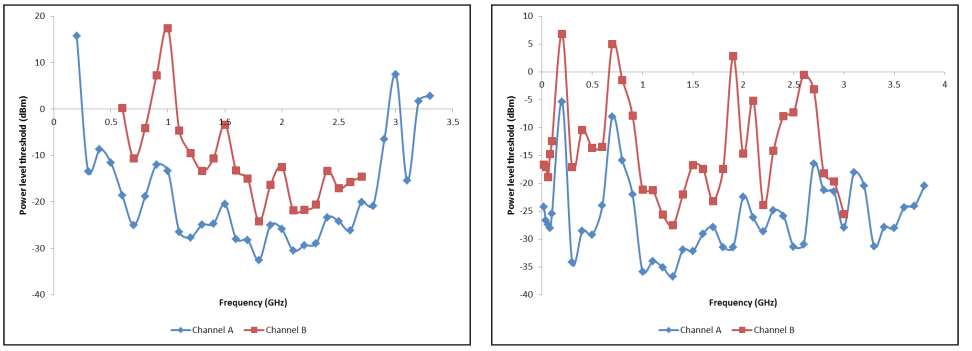

(c) **(d)**

Figure 5: Power level thresholds of the evaluated RF detectors over the tested frequencies: (a) Lanmda (model LM-DC2); (b) Skynet (model XB-68); (c) Mini Gadgets (model CD-RFLD); (d) Comenzi (model RFS-DT1).

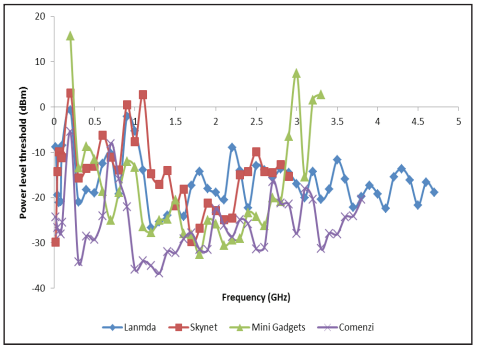

Figure 6: Power level thresholds of Channel A of the evaluated RF detectors.

Based on the results of the tests conducted on operating bandwidth and power level threshold, it was determined that the Lanmda (having the largest operating bandwidth) and Comenzi (having the lowest power level threshold performance) RF detectors were more suitable for detection of wireless spy devices as compared to the other evaluated RF detectors. A further comparison of the Lanmda and Comenzi RF detectors' Channels A and B (Figure 7) shows that the Comenzi RF detector's Channel B has a power level threshold performance that is approximately similar, albeit less steady, to the Lanmda RF detector's Channel A.

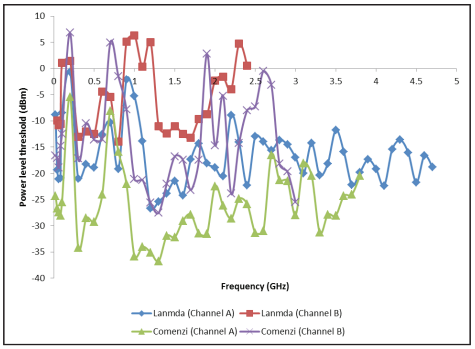

Figure 7: Comparison of power level thresholds of Channels A and B of the Lanmbda and Comenzi RF detectors.

4. CONCLUSION

Based on the results obtained, it was determined that the Lanmda RF detector has the largest operating bandwidth, while the Comenzi RF detector has the lowest power level threshold performance. The Comenzi RF detector's significantly low power level thresholds could render it susceptible to false alarms, and make it difficult to hone in on possible targets. The Lanmda RF detector's power level thresholds make it suitable for the user to sweep the suspected area using its lowest power level threshold, and then, hone in on the target using higher power level thresholds. Furthermore, its larger operating bandwidth allows it to detect a wider range of signal frequencies. It should be noted that while this operating bandwidth is sufficient to cover most commonly used wireless communications frequencies, it is unsuitable for detection of the increasingly popular 5 and 5.8 GHz communications frequencies.

ACKNOWLEDGEMENT

This study was conducted when the second author was an industrial trainee with the Science & Technology Research Institute for Defence (STRIDE). The authors are grateful to Mr. Kamarulzaman Mustapa, Mdm. Jamilah Jaafar and Mr. Muhammad Adib Idris for their support. The authors would like to thank the reviewers, Dr. Mahdi Che Isa and Mdm. Halijah Ahmad, for their suggestions that have helped strengthen this manuscript.

REFERENCES

Aaronia (2009). *Precompliance Test Antenna Series HyperLOG® 60xxx: Span 680 MHz to 18 GHz*. Aaronia AG, Strickscheid, Germany.

Advantest (2009). *U3741/3751 Spectrum Analyzers*. Advantest Corporation, Chiyoda-ku, Tokyo.

Aeroflex (2005). *2026B Multi-source Generator.* Aeroflex, Plainview, New York.

Burke, T.W. & Owen, S.S. (2010). Cell phones as prison contrabands. *FBI Enforcement Bull.*, **12**: 10-15.

Comenzi (2011). *Detector Radio RFS-DT1*. Comenzi Net Srl, Bucharest, Romania.

Curtis, R. (2003). *Introduction to Radio Frequency Radiation*. Occupational Safety & Health Administration (OSHA), US Department of Labor, Washington D.C.

Davis, B. (2004). Spy gear: Modern surveillance tools use the newest technology to catch crooks on the sly. *Police Law Enforcement Mag.*, **28**: 38-43.

Diamond (2010). *RH799: 70 to 1000MHz Wide-band Antenna*. Diamond Antenna Corporation, Tokyo, Japan.

Dinesh, S., Mohd. Faudzi, M., Mohd Idris, I.,, Shalini, S., Jamilah, J., Aliah, I.,, Zainal Fitry, M.A., Siti Zainun, A. & Mohd Hasrol Hisam, M.Y. (2011). Evaluation of operating bandwidth and power level threshold of RF detectors. *Defence S&T Tech. Bull.*, **4**: 31-38.

Hewlett Packard (1998). *HP 8360B Series Synthesized Swept Signal Generators*. Hewlett Packard, Chicago.

Lanmda (2011). *Lanmda LM-DC2 Wireless Surveillance Detector*. Lanmda Co. Ltd., Shenzhen, China.

Mini Gadgets (2011). *Camera Detectors: CD-RFLD*. Mini Gadgets Inc., Alpharetta, Georgia.

Ministry of Labour (MOL) (2009). *Radiofrequency and Microwave Radiation in the Workplace*. Ministry of Labour (MOL), Ontario.

Mishra, N.K. (2009). Development of GSM - 900 mobile jammer: An approach to overcome existing limitation of jammer. *Fifth IEEE Conference on Wireless Communication and Sensor Networks (WCSN)*, 15-18 December 2009, Allahabad, India.

Molisch, F.A. (2011). *Wireless Communications*. John Wiley & Sons Ltd., Chichester, West Sussex.

Patel, M.B., Thaker, J.P., Punnam, S. & Jongnarangsin, K. (2007). Pacemaker interference with an iPod. *Human Rhythm*, **4**: 781-784.

Peterson, J.K. (2001). *Understanding Surveillance Technologies: Spy Devices, Their Origins & Applications*. CRC Press, Boca Raton, Florida.

Peterson, J.K. (2007). *Understanding Surveillance Technologies: Spy Devices, Privacy, History & Applications.*. Auerbach Publications, Boca Raton, Florida.

Pinski, S.L. & Trohman, R.G. (2002a). Interference in implanted cardiac devices,

Part I. *Pace*, **25**: 1367-1381.
Pinski, S.L. & Trohman, R.G. (2002b). Interference in implanted cardiac devices, Part II. *Pace*, **25**: 1496-1509.
Radio Advisory Board of Canada (RBAC) (2001). *Use of Jammer and Disabler Devices for Blocking PCS, Cellular & Related Services*. Radio Advisory Board of Canada (RBAC), Ottawa, Ontario
Sambhe, V.K., Kale, D.S.K., Wasule, A. & Neema, S. (2008). Antenna for mobile phone jammer . *First International Conference on Emerging Trends in Engineering and Technology*. 16-18 July 2008, G. H. Raisoni College of Engineering, Nagpur, India.
Savry, O. & Vacherand, F. (2010). Security and privacy protection of contactless devices. In Giusto, D., Iera, Morabito, G. & Atzori (Eds.), *The Internet of Things: 20th Tyrrhenian Workshop on Digital Communications*. Springer, New York, pp. 409-420.
Science & Technology Research Institute for Defence (STRIDE) (2011a). *Evaluation of Operating Bandwidth of a LM-DC2 Lanmda RF Detector*. Science & Technology Research Institute for Defence (STRIDE), Ministry of Defence, Malaysia.
Science & Technology Research Institute for Defence (STRIDE) (2011b). *Evaluation of Power Level Threshold of a LM-DC2 Lanmda RF Detector*. Science & Technology Research Institute for Defence (STRIDE), Ministry of Defence, Malaysia.
Science & Technology Research Institute for Defence (STRIDE) (2011c). *Evaluation of Operating Bandwidth of a Mini Gadgets (Model CD-RFLD) RF Detector*. Science & Technology Research Institute for Defence (STRIDE), Ministry of Defence, Malaysia.
Science & Technology Research Institute for Defence (STRIDE) (2011d). *Evaluation of Power Level Threshold of a Mini Gadgets (Model CD-RFLD) RF Detector*. Science & Technology Research Institute for Defence (STRIDE), Ministry of Defence, Malaysia.
Science & Technology Research Institute for Defence (STRIDE) (2011e). *Evaluation of Operating Bandwidth of a Comenzi (Model RFS-DT1) RF Detector*. Science & Technology Research Institute for Defence (STRIDE), Ministry of Defence, Malaysia.
Science & Technology Research Institute for Defence (STRIDE) (2011f). *Evaluation of Power Level Threshold of a Comenzi (Model RFS-DT1) RF Detector*. Science & Technology Research Institute for Defence (STRIDE), Ministry of Defence, Malaysia.
Science & Technology Research Institute for Defence (STRIDE) (2011g). *Evaluation of Operating Bandwidth of a Skynet (Model XB-68) RF Detector*. Science & Technology Research Institute for Defence (STRIDE), Ministry of Defence, Malaysia.
Science & Technology Research Institute for Defence (STRIDE) (2011h). *Evaluation of Power Level Threshold of a Skynet (Model XB-68) RF Detector*.

Science & Technology Research Institute for Defence (STRIDE), Ministry of Defence, Malaysia.

Seidman, S., Randall, Brockman, R., Lewis, B.M., Guag, J., Shein, M.J., Clement, W.J., Kippola, J., Digby, D., Barber, C. & Huntwork, D. (2010). In vitro tests reveal sample radiofrequency identification to implantable pacemakers and implantable cardioverter-defibrillators. *Human Rhythm*, **7**: 99-107

Sambhe, V.K., Kale, D.S.K., Wasule, A. & Neema, S. (2008). Antenna for mobile phone jammer . *First International Conference on Emerging Trends in Engineering and Technology*. 16th-18th July 2008, G. H. Raisoni College of Engineering, Nagpur, India.

Skynet (2011). *XB-68 Sky Net Multi-Functional Detector*. Skynet Technology Development Ltd., North Point, Hong Kong.

Taylor, C. (2005). *The Red Balloon*. Pinpoint Productions, Inc., Vancouver, Canada.

US Navy (USN) (1997). *Electronics Technician: Volume 1 - Safety*. US Navy (USN), Washington D.C.

Webb, W. (2007). *Wireless Communications: The Future*. John Wiley & Sons Ltd., Chichester, West Sussex.

Wu, C.Y., Lee, T.S. & Hsue, C.W. (2010). Mobile phone users and base stations versus human health concern. *2010 Asia Pacific Symposium on Electromagnetic Compatibility (APEMC)*, 12-16 April 2010, Beijing, China.

APPENDIX

Power level estimation:

P_T : Transmitter power
P_R : Receiver power
G_T : Transmitter gain
G_R : Receiver gain
L : Free-space path loss
L_E : External losses
R : Distance (km)
f : Frequency (MHz)

$$P_R = P_T + G_T + G_R - L - L_E \quad \text{(A1)}$$

$$L = 32.44 + 20\log R + 20\log f \quad \text{(A2)}$$

Effective transmitted power P_{Teff}:

$$P_{T_{eff}} = P_T + G_T \quad \text{(A3)}$$

Effective received power P_{Reff}:

$$P_{R_{eff}} = P_R - G_R \quad \text{(A4)}$$

With L_E and f being constant:

$$P_{R_{eff}} = P_{T_{eff}} - 20\log R - L_O - G_R \quad \text{(A5)}$$

where:

$$L_O = 32.44 + 20\log f + L_E \quad \text{(A6)}$$

COMPARATIVE TEST OF SIGNALS OF MOBILE PHONE JAMMERS

Nur Atiqah Japri[1*], Dinesh Sathyamoorthy[2], Mohd Faudzi Mohammad[2], Mohd Idris Ishak[2], Shalini Shafii[2], Aliah Ismail[2], Zainal Fitry M Amin[2] & Siti Zainun Ali[2]

[1]Faculty of Electrical and Electronic Engineering, Universiti Tun Hussein Onn, Malaysia
[2]Instrumentation & Electronics Technology Division (BTIE), Science & Technology Research Institute for Defence (STRIDE), Ministry of Defence, Malaysia

*E-mail: ekaries87@gmail.com

ABSTRACT

On 28 June 2011, the Instrumentation & Electronics Technology Division (BTIE) conducted a test to compare the transmitted signals of two mobile phone jammers (MPJs) a portable MPJ (MPJ34) and a high powered MPJ (MPJ2000). Both MPJs are designed to operate in the bandwidths of Code Division Multiple Access (CDMA), Global System for Mobile Communications (GSM), Digital Cellular System (DCS) and Third Generation Mobile Telecommunications (3G). The test was conducted in BTIE's semi anechoic chamber in order to avoid unintended interference signals. It was observed that for all the tested bandwidths, the MPJ2000 jammer has significantly higher transmitted power levels as compared to the MPJ34 jammer. Hence, of the two jammers, the MPJ2000 jammer is able to conduct mobile phone jamming for significantly larger radiuses. It should be noted that in addition to transmitted power levels, other parameters can affect an MPJ's jamming radius, including proximity to base transceiver stations (BTSs), presence of buildings and landscape, and temperature and humidity.

Keywords: *Mobile phone jammer (MPJ); transmitted signals; power level; spectrums; jamming radius.*

1. INTRODUCTION

Jamming is defined as the broadcasting of a strong signal that overrides or obscures the signal being jammed (DOA, 2009; JCS, 2007; Poisel, 2002). A mobile phone jammer (MPJ) (also known as mobile phone silencer) is a device that purposefully tries to interfere with the physical transmission and reception of mobile / wireless communications. It prevents mobile phones from receiving and transmitting signals to base transceiver stations (BTSs). This is known as a denial-of-service attack, in

that the MPJ denies service of the radio spectrum to mobile phone users within range of the jamming device (Bennahum, 2003; Shah *et al.*, 2008; Wollenhaupt, 2008; ACMA, 2010).

A MPJ interrupts communications signals by sending out jamming signals along the same frequency as the communications signal. The transmitted jamming signals are strong enough to interfere with the communications signal. Communications devices are commonly designed to operate across several bands. Since mobile phones are two way communications devices, MPJs are designed to work by either disrupting mobile phone to BTS (uplink) signals or BTS to mobile phone (downlink) signals, with most MPJs focusing on the weaker downlink signals. The jamming range of a MPJ depends on its transmitted powers and frequencies, the mobile phones it is attempting to block, the local environment (e.g. buildings and landscape), and temperature and humidity (RSAC 2000; Bennahum, 2003; Shah *et al.*, 2008; Wollenhaupt, 2008; ACMA, 2010; Sander & Johnk, 2010).

While older types of MPJs could only operate on a few frequency ranges, current types of MPJs can block all widely used bandwidths, including Code Division Multiple Access (CDMA), Global System for Mobile Communications (GSM), Digital Cellular System (DCS) and Third Generation Mobile Telecommunications (3G). The latest types of MPJs are very effective against modern communications devices which are able to hop between different frequencies and systems. Future MPJs are expected to be expanded to include other communications frequency bands used for other wireless technologies, such as Wi-Fi and WiMAX, in order to jam entire communications systems (Wollenhaupt, 2008; ACMA, 2010).

MPJs were originally developed for law enforcement and military personnel to interrupt communications by criminals and terrorists, to protect secure military areas from electronic surveillance, and to deter mobile phone triggered bombs. In addition, MPJs can be used in areas where radio transmissions are dangerous (e.g. areas with a potentially explosive atmosphere), such as chemical storage facilities or grain elevators. Corporations also use jammers to stop corporate espionage by blocking voice and photo transmissions from camera phones (Efstathiou, 2002; Bennahum, 2003; Wollenhaupt, 2008; Netline, 2011).

However, many countries only allow MPJs for military and government use only, and have outlawed civilian sale and use of jammers. This is because unauthorised jamming can interfere with emergency communications between police and rescue personnel, aid in criminal activity, and disrupt medical equipment such as pacemakers. Furthermore, the triangulation of the exact position of a mobile phone jamming source is a difficult and time consuming task (RSAC, 2000; Efstathiou, 2002; Bennahum, 2003; Wollenhaupt, 2008; ACMA, 2010; FCC, 2011).

On 28 June 2011, the Instrumentation & Electronics Technology Division (BTIE) conducted a test to compare the transmitted signals of two MPJs; a portable MPJ

(MPJ34) and a high powered MPJ (MPJ2000) (Figure 1) (STRIDE, 2011a). Based on the provided specifications, both MPJs are designed to jam the bandwidths in Table 1.

(a) **(b)**

Figure 1: MPJs tested in this study: (a) MPJ34; (b) MPJ2000.

Table 1: Bandwidths that are jammed by the evaluated MPJs, based on the provided specifications.

Signal	Bandwidth (MHz)
Code Division Multiple Access (CDMA)	850 – 894
Global System for Mobile Communications (GSM)	925- 960
Digital Cellular System (DCS)	1,805 – 1,990
Third Generation Mobile Telecommunications (3G)	2,100 – 2,170

The jamming radius of the MPJ34 jammer is 15 m, and 40 m for the MPJ2000 jammer. The MPJ2000 jammer has four antennas, for transmission on the bandwidths of CDMA, GSM, DCS and 3G, while the MPJ34 jammer has only three antennas, for transmission of the bandwidths of CDMA / GSM, DCS and 3G. This paper is aimed at discussing the procedures employed in the conducted test, and the findings obtained.

2. METHODOLOGY

An Advantest U3571 spectrum analyser (Advantest, 2009) was used to measure the signals of the MPJs. The test was conducted in BTIE's semi anechoic chamber (A. Faridz *et al.*, 2010) in order to avoid unintended interference signals. The test setup employed is as shown in Figure 2. For each MPJ, the spectrums were recorded prior to signal transmission, for the jammer switched on with all antennas installed, and with the jammer's separate individual antennas installed.

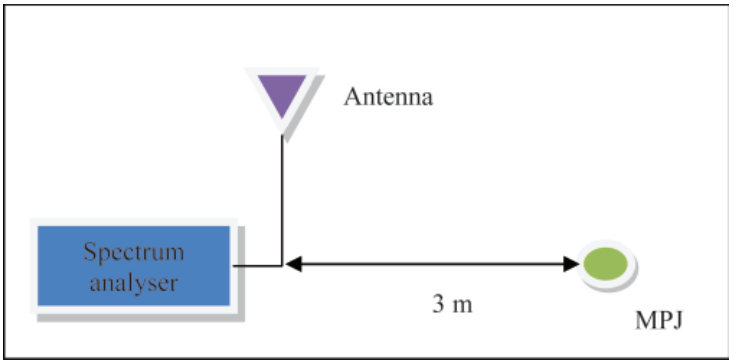

Figure 2: The test setup.

3. RESULTS AND DISCUSSION

Spectrums for signals measured in the frequency range of 700 MHz to 2.4 GHz are shown in the Figures 3 to 9. The measured transmitted power levels of the jammers are as shown in Table 2.

No discernible signals were observed in the measurement span prior to signal transmission (Figure 3). Based on the comparison of the MPJs with all antennas installed (Figure 4), it is observed that the MPJ2000 jammer has higher transmitted power levels as compared to the MPJ34 jammer. From the spectrum of signals recorded with none of the antennas installed (Figure 5), but the jammers being switched on, it was observed that was no signals were received for the MPJ34 jammer, and some residual signals in the DCS and 3G bandwidths for the MPJ2000 jammer, albeit much weaker as compared to Figure 4(b).

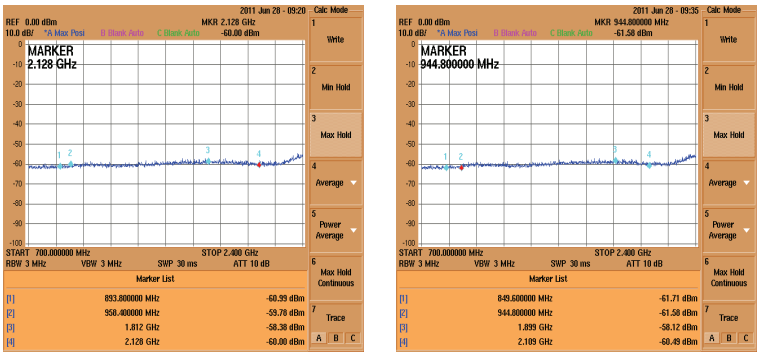

(a) **(b)**

Figure 3: Spectrums recorded prior to transmission of signals: (a) MPJ34; (b) MPJ2000.

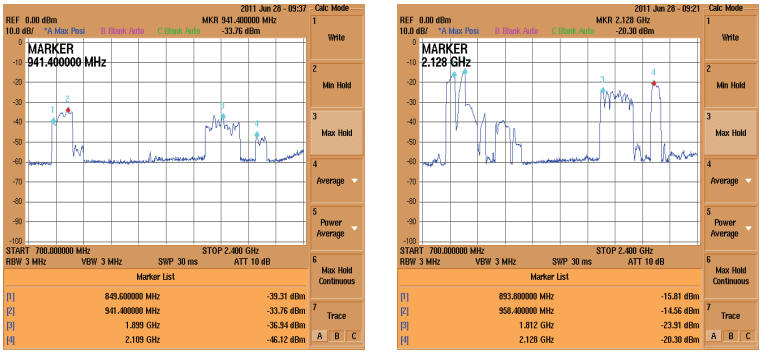

(a) (b)

Figure 4: Spectrums recorded with all antennas (CDMA, GSM, DCS and 3G) installed: (a) MPJ34; (b) MPJ2000.

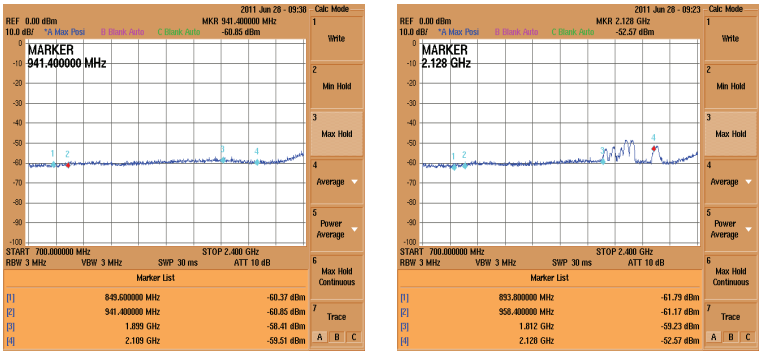

(a) (b)

Figure 5: Spectrums recorded with none of the antennas installed: (a) MPJ34; (b) MPJ2000.

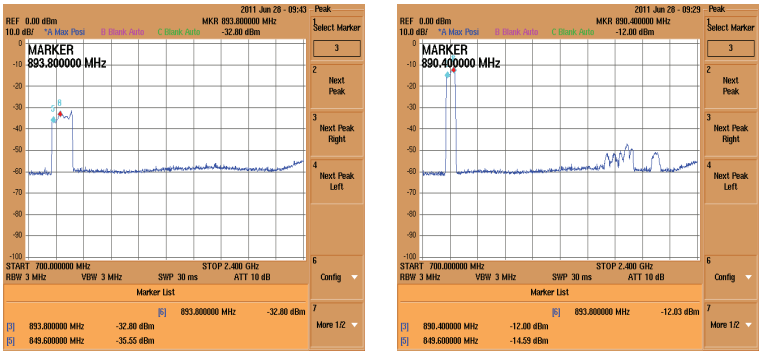

(a) (b)

Figure 6: Spectrums recorded with only the CDMA antenna installed: (a) MPJ34; (b) MPJ2000.

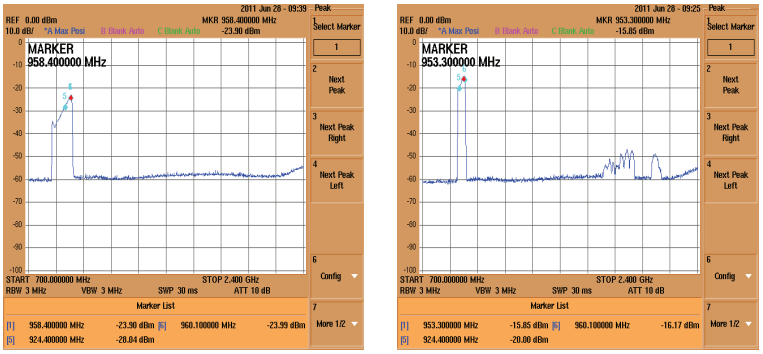

(a) (b)

Figure 7: Spectrums recorded with only the GSM antenna installed: (a) MPJ34; (b) MPJ2000.

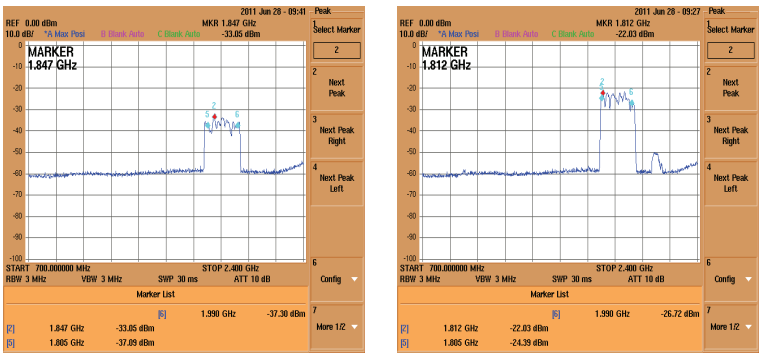

(a) (b)

Figure 8: Spectrums recorded with only the DCS antenna installed: (a) MPJ34; (b) MPJ2000.

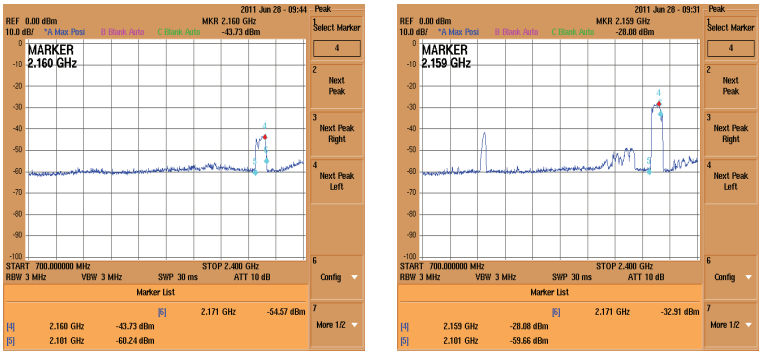

(a) (b)

Figure 9: Spectrums recorded with only the 3G antenna installed: (a) MPJ34; (b) MPJ2000.

Table 2: Measured received power levels for the MPJ34 and MPJ2000 jammers.

Bandwidth	Power Level (dBm)	
	MPJ34	MPJ2000
CDMA	-32.80	-12.00
GSM	-23.90	-15.85
DCS	-33.05	-22.03
3G	-43.73	-28.08

For the measurements conducted with only the individual antennas installed:

a. Only the CDMA antenna installed (Figure 6): The highest power level transmitted by the MPJ34 jammer was –32.8 dBm at 893.8 MHz, and -12.00dBm at 890.4 MHz for the MPJ2000 jammer.
b. Only the GSM antenna installed (Figure 7): The highest power level transmitted by the MPJ34 jammer was -23.90 dBm at 958.4 MHz, and -15.85dBm at 953.3 MHz for the MPJ2000 jammer.
c. Only the DCS antenna installed (Figure 8): The highest power level transmitted by the MPJ34 jammer was -33.05dBm at 1.847 GHz, and -22.03dBm at 1.812 GHz for the MPJ2000 jammer.
d. Only the 3G antenna installed (Figure 9): The highest power level transmitted by the MPJ34 jammer was -43.73 dBm at 2.160 GHz, and -28.08 dBm at 2.159 GHz for the MPJ2000 jammer.

Based on the measured received power levels for MPJs, the effective isotropic radiated power (EIRP) (Table 3) and received power levels over various distances (Figure 10) are estimated using free space propagation computation (appendix). This computation did not take into possible external interferences and losses, and hence, the actual EIRP would be larger, while the actual received power levels would be smaller.

Table 3: Estimated EIRPs of the MPJs.

Bandwidth	EIRP (dBm)	
	MPJ34	MPJ2000
CDMA	7.97	28.77
GSM	17.64	25.69
DCS	14.51	25.53
3G	4.90	20.55

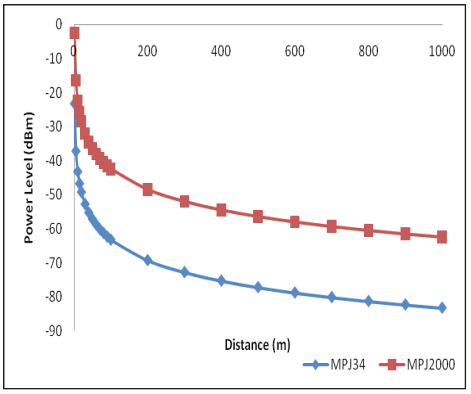

(a)

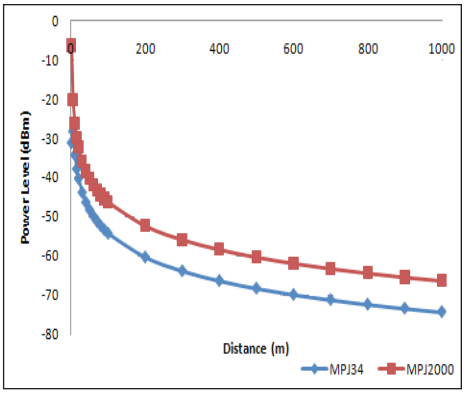

(b)

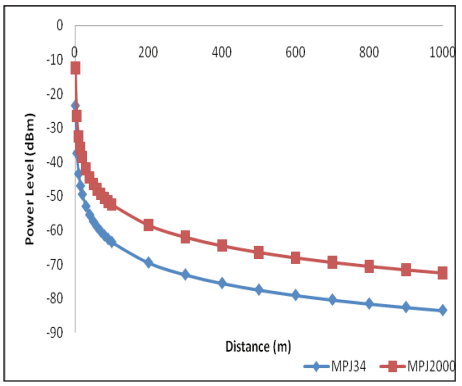

(c)

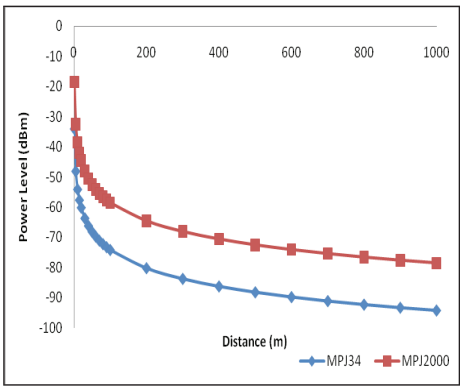

(d)

Figure 10: Estimated received power levels over varying distances for bandwidths of: (a) CDMA; (b) GSM; (c) DCS; (d) 3G.

It is observed that for all the tested bandwidths, the MPJ2000 jammer has significantly higher EIRP as compared to the MPJ34 jammer, and as a result, higher received power levels over the various distances. Hence, of the two jammers, the MPJ2000 jammer is able to conduct mobile phone jamming for significantly larger radiuses.

For the MPJ2000 jammer, it is noted that while the EIRPs for the tested bandwidths are almost similar, bandwidths with lower frequencies (CDMA and GSM) have higher received power levels as compared to bandwidths with higher frequencies (DCS and 3G). This occurs as increase in frequency causes increased signal propagation loss. In addition, environmental parameters such as temperature and humidity have more pronounced effect on signals with higher frequencies as compared to signals with lower frequencies (Poisel, 2002; Molisch, 2011).

Based on the findings of a separate test, it was determined that the minimum interference signal power level required to jam the GSM reception of a Nokia E52 mobile phone (Nokia, 2009) at the STRIDE Block B car park (N 2º 58' 4.9" E 101º 48' 35.5") is -41.55 dBm (STRIDE, 2011b). Based on this minimum jamming power level, the estimated jamming radiuses of both MPJs are as shown in Table 4.

Table 4: Estimated jamming radius of the MPJs for minimum jamming power of -41.55 dBm.

Bandwidth	Distance (m)	
	MPJ34	MPJ2000
CDMA	8.22	90.08
GSM	22.89	57.83
DCS	7.98	28.39
3G	2.33	14.15

It should be noted that these jamming radiuses are not fixed, but rather, are dependent on a number of factors. As the estimation was made solely based on free space propagation, the actual jamming radius would be smaller due to various losses. In addition, the minimum interference signal power level required to jam a mobile phone is dependent on several factors, including proximity to BTSs, presence of buildings and landscape, temperature and humidity, and the design characteristics of the mobile phone.

While both MPJs were designed for use within enclosed environments, signal leakages often occur, resulting in interference outside the intended area. If the MPJs are installed in areas with large numbers of windows, such as offices or libraries, the signal leakage and interference range could be much larger (RSAC, 2000; Sander & Johnk, 2010). The MPJ2000 jammer, having significantly higher transmitted power, is more likely to cause such signal leakages. An alternative to mitigate such possible interferences is to employ RF detectors to detect unauthorised mobile phone communications in restricted areas, followed by the immediate activation of the MPJ (RABC, 2001; Sambhe *et al.*, 2008; Mishra, 2009; Burke & Owen, 2010).

4. CONCLUSION

This test has highlighted the effects of two MPJs; a portable jammer (MPJ34) and a high powered jammer (MPJ2000). Both MPJs operate on signals in the bandwidths of GSM, DCS, CDMA and 3G. Based on the results obtained, it is observed that of the two MPJs, the MPJ2000 jammer has significantly higher transmitted power levels for the tested bandwidths, and hence, larger jamming radius. It should be noted that in addition to transmitted power levels, other parameters can affect an MPJ's jamming radius, including proximity to BTSs, presence of buildings and

landscape, and temperature and humidity. It is proposed that the study be extended to evaluate a wider range of MPJ products.

ACKNOWLEDGEMENT

This study was conducted when the first author was an industrial trainee with the Science & Technology Research Institute for Defence (STRIDE). The authors are grateful to Mr. Kamarulzaman Mustapa, Mr. Ahmad Faridz Ahmad Ghafar and Mdm. Jamilah Jaafar for their support. The authors would like to thank the reviewers, Dr. Mahdi Che Isa and Mdm. Nor Hafizah Mohamed, for their suggestions that helped improve this manuscript.

REFERENCES

A. Faridz, A.G., M. Razali, M. Y. & W. Salwa, W.H. (2010). STRIDE's 3 meters EMC semi-anechoic chamber: Design considerations and compliance to standards. *2010 IEEE Asia-Pacific Conference on Applied Electromagnetics (APACE 2010)*, 9-11 November 2010, Tiara Beach Resort, Port Dickson, Negeri Sembilan.

Advantest (2009). *U3741/3751 Spectrum Analyzers*. Advantest Corporation, Chiyoda-ku, Tokyo.

Australian Communications and Media Authority (ACMA) (2010). *Review of Mobile Phone Jammer Prohibition: Public Discussion Paper*. Australian Communications and Media Authority (ACMA), Australian Government, Canberra.

Bennahum, D.S. (2003). *Cell-Phone Jammers May Soon Be All Over*. Available online at: http://www.slate.com/id/2092059 (Last access date: 24 May 2011).

Burke, T.W. & Owen, S.S. (2010). Cell phones as prison contrabands. *FBI Enforcement Bull.*, **12**: 10-15.

Department of Army (DOA) (2009). *Electronic Warfare in Operations*. Army Field Manual 3-36, Department of Army, Washington D.C.

Efstathiou, E.C. (2002). *The Mobile-Phone Silencers Controversy*. Athens University of Economics and Business, Athens.

Federal Communications Commission (FCC). *FCC Enforcement Bureau Steps Up Education and Enforcement Efforts Against Cellphone and GPS Jamming*. Media release (9 February 2011), Federal Communications Commission (FCC), Washington D.C.

Joint Chief of Staffs (JCS) (2007). *Geospatial Electronic Warfare*. Joint Publication 3-13.1, Joint Chief of Staffs (JCS), USA.

Mishra, N.K. (2009). Development of GSM - 900 mobile jammer: An approach to overcome existing limitation of jammer. *Fifth IEEE Conference on Wireless Communication and Sensor Networks (WCSN)*, 15-18 December 2009, Allahabad, India.

Molisch, F.A. (2011). Wireless Communications. John Wiley & Sons Ltd., Chichester, West Sussex.

Poisel, A.R. (2002). *Introduction to Communication Electronic Warfare Systems*. Artech House, Boston.

Netline (2011). *Cell Phone Jammer*. Available online at: http://www.netline.co.il/cell_phone_jammer.aspx (Last access date: 24 May 2011).

Nokia (2009). *Nokia E52 User Guide*. Nokia, Helsinki, Finland.

Radio Advisory Board of Canada (RBAC) (2001). Use of Jammer and Disabler Devices for Blocking PCS, Cellular & Related Services. Radio Advisory Board of Canada (RBAC), Ottawa, Ontario

Radio Spectrum Advisory Committee (RSAC) (2000). *Cellular Phone Jammers*. Radio Spectrum Advisory Committee (RSAC), Office of the Telecommunications Authority (OFTA), Hong Kong.

Sambhe, V.K., Kale, D.S.K., Wasule, A. & Neema, S. (2008). Antenna for mobile phone jammer . *First International Conference on Emerging Trends in Engineering and Technology*. 16-18 July 2008, G. H. Raisoni College of Engineering, Nagpur, India.

Sander, F.H. & Johnk, R.T., *Emission Measurements of a Cellular and PCS Jammer at a Prison Facility*. NTIA report TR-10-466, National Telecommunications and Information Administration (NTIA), US. Department of Commerce, Washington D.C.

Science & Technology Research Institute for Defence (STRIDE) (2011a). *Comparative Test of Signals of MPJ34 and MPJ2000 Mobile Phone Jammers*. Science & Technology Research Institute for Defence (STRIDE), Ministry of Defence, Malaysia.

Science & Technology Research Institute for Defence (STRIDE) (2011b). *Measurement of Minimum Interference Signal Power Level Required to Jam a Nokia E52 Mobile Phone*. Science & Technology Research Institute for Defence (STRIDE), Ministry of Defence, Malaysia.

Shah, S.W., Babar, M.I., Arbab, M.N., Yahya, K.M., Ahmad, G., Adnan, T. & Masood, A. (2008). Cell phone jammer. *12th IEEE International Multitopic Conference (INMIC 2008)*, 23-25 December 2008, Karachi.

Wollenhaupt, G. (2008). *How Cell Phone Jammers Work*. Available online at:
http://electronics.howstuffworks.com/cell-phone-jammer.htm (Last access date: 23 May 2011).

APPENDIX

Power level estimation:

P_T : Transmitter power
P_R : Receiver power
G_T : Transmitter gain
G_R : Receiver gain
L : Free-space path loss
R : Distance (km)
f : Frequency (MHz)

$$P_R = P_T + G_T + G_R - L \quad \text{(A1)}$$

$$L = 32.44 + 20 \log R + 20 \log f \quad \text{(A2)}$$

Effective isotropic radiated power (EIRP) P_{Teff}:

$$P_{T_{eff}} = P_T + G_T \quad \text{(A3)}$$

Effective received power P_{Reff}:

$$P_{R_{eff}} = P_R - G_R \quad \text{(A4)}$$

Based on received power level for R = 3 m P_{R3}:

$$P_{T_{eff}} = P_{R_3} + 32.44 + 20 \log f + 20 \log(3/1000) \quad \text{(A5)}$$

For $R = x$ m, the received power level P_{RX}:

$$P_{R_X} = P_{T_{eff}} - 32.44 - 20 \log f - 20 \log(x/1000) \quad \text{(A6)}$$

The operating radius R_O for minimum jamming power level of P_{Rmin}:

$$R_O = 10^{(P_{T_{eff}} - P_{R_{\min}} - 32.44 - 20 \log f)/20} \quad \text{(A7)}$$

CATCH OF THE NET

The traditional crime map was a jumbo representation of a jurisdiction with pins stuck on it to depict locations where crimes occurred. This manual process had serious limitations in that it could not provide accurate, reliable and comprehensive data around the clock, or help in trend prediction and decision support, resulting in lower productivity and ineffective utilisation of manpower. To this end, geographic information systems (GIS) play an important role in crime mapping & analysis through the use of computer-generated maps as an interface for accessing, integrating and coordinating large amounts of location-based data from multiple sources. GIS enables the user to layer and view the data most critical to particular issues or missions, via appropriate spatial and visual mediums, for effective planning of emergency responses and resource allocations, determination of mitigation priorities, analysis of historical events, and prediction of future trends. GIS functions, when combined with capabilities of location identification devices such as Global Positioning System (GPS) receivers, assist in tactical planning and response by facilitating the delivery of critical information to emergency responders upon dispatch or while en route to an incident. Hence, GIS-based crime mapping & analysis is being implemented by law enforcement authorities in many countries, including in Malaysia through the Safe City Monitoring System. The following are relatively interesting and useful websites on crime mapping & analysis using GIS:

1) **Crime Mapping Research Center: Mapping Crime: Principle and Practice**
   https://www.ncjrs.gov/html/nij/mapping/index.html

2) **National Institute of Justice: Mapping Crime: Understanding Hot Spots**
   http://www.nij.gov/pubs-sum/209393.htm
   Tutorials on the applications and functionalities of GIS-based crime mapping & analysis.

3) **Police Foundation: Crime Mapping News**
   http://www.policefoundation.org/docs/library.html#news
   A quarterly periodical on crime mapping & analysis, GIS and policing

4) **Raids Online**
   http://www.raidsonline.com

5) **Police.UK**
   http://www.police.uk

6) **Malaysia Crime**
   http://www.malaysiacrime.com
   Websites providing online interactive crime mapping functions.

7) **GIS Lounge: Crime Mapping and Analysis**
   http://gislounge.com/crime-mapping-and-analysis

8) **The Crime Map**
   http://thecrimemap.crimereports.com

9) **National Archive of Criminal Justice Data (NACJD): GIS Resources**
   http://www.icpsr.umich.edu/icpsrweb/NACJD/gis/resources.jsp

10) **Crime Mapping**
    http://crimemapping.wordpress.com
    Resource centres for articles, tutorials and materials on GIS-based crime mapping & analysis.

11) **GeoConnections: Emergency Mapping Symbology**
    http://emsymbology.org
    A resource centre for symbologies used for emergency and crime mapping applications.